Wireless Friendliness Evaluation of Building Materials as Reflectors

Yixin Zhang

Department of Electronic and Electrical Engineering

University of Sheffield

Supervisors: Prof. Xiaoli Chu and Prof. Jie Zhang

This thesis is submitted for the approval of the

Doctor of Philosophy

May 2022

𝔇edicated to my beloved family.

Without their unconditional love, support and encouragement,
I would not be the person I am today.

Acknowledgements

First and foremost, I would like to express my sincere gratitude to my supervisors, Prof. Xiaoli Chu and Prof. Jie Zhang, for providing me with such a great opportunity to study at the University of Sheffield. Many thanks for inspiring hope in me, igniting my imagination, and instilling in me a love of learning. Many thanks for sharing the ideas, comments, and suggestions with me and leading me out of confusion. Many thanks for spending huge time and efforts guiding me and making me an independent researcher. They act as my role models in academia, career, and life.

I am deeply grateful to some important academic and industrial partners. Thanks Dr. Jiliang Zhang from the University of Sheffield for helping me quickly adapt to my Ph.D. study and offering academic support generously and continuously. Thanks Dr. Mikko A. Uusitalo and Dr. Saeed R. Khosravirad from Nokia Bell Labs for providing me with valuable collaborations and inspiring discussions on practical guidelines. Thanks Mr. Frederik Naessens and Mr. Carl Lylon from Televic Conference for providing me with interesting industrial on-site experience and insightful advice on my academic work.

I also wish to acknowledge the financial support from the European Union's Horizon 2020 Research and Innovation Programme under the Marie Sklodowska-Curie Actions WaveComBE project (grant 766231). Thanks WaveComBE for covering my tuition fee and providing me with numerous high-quality exchange platforms, such as, visiting Universitat Politècnica de València and Dublin City University, enrolling in outreach training schools, and participating in international conferences and workshops. Also thanks to the European Union's Horizon 2020 Research and Innovation Programme AceLSAA project (grant 752644).

Special thanks to my friends and colleagues, Wenfei Yang, Chen Chen, Songjiang Yang, Monika Drozdowska, Danaisy Prado Alvarez, Wai Yan Yong, Samuel Romero, Ju Tan, Yixin Huang, Chunxia Qin, Yan Jiang, Yu Shao, Yang Zhou, Zeyang Li, Jixuan Lin, Alireza Bagheri, Mohammad Poordaraee, Othman Zahid, Mengxin Zhou, Mengxue Tang, Junwei Zhang, Hui Zheng, Bo Ma, Kan Lin, Fuyou Li, and Amar Al-Jzari, for their help and encouragement along my PhD journey. Great thanks to Zhaonan Liu for his company, support, and understanding.

Above all, I would like to express my heartfelt appreciation to my beloved family, especially my dear parents, Yingfeng Zhang and Ge Wang, for their unreserved love, endless patience, and constant encouragement. I wouldn't be where I am today without them.

Abstract

The enormous popularity of wireless devices has prompted a rapid growth of indoor wireless traffic. To meet the high data demand and avoid inconvenient usages of a room, indoor base stations (BSs) and Wi-Fi access points (APs) with large-scale multiple-input multiple-output (MIMO) antenna arrays are likely to be deployed in the vicinity of a wall, which therefore results in non-negligible interactions between indoor electromagnetic (EM) wave propagations and building materials. The reflection characteristics of building materials, which depend on their intrinsic EM and physical properties, play a crucial role in indoor wireless communications. However, the relationship between the material properties and the indoor wireless performance has not been sufficiently studied.

In this thesis, wireless friendliness is proposed as a new metric to measure the impact of a building material on indoor wireless performance as a function of its EM and physical properties. The main objectives are to develop wireless friendliness evaluation schemes for building materials as reflectors on indoor line-of-sight (LOS) MIMO communications, and to provide insights into the appropriate design and/or selection of building materials according to their wireless friendliness.

To achieve these objectives, the thesis presents four major contributions. The first contribution is to propose a new two-ray channel model and a new multipath channel model that incorporate both the LOS path and the wall reflection (WR) path for indoor LOS MIMO downlink transmissions. For the first time, the relative permittivity (EM property) and thickness (physical property) of a building material are encapsulated into the channel models through the reflection coefficient of the building material, which provides theoretical prerequisites for the subsequent tractable analysis.

The second contribution is to reveal the analytical relationship between the relative permittivity and thickness of building materials and the MIMO channel capacity. By exploiting the expressions of indoor wireless capacity and their asymptotic forms, four effective metrics for evaluating the wireless friendliness of building materials are proposed, i.e., the spatially averaged capacity, the spatially averaged logarithmic eigenvalue sum (LES), the spatially averaged logarithmic eigenvalue product (LEP), and the upper-bound outage probability, which are all over the room of interest.

The third contribution is to develop the evaluation schemes for the wireless friendliness of building materials. The optimal values of the relative permittivity and thickness of a building material that maximise the indoor wireless capacity are obtained, shedding light on the selection and/or design of a building material accordingly, and thus paving the way for wireless friendly architectural design.

The fourth contribution is to analyse the effects of the WR from building materials on the per-antenna power distribution across a precoded antenna array at a BS or an AP deployed near a wall. An uneven power distribution across antenna elements may reduce the efficiencies of their corresponding radio frequency (RF) power amplifiers. How the per-antenna power distribution changes with the building material's relative permittivity and thickness is investigated, providing guidelines on the selection and/or design of a building material that alleviates the unevenness of per-antenna power distribution.

Simulation results validate the correctness of analytical results as well as the effectiveness of the four proposed evaluation metrics, and demonstrate that the EM and physical properties of building materials have to be delicately selected or designed to avoid the risk of reducing indoor wireless capacity and RF power amplifier efficiency. More specifically, the inappropriate choices of relative permittivity and thickness of a building material may reduce the indoor wireless capacity by up to 13.5% or cause severe unevenness as large as 8 dB in the per-antenna power distribution across a precoded antenna array. The outcomes of this thesis would enable appropriate design and/or selection of building materials for building designers, e.g., civil engineers and architects, and provide wireless-friendliness information for communications engineers.

Table of contents

List of Abbreviations

2D	Two-Dimensional
3D	Three-Dimensional
5G	The Fifth Generation Mobile Communication System
6G	The Sixth Generation Mobile Communication System
AF	Array Factor
AOD	Angle of Departure
AOA	Angle of Arrival
AP	Access Point
BS	Base Station
CDF	Cumulative Distribution Function
CLT	Central Limit Theorem
EM	Electromagnetic
FSS	Frequency-Selective Surface
i.i.d.	Independent and Identically Distributed
IoT	Internet of Things
LOS	Line-of-Sight
LEP	Logarithmic Eigenvalue Product
LES	Logarithmic Eigenvalue Sum
LTE-B	LTE-Broadcast
mBBMT	Massive Broad Bandwidth Machine Type
MIMO	Multiple-Input Multiple-Output
mMTC	Massive Machine Type Communication
MPDF	Marginal Probability Density Function

MPR	Maximum Power Ratio
MU	Multi-User
NLOS	Non Line-of-Sight
OFDM	Orthogonal Frequency Division Multiplexing
PDF	Probability Density Function
PUF	Polyurethane Foam
RF	Radio Frequency
SI	International System of Units
SNR	Signal-to-Noise-Ratio
SVD	Singular Value Decomposition
TE	Transverse Electric
TM	Transverse Magnetic
ULA	Uniform Linear Array
UPA	Uniform Planar Array
UE	User Equipment
WR	Wall Reflection
XR	Extended Reality
ZF	Zero-Forcing

Part I

Introduction and Overview

List of figures

List of tables

Chapter 1

Introduction

1.1 Background

With the proliferation of existing applications (e.g., smart phones, live video streaming) and emerging innovative applications (e.g., extended reality (XR) devices, smart wearable devices, implants), the number of heterogeneous devices supporting ubiquitous wireless connections is predicted to reach tens of billions in the next few years [1–3]. As a consequence, the required wireless traffic is growing at an unprecedented rate. This undoubtedly raises a more demanding objective for the capabilities of fifth-generation (5G) or sixth-generation (6G) mobile networks [4, 5] as well as wireless local area networks based on Wi-Fi protocols [6, 7].

Notably, it is estimated that the overwhelming majority of wireless data traffic, say 80%-96%, will be consumed indoors, be it at home, in the office or in public buildings [8]. At the same time, users' expectations for economical, reliable and flexible indoor wireless services are continuing to increase, such as lower service costs, higher peak/minimum data rates, and more convenient use of spectrum resource and network infrastructure [9]. Therefore, indoor wireless networks are envisioned to be fundamental facilities for smart buildings [10], and the indoor wireless coverage and capacity will become the important basis to the site selection for human indoor activities.

The conventional buildings are increasingly limited in their abilities to support superior indoor wireless network experience for modern users' needs. One of the reasons is that the wireless network performance in an existing building may reach its achievable upper limit, which is constrained by its intrinsic factors, e.g., the properties of building materials and structures, while independent of network optimisation efforts [10]. In addition, the inefficient power consumption of the wireless networks in existing buildings may hinder the possibility of offering a variety of more power-hungry services in 6G and beyond [11, 12]. Therefore, providing advanced capability for in-building wireless communications should be one of the indispensable prerequisites for future buildings.

Multiple-input multiple-output (MIMO) technique can be used to boost indoor wireless performance by enabling multiple parallel spatial streams between transceivers without requiring additional bandwidth or higher transmission power [13, 14]. To satisfy the high data requirements and address the capacity crunch in-building, indoor small base stations (BSs) and Wi-Fi access points (APs) are commonly equipped with large-scale MIMO antenna arrays to achieve spatial multiplexing/diversity gains [15, 16], which however occupy large spatial area.

The indoor wireless signal propagation environments are complicated due to various architectural design and internal object placement [17]. Both the precise geometric specifications [18, 19] and the dielectric properties [20, 21] of the surroundings affect indoor electromagnetic (EM) wave propagations. Therefore, it is of great necessity to create constructive interactions between indoor wireless signal transmissions and the built environments.

1.2 Motivation and Objectives

For the sake of avoiding any possible detrimental effects on the safety, functionality, and appearance of a room, a popular way of deploying indoor BSs and Wi-Fi APs is to put the large-dimension MIMO antenna arrays in the vicinity of the inner walls of a building, e.g., in offices [22], shopping centres [22], hallway [23], lobbies [24], conference rooms [24–26],

and industrial mechanical or electronics rooms [27], which therefore results in non-negligible coupling between the MIMO antenna arrays and the building materials [28, 29].

Specifically, the wall in the vicinity of a BS or an AP can be regarded as a lossy dielectric structure [30, 31]. An EM wave would suffer reflection loss after hitting on the wall's surface due to multiple internal reflections. Measurement results have shown that the reflection loss is not only dependent on the incident angle and polarisation of EM waves, but also the EM and physical properties of building materials [32, 33], which can be mathematically characterised by reflection coefficients [34, 35]. The wall reflected EM waves will be superposed with other EM waves, which jointly influence the indoor wireless performance. Thus, enhancing indoor wireless performance requires a rational selection and/or design of building materials.

Meanwhile, the effects of the reflection from a building material will influence the per-antenna power distribution of a precoded antenna array at a BS or an AP. The power assigned to each transmit antenna affects the efficiency of its corresponding radio frequency (RF) power amplifier, and thus affects the power consumption of the RF chains of the BS [36]. It has been shown in [37, 38] that the uniform power excitation over all transmit antennas would allow the RF power amplifiers to work with maximum efficiency, while significant power variations across different antennas would reduce this efficiency and cause a huge waste of energy. That is why per-antenna power constraints, instead of sum power constraints, need to be well considered for practical precoder design [39].

As will be shown in the subsequent sections, the appropriate selection of building materials will increase in the baseline value of indoor wireless capacity or alleviate the unevenness of the per-antenna power distribution across a precoded antenna array. Accordingly, the wireless performance of building materials should be considered inherently in the planning and design stages of future smart/green buildings. Therefore, it is of vital importance to build a scheme to identify the relationship between the properties of building materials and indoor wireless performance.

In this thesis, wireless friendliness is proposed as a new metric of a building material, which is determined by its EM and physical properties, to measure its impact on indoor

wireless performance. A building material with desirable wireless friendliness will be beneficial to indoor wireless performance.

The overarching aim is to study the impact of building materials, especially their EM and physical properties, on the indoor wireless performance by evaluating their wireless friendliness for indoor LOS MIMO communications. To achieve this goal, the following specific research questions will be answered in this thesis:

- What are the key parameters of a building material necessary for studying the impacts of its EM and physical properties on indoor wireless performance?
- How to incorporate the key EM and physical parameters of a building material into a channel model?
- How to effectively characterise the indoor wireless performance as a function of the key EM and physical parameters of a building material?
- How to design simple and effective metrics that can be used for evaluating the wireless friendliness of a building material?
- How to develop the wireless friendliness evaluation schemes based on the proposed metrics?
- How do the reflections from a building material affect the per-antenna power distribution of a transmit precoded antenna array?
- To what extent do the appropriately selected EM and physical parameters of a building material improve the indoor wireless capacity and the evenness of the power distribution across the transmit antennas?

1.3 Thesis Outline

The thesis is composed of two parts. Part I provides a general introduction and overview, consisting of three chapters. Part II provides key technical contributions, presented by three published journal papers.

In Chapter 1, the background, motivations, and objectives of the research on the wireless friendliness evaluations of building materials as reflectors, and the thesis outline are introduced.

In Chapter 2, the ingredients, structures, EM and physical properties of existing building materials are reviewed in Section 2.1. The reflections from building materials are reviewed in Section 2.2. Finally, several aspects of indoor MIMO wireless systems, including MIMO antenna arrays, indoor multipath channel modelling, and the capacity of MIMO multipath channels, are reviewed in Section 2.3.

In Chapter 3, the contributions of the three published journal papers are briefly presented. Several insightful conclusions are summarised, and extensive studies for future works are discussed.

Chapter 2

Literature Review

2.1 Building Materials

In this section, we first introduce the ingredients and structures of building materials typically used in practice, then present two essential EM and physical parameters of building materials, i.e., relative permittivity and thickness, that are necessary for studying their wireless friendliness, and finally review the measurement results on the EM properties of building materials.

2.1.1 Ingredients and Structures

Building materials used for walls, ceilings, floors, windows, and obstructing objects differ widely in ingredients. Traditional ingredients used for the main body include: concrete, brick, plasterboard, wood, glass [40–50]. Concrete and brick are the typical components in building facades and the walls between rooms [40–43]. Plasterboards are often used in interior walls to separate two rooms [44, 45]. Glass and wood can be manufactured for windows, doors and partitioners [46–48]. Besides, traditional ingredients used for heat insulation include: mineral wool [49], fibreglass [51], cellulose [52], polystyrene [44, 51], and polyurethane foam (PUF) [53, 54]. The advantages of using these traditional ingredients of building materials are affordable price, readily available raw materials, and simple production method, which make

them widely applied in constructions. However, since it is difficult and time-consuming to retrofit them or adjust their properties, the selection of building materials deserves careful consideration.

In practical, building materials are generally made of multi-layer composite materials [45, 50], referred to as sandwich materials. A typical concrete exterior wall of a residential building is a fabricated sandwich-like panel composing of two outlying concrete layers and a heat insulation layer between them [40–42]. While the interior structures of office buildings commonly adopt two wall types: a 3-layered structure with the air layer sandwiched between two plasterboard layers; or a 4-layered structure consisting of a plasterboard layer, an air layer, a heat insulator layer, and a concrete layer [45].

2.1.2 EM and Physical Properties

EM properties

- **Permittivity** ε: a measure of the electric polarisability of a dielectric, also known as dielectric constant. The greater the permittivity, the greater the ability of a material to polarise in response to the field, thereby storing more energy in the material. Its international system of units (SI) unit is farad per meter (F/m). The permittivity of free space is $\varepsilon_0 = 8.854 \times 10^{-12}$ F/m.

- **Conductivity** σ: a measure of the material's ability to conduct electric current. Its SI unit is siemens per metre (S/m). It is the reciprocal of electrical resistivity with the SI unit of ohm-meter (Ω/m). A conductor such as a metal has high conductivity greater than 10^5 S/m and a low resistivity, while an insulator like glass has low conductivity below 10^{-10} S/m and a high resistivity. The conductivity of a semiconductor is generally intermediate. A non-conducting material has $\sigma = 0$.

- **Permeability** μ: a measure of the magnetisation that a material obtains in response to an applied magnetic field. It is the proportionality between magnetic induction and magnetising force when forming a magnetic field. Its SI unit is newtons per ampere squared $(\mathrm{N/A^2})$. The permeability of free space is $\mu_0 = 4\pi \times 10^{-7}\mathrm{N/A^2}$.

EM wave propagation originates from Maxwell's equations, the foundation of classical electromagnetism. Recall the differential form of the Maxwell–Faraday equation and the Ampère's circuital law [20]

$$\nabla \times \mathbf{E} = -\frac{\partial \mathbf{B}}{\partial t}, \tag{2.1}$$

$$\nabla \times \mathbf{B} = \mu \left(\mathbf{J}_{\mathrm{c}} + \frac{\partial \mathbf{D}}{\partial t} \right), \tag{2.2}$$

where $\mathbf{E}$, $\mathbf{B}$, $\mathbf{J}_{\mathrm{c}}$, $\mathbf{D}$, t, and $\nabla\times$ denote the electric field intensity (V/m), magnetic flux density (T), the current density of free charges $(\mathrm{A/m^2})$, the electric displacement field ($\mathrm{C/m^2}$), the time, and the curl of a vector, respectively.

Specifically, as revealed by the right-hand side in Ampère's law in (2.2), a wave propagating in a lossy medium, i.e. σ is non-zero and finite, will set up a conduction current generated by unbound conduction charges

$$\mathbf{J}_{\mathrm{c}} = \sigma \mathbf{E}, \tag{2.3}$$

as well as a displacement (polarisation) current generated by bound polarised charges

$$\mathbf{J}_{\mathrm{d}} = \frac{\partial \mathbf{D}}{\partial t} = j\omega \mathbf{D} = j\omega\varepsilon \mathbf{E}, \tag{2.4}$$

where $\omega = 2\pi f$ denotes the angular frequency under frequency f. Both currents will cause ohmic losses, and they together constitute the total effective current, which is given by

$$\mathbf{J}_{\mathrm{tot}} = \mathbf{J}_{\mathrm{c}} + \mathbf{J}_{\mathrm{d}} = (\sigma + j\omega\varepsilon)\,\mathbf{E} = j\omega\varepsilon_{\mathrm{eff}}\mathbf{E}. \tag{2.5}$$

Then the effective complex permittivity is given by

$$\varepsilon_{\mathrm{eff}} = \varepsilon - j\frac{\sigma}{\omega}. \tag{2.6}$$

The relative permittivity is a dimensionless representation of permittivity, which is defined as the ratio of the absolute permittivity and the vacuum permittivity and is given by

$$\varepsilon_{\mathrm{r}} = \frac{\varepsilon_{\mathrm{eff}}}{\varepsilon_0} \triangleq \Re(\varepsilon_{\mathrm{r}}) - j\Im(\varepsilon_{\mathrm{r}}), \tag{2.7}$$

where $\Re(\cdot)$ and $\Im(\cdot)$ denotes the real part and the image part of a complex.

The loss tangent is another quantity to characterise the degree of ohmic losses, i.e.,

$$\tan\delta = \frac{\Im(\varepsilon_{\mathrm{r}})}{\Re(\varepsilon_{\mathrm{r}})} = \frac{\sigma}{\varepsilon\omega}, \tag{2.8}$$

which establishes a dividing line between a good conductor and a good dielectric. In general, a smaller $\tan\delta$ means lower dielectric loss. Hence, the relative permittivity can also be written by

$$\varepsilon_{\mathrm{r}} = \Re(\varepsilon_{\mathrm{r}})\left(1 - j\tan\delta\right). \tag{2.9}$$

The velocity in the material is no longer the same as that in free space, which is given by

$$v = \frac{c}{n} = \frac{c}{\sqrt{\varepsilon_{\mathrm{r}}}}. \tag{2.10}$$

where $n = \sqrt{\varepsilon_{\mathrm{r}}}$ denotes the refractive index, describing how fast light travels through the material, and $c = \frac{1}{\sqrt{\varepsilon_0\mu_0}}$ denotes the speed of light.

The characteristic impedance of the material is given by

$$\eta = \sqrt{\frac{\mu}{\varepsilon_{\mathrm{eff}}}} = \sqrt{\frac{\mu}{\varepsilon\left(1 - j\tan\delta\right)}}. \tag{2.11}$$

The wave number in the material is also changed and is given by

$$k = \frac{2\pi}{\lambda_0}\sqrt{\varepsilon_{\mathrm{r}}} = \omega\sqrt{\varepsilon_{\mathrm{eff}}\mu}. \tag{2.12}$$

where $\lambda_0 = c/f$ denotes the wavelength under frequency f in the free space.

The wavelength in the material is given by

$$\lambda = \frac{v}{f} = \frac{\lambda_0}{\sqrt{\varepsilon_{\mathrm{r}}}} = \frac{2\pi}{\omega\sqrt{\varepsilon_{\mathrm{eff}}\mu}}. \tag{2.13}$$

Substituting (2.1) and (2.3) into (2.2), we have $\nabla^2\mathbf{E} - \varepsilon\mu\frac{\partial^2\mathbf{E}}{\partial t^2} = \mu\sigma\frac{\partial\mathbf{E}}{\partial t}$. Then, a possible wave solution is given by

$$\mathbf{E} = \mathbf{E_0}e^{j(\omega t - \mathbf{kr})}, \tag{2.14}$$

where $\mathbf{r}$ denotes the propagation distance vector, $\mathbf{E_0}$ denotes the electric field when $t = 0, \mathbf{r} = \mathbf{0}$, and $\mathbf{k}$ denotes the wave number vector with $|\mathbf{k}| = 2\pi/\lambda$.

Assuming that $\mathbf{k}$ and $\mathbf{r}$ are both one dimensional vectors, substitute (2.12) into (2.14) and let $\gamma = jk \triangleq \alpha + j\beta$ denote the propagation constant, then (2.14) becomes

$$\mathbf{E} = \mathbf{E}_0 e^{j\omega t}e^{-\alpha r}e^{-j\beta r}, \tag{2.15}$$

where

$$\alpha = \omega\sqrt{\frac{\mu\varepsilon}{2}\left(\sqrt{1+\tan^2\delta} - 1\right)}, \tag{2.16}$$

$$\beta = \omega\sqrt{\frac{\mu\varepsilon}{2}\left(\sqrt{1+\tan^2\delta} + 1\right)}. \tag{2.17}$$

From (2.15), α and β can be physically interpreted as the attenuation constant in (Np/m) and phase constant in (rad/m), respectively [56]. At the skin depth of $\Delta = \frac{1}{\alpha}$, the field strength decreases to $\frac{1}{e}$, i.e., nearly 63% drop. The attenuation rate in dB/m is defined by $20\log_{10}|e^{-\alpha r}| = -8.686\alpha r$ [20].

The following Table. 2.1 summarises the values of the propagation parameters in different mediums.

Table 2.1 The propagation parameters in different mediums [57]

	Lossless Medium ($\sigma = 0$)	Low-loss Medium ($\sigma << \varepsilon\omega$)	Good Conductor ($\sigma >> \varepsilon\omega$)	Units
α	0	$\frac{\sigma}{2}\sqrt{\frac{\mu}{\varepsilon}}$	$\sqrt{\frac{\mu\sigma\omega}{2}} = \sqrt{\pi f\mu\sigma}$	(Np/m)
β	$\omega\sqrt{\mu\varepsilon}$	$\omega\sqrt{\mu\varepsilon}$	$\sqrt{\frac{\mu\sigma\omega}{2}} = \sqrt{\pi f\mu\sigma}$	(rad/m)
η	$\sqrt{\frac{\mu}{\varepsilon}}$	$\sqrt{\frac{\mu}{\varepsilon}}$	$(1+j)\sqrt{\frac{\mu\omega}{2\sigma}} = (1+j)\frac{\alpha}{\sigma}$	(Ω)
v	$\frac{1}{\sqrt{\mu\varepsilon}}$	$\frac{1}{\sqrt{\mu\varepsilon}}$	$\sqrt{\frac{4\pi f}{\mu\sigma}}$	(m/s)
λ	$\frac{1}{f\sqrt{\mu\varepsilon}}$	$\frac{1}{f\sqrt{\mu\varepsilon}}$	$\sqrt{\frac{4\pi}{f\mu\sigma}}$	(m)

Note that for most practical material samples, e.g., non-ionised and non-magnetic materials, the conductivity σ and permittivity ε are the most important factor, while the permeability μ is commonly set as μ_0 [9, 20].

Physical properties

- **Thickness**: typically comparable to the *cm* wavelength. It determines the distance that the incident EM waves propagate inside a building material.
- **Roughness**: also known as surface irregularity, on the order of hundreds of μm. The roughness of a material will affect the reflection and diffuse scattering phenomena with respect to the material. When the surface is made progressively rougher, the reflected wave will be scattered from a large number of positions on the surface, broadening the scattered energy. This reduces the energy in the specular direction and increases the energy radiated in other directions [9].

The thickness of a building material is affected by its usage, i.e., the thickness of load-bearing walls would be much larger than the non-load bearing walls [50]. The thickness of the heat insulation layer has to be specified according to the type of insulation materials as well as the building regulations during design and constructions [50]. Increasingly stringent building regulations require good thermal isolation of houses to ensure a high heating efficiency of buildings [49, 58].

The roughness of a building material influences the effects of diffuse scattering on the EM wave propagations. At microwave bands, given that the wavelength of *cm* is much larger than the surface irregularities of μm, the scattering effects are negligible. Even at the frequency band about 26 GHz, the impact of diffuse scattering is still not be comparable to the impact of multiple bounce specular reflections, because the former results in the received power 10 dB less than the latter [59]. Diffuse scattering will be more pronounced for carrier frequencies above 40 GHz [47, 60].

2.1.3 Measurements on the EM Properties

In literatures, numerous experimental campaigns show that the signal attenuation or the penetration loss through a building material is dependent on frequency and polarisation. The authors in [46] validated that the brick wall has penetration loss that increases as a function of the frequency. The authors in [41] and [49] showed that the metallic surfaces or foil and modern windows consisting of low emission glasses to improve thermal isolation efficiency provide considerably additional RF attenuations that increases with the frequency from 900 MHz to 2100 MHz and from 800 MHz to 5000 MHz, respectively. The authors in [43] demonstrated that the plaster mesh used to fix a layer of material on a concrete wall significantly increases the overall signal attenuation, which decreases with the frequency in the range of 500 MHz to 6 GHz and is affected by the size of mesh. The authors in [61] provided the results of partition losses of dry wall, whiteboard, clear glass, and mesh glass under 2.5 GHz and 60 GHz and concluded that high levels of signal attenuation under high frequency caused by certain building materials may help keep the signals confined in a room, while low levels of signal attenuation at low frequency enables the wireless system to cover several rooms. The authors in [62] indicated linear regression trends of the relative permittivity with respect to the frequency for marble, concrete, brick, and plasterboard, except glass, investigated the permittivity effects of building materials on path loss and channel impulse responses via 3D ray tracing simulations (assuming all materials with the same given permittivity) and field measurement under 28 GHz in urban micro-cell environments, and demonstrated the impact of permittivity on the multipath numbers and received signal strength at the non line-of-sight (NLOS) regions. The authors in [33] conducted the measurements at 5.8 GHz of the penetration losses for dry wall, wood, door window, and steel door, along with five different combinations of antenna polarisations (linear, circular polarized, and slant 45°). The results show that combinations of vertical-vertical and slant 45°-slant 45° polarisations have relative low penetration losses and high reflectivity, while the combination of circular-circular polarisation experiences low reflectivity and significant penetration loss.

Besides, plentiful measurement results reveal that the relative permittivity of a building material changes with its composition, moisture, temperature, and working frequency band.

The three main components of concrete are cement, aggregate and water with a rough proportion of 1:7:2 [40], while additional chemical admixtures are usually added to accelerate or slow down the hydration process and/or to increase the resistance against frost of hardened concrete. The authors in [63] validated that the permittivities and loss tangents of foamed concrete materials can be accurately predicted by the foam content and blast furnace slag content in the frequency range of 1-8 GHz. The authors in [40, 42] showed that the RF attenuations under 4.5-19 GHz, 7-13 GHz, and 26-40 GHz frequency range vary significantly among different concrete samples of various water-cement ratio, moisture, type, and frequency band, duo to the great difference between their real parts and imaginary parts of the relative permittivities as well as their loss tangents. The authors in [64] extracted the approximated relative permittivity values of brick, glass, concrete, plasterboard, and plywood and chipwood, by fitting the measurement results versus frequency into a polynomial regression curve in a wide frequency range of 2-62.4 GHz. The authors in [65] measured the complex relative permittivities and loss tangents of 20 common materials in indoor environments (including plastics, wood and wood-based materials, glass, gypsum plaster and plasterboard, brick, and concrete) over the frequency band 0.2-67 GHz. The frequency dependence of the material properties is fitted by using a single-pole Cole-Cole model. The authors in [66] revealed that the behaviours of dielectric permittivity of cement-based materials at 2.45 GHz are greatly affected by the temperature, free moisture content, and hydration time. The authors in [48] presented that the dielectric constants of granite, marble, wooden board, and polyvinyl chloride board hardly change with the frequency in the range of 40 GHz to 50 GHz, while their conductivities change remarkably.

Based on the above measured data and using the widely-used curve-fitting method, the ITU recommendations [20] gives the value of relative permittivity ε_{r} as a function of frequency, which is given by

$$\Re(\varepsilon_{\mathrm{r}}) = uf^{v}, \tag{2.18}$$

$$\Im(\varepsilon_{\mathrm{r}}) = 17.98\sigma/f, \tag{2.19}$$

where

$$\sigma = rf^t, \tag{2.20}$$

and constants u, v, r and t are compiled in Table. 2.2, for the frequency range of 0.01-100 GHz.

Table 2.2 Material EM properties [20]

Material class	Real part		Conductivity		Frequency range
	u	v	r	t	GHz
Vacuum ($\approx$ air)	1	0	0	0	0.01-100
Concrete	5.31	0	0.0326	0.8095	1-100
Brick	3.75	0	0.038	0	1-10
Plasterboard	2.94	0	0.0116	0.7076	1-100
Wood	1.99	0	0.0047	1.0718	0.01-100
Glass	6.27	0	0.0043	1.1925	0.1-100
Ceiling board	1.50	0	0.0005	1.1634	1-100
Floorboard	3.66	0	0.0044	1.3515	50-100
Chipboard	2.58	0	0.0217	0.78	1-100
Very dry ground	3	0	0.00015	2.52	1-10 only
Medium dry ground	15	-0.1	0.035	1.63	1-10 only
Wet ground	30	-0.4	0.15	1.30	1-10 only

2.2 Reflections from Building Materials

EM waves emitted from the transmitter often experience complicated reflection process, e.g., one-bounce reflection, two-bounce reflection, with the interacting physical objects before arriving the receiver. The reflection characteristics of common building materials will be required for the planning and design of future wireless communication systems [67]. The received signal power loss caused by reflections from building materials is jointly determined by the polarisation and the incident angle of the incident EM waves as well as the intrinsic EM and physical properties, i.e., the relative permittivity and thickness, of the interacting building materials [20, 26, 32].

The reflection coefficient of a building material describes how much of the EM waves is reflected by an impedance discontinuity in the transmission medium. Existing studies

on the reflection coefficients of building materials are mostly through measurements and simulations. The authors in [28] performed experiments for the reflection coefficients of several material samples (PVC, wooden structures, plaster, mortar, concrete, etc.) in the frequency range between 8 and 12.5 GHz, and summarised that, in general, the amplitudes of the reflection coefficient slightly decrease with the frequency, while the phases decrease linearly with the frequency because the travelling thickness in a given sample increases as the wavelength decreases. The authors in [29] verified through simulations that considering multiple reflections results in higher spatial signal received power at 350 GHz as compared to Fresnel reflections, and emphasised the importance of including multiple reflections from stratified building materials. The authors in [45] measured the reflection coefficients of interior walls of office buildings with sandwich structures in the 60 GHz band under parallel, perpendicular, and circular polarisations, and found that the use of circular polarisation can reduce the reflection even if the interior parts of the structure have complicated structures. The authors in [68] presented the substantial difference between the reflection coefficients under normal incidence at 890 MHz versus the relative permittivity and the conductivity under single-ray model and multi-ray model (i.e., consider multiple internal reflections or not), respectively, indicating that the use of the more accurate multi-ray model would be more appropriate for studying reflection phenomenon. The authors in [69] showed the reflection coefficients of a group of concrete slabs versus the incident angle under 18.7 GHz and 60 GHz, and found that the reflection coefficient is affected by the thickness of the gravel used for preventing the concrete from cracking and shifting. The authors in [70] plotted the measured reflection coefficients of several house flooring materials (i.e., hardwood, vinyl, and carpet) and the analytical reflection coefficients under different incident angles in the frequency range of 57-64 GHz, and found that hardwood and vinyl have better reflectivity than carpet due to more shiny surface with small roughness. Vinyl and carpet present the most and the least dependence of the reflection coefficient on frequency, respectively. Adding a plywood supporting layer to vinyl and carpet will decrease and increase this frequency dependence, respectively.

In the following, we study how the reflection coefficients considering multiple internal reflections of a single-layer building material and a sandwich material are derived from the classical EM wave propagation theory, and plot some figures to gain some insights on the reflection coefficients.

2.2.1 Transverse Impedances

Many types of waves can satisfy Maxwell's equations, e.g., plane, spherical, and cylindrical waves. However, plane wave assumptions are widely used for analysis due to the following two reasons: first, plane wave is a fundamental type since any other wave type can be represented by a collection of plane waves; second, it can exhibit the necessary EM wave properties in a simpler and more analytically tractable way compared with the other complicated wave types [9, Ch 4]. Therefore, in the following analysis, we adopt uniform plane wave assumptions.

Fig. 2.1 depicts uniform plane waves incident from both sides onto a planar interface separating two mediums ε, $\bar{\varepsilon}$. Both cases of transverse electric (TE) and transverse magnetic (TM) polarisations are shown. In TE polarisation, also known as perpendicular polarisation, s-polarisation, or σ-polarisation, the electric fields are perpendicular to the plane of incidence, and the magnetic fields are parallel to that plane. In TM polarisation, also known as parallel polarisation, p-polarisation, or π-polarisation, the electric fields are parallel to the plane of incidence, and the magnetic fields are perpendicular to that plane.

Based on the boundary conditions that the net transverse component of the electric field must be continuous across the interface $z = 0$, three important theorems are found:

1) The vector wave numbers of the reflected and refracted waves lie in the plane of incidence, i.e.,

$$\begin{aligned} k_{x+} &= k_{x-} = \bar{k}_{x+} = \bar{k}_{x-}, \\ k_{y+} &= k_{y-} = \bar{k}_{y+} = \bar{k}_{y-}. \end{aligned} \tag{2.21}$$

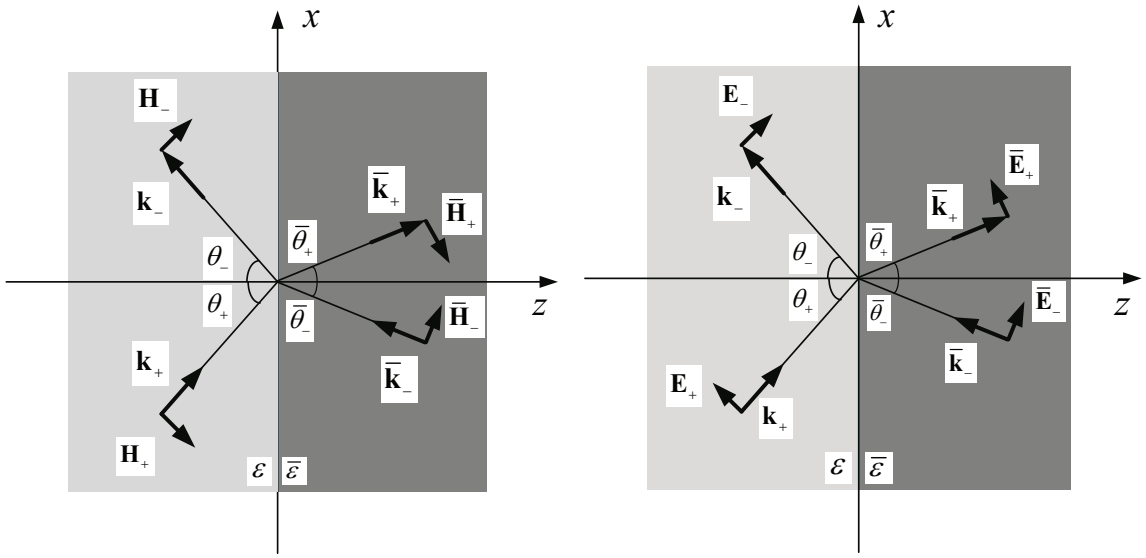

(a) TE, perpendicular, s- polarisation

(b) TM, parallel, p- polarisation

Fig. 2.1 Oblique incidence for TE and TM polarised waves.

2) Snell's law of reflection: the angles of incidence and reflection are the same on either side.

$$\begin{aligned} \theta_+ &= \theta_- \triangleq \theta, \\ \bar{\theta}_+ &= \bar{\theta}_- \triangleq \bar{\theta}. \end{aligned} \tag{2.22}$$

3) Snell's law of refraction:

$$\frac{\sin\theta}{\sin\bar{\theta}} = \frac{\bar{k}}{k} = \frac{\bar{n}}{n} = \frac{\sqrt{\bar{\varepsilon}}}{\sqrt{\varepsilon}}. \tag{2.23}$$

Transverse impedance is defined as the ratio of the transverse components of the electric and magnetic fields. The transverse impedances for TE and TM polarisation cases are defined differently in terms of the incident angle.

Generally, an obliquely-moving EM wave will have both TE and TM components. In Fig. 2.1, we consider a wave with the incident angle of θ impinges on the mediums that are stacked along the positive z direction. The electric and magnetic fields of the wave on the

interface $z = 0$ are given as

$$\begin{aligned}\mathbf{E}_+(x,z) &= [(\vec{\mathbf{x}}\cos\theta - \vec{\mathbf{z}}\sin\theta)A_+ + \vec{\mathbf{y}}B_+]\, e^{-j(k_x x + k_z z)},\\ \mathbf{H}_+(x,z) &= \frac{1}{\eta}\,[\vec{\mathbf{y}}A_+ - (\vec{\mathbf{x}}\cos\theta - \vec{\mathbf{z}}\sin\theta)B_+]\, e^{-j(k_x x + k_z z)},\end{aligned} \tag{2.24}$$

where A_+ and B_+ denote the TM and TE components, respectively, $\vec{\mathbf{x}}$, $\vec{\mathbf{y}}$ and $\vec{\mathbf{z}}$ denote the unit vector towards the positive x-axis, y-axis, and z-axis, respectively, $k_x = k\sin\theta$, and $k_z = k\cos\theta$. After interacting with the medium interface, the electric and magnetic fields of the wave reflected back to medium ε are formed by

$$\begin{aligned}\mathbf{E}_-(x,z) &= [(\vec{\mathbf{x}}\cos\theta + \vec{\mathbf{z}}\sin\theta)A_- + \vec{\mathbf{y}}B_-]\, e^{-j(k_x x - k_z z)},\\ \mathbf{H}_-(x,z) &= \frac{1}{\eta}\,[-\vec{\mathbf{y}}A_- + (\vec{\mathbf{x}}\cos\theta + \vec{\mathbf{z}}\sin\theta)B_-]\, e^{-j(k_x x - k_z z)},\end{aligned} \tag{2.25}$$

where A_- and B_- denote the TM and TE components, respectively.

Hence, the net transverse fields in the left medium ε can be organised as [55, Ch 7]

$$\begin{aligned}\mathbf{E}_{\mathrm{T}}(x,z) &= \mathbf{E}_{\mathrm{T}+}(x,z) + \mathbf{E}_{\mathrm{T}-}(x,z) = \vec{\mathbf{x}}E_{\mathrm{TM}}(x,z) + \vec{\mathbf{y}}E_{\mathrm{TE}}(x,z),\\ \mathbf{H}_{\mathrm{T}}(x,z) &= \mathbf{H}_{\mathrm{T}+}(x,z) + \mathbf{H}_{\mathrm{T}-}(x,z) = \vec{\mathbf{y}}H_{\mathrm{TM}}(x,z) - \vec{\mathbf{x}}H_{\mathrm{TE}}(x,z),\end{aligned} \tag{2.26}$$

where subscript T denotes the transverse (with respect to z) components of the vector,

$$\begin{aligned}E_{\mathrm{TE}}(x,z) &= \left[B_{\mathrm{T}+}e^{-jk_z z} + B_{\mathrm{T}-}e^{jk_z z}\right] e^{-jk_x x},\\ H_{\mathrm{TE}}(x,z) &= \frac{1}{\eta_{\mathrm{TE}}}\left[B_{\mathrm{T}+}e^{-jk_z z} - B_{\mathrm{T}-}e^{jk_z z}\right] e^{-jk_x x},\end{aligned} \tag{2.27}$$

$$\begin{aligned}E_{\mathrm{TM}}(x,z) &= \left[A_{\mathrm{T}+}e^{-jk_z z} + A_{\mathrm{T}-}e^{jk_z z}\right] e^{-jk_x x},\\ H_{\mathrm{TM}}(x,z) &= \frac{1}{\eta_{\mathrm{TM}}}\left[A_{\mathrm{T}+}e^{-jk_z z} - A_{\mathrm{T}-}e^{jk_z z}\right] e^{-jk_x x},\end{aligned} \tag{2.28}$$

in which $A_{\mathrm{T}\pm} = A_\pm\cos\theta$, $B_{\mathrm{T}\pm} = B_\pm$ denote the transverse amplitudes, respectively, and

$$\begin{aligned}\eta_{\mathrm{TE}} &= \frac{\eta}{\cos\theta},\\ \eta_{\mathrm{TM}} &= \eta\cos\theta,\end{aligned} \tag{2.29}$$

denote the transverse impedances for TE and TM polarised waves, respectively.

Accordingly, the transverse refractive index for TE and TM polarised waves are, respectively, given by

$$\begin{aligned} n_{\mathrm{TE}} &= n\cos\theta, \\ n_{\mathrm{TM}} &= \frac{n}{\cos\theta}. \end{aligned} \tag{2.30}$$

For convenience, we remove the common factor $e^{-jk_x x}$ and summarise (2.27)-(2.29) in a compact form:

$$\begin{aligned} E_{\mathrm{T}}(z) &= E_{\mathrm{T}+}e^{-jk_z z} + E_{\mathrm{T}-}e^{jk_z z}, \\ H_{\mathrm{T}}(z) &= \frac{1}{\eta_{\mathrm{T}}}\left[E_{\mathrm{T}+}e^{-jk_z z} - E_{\mathrm{T}-}e^{jk_z z}\right], \end{aligned} \tag{2.31}$$

where E_{T} stands for either $E_{\mathrm{TE}\pm} = B_{\mathrm{T}\pm}$ or $E_{\mathrm{TM}\pm} = A_{\mathrm{T}\pm}$, and η_{T} stands for either $\eta_{\mathrm{TE}} = \frac{\eta}{\cos\theta}$ or $\eta_{\mathrm{TM}} = \eta\cos\theta$.

2.2.2 Propagation of Transverse Fields

The transverse wave impedance Z_{T} and the transverse reflection coefficient Γ_{T} at position z are, respectively, defined by

$$Z_{\mathrm{T}}(z) = \frac{E_{\mathrm{T}}(z)}{H_{\mathrm{T}}(z)}, \tag{2.32}$$

$$\Gamma_{\mathrm{T}}(z) = \frac{E_{\mathrm{T}-}(z)}{E_{\mathrm{T}+}(z)}. \tag{2.33}$$

Given that

$$\begin{aligned} E_{\mathrm{T}}(z) &= E_{\mathrm{T}+}(z) + E_{\mathrm{T}-}(z), \\ H_{\mathrm{T}}(z) &= \frac{1}{\eta_{\mathrm{T}}}\left[E_{\mathrm{T}+}(z) - E_{\mathrm{T}-}(z)\right], \end{aligned} \tag{2.34}$$

and

$$\begin{aligned} E_{\mathrm{T}+}(z) &= \frac{1}{2}[E_{\mathrm{T}}(z) + \eta_{\mathrm{T}}H_{\mathrm{T}}(z)], \\ E_{\mathrm{T}-}(z) &= \frac{1}{2}[E_{\mathrm{T}}(z) - \eta_{\mathrm{T}}H_{\mathrm{T}}(z)], \end{aligned} \tag{2.35}$$

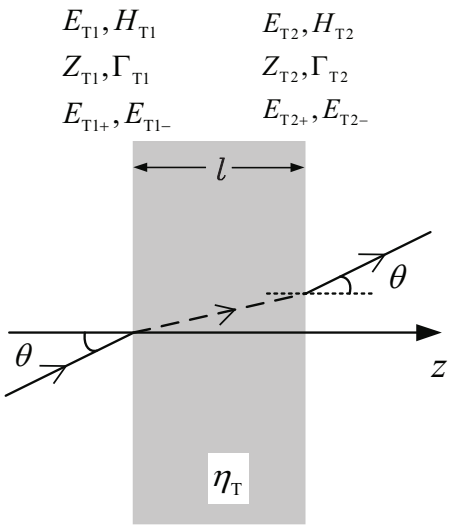

Fig. 2.2 Field quantities on the interfaces of a medium.

by substituting (2.34) into (2.32) and substituting (2.35) into (2.33), we have the relationships between wave impedance and reflection coefficient

$$Z_{\mathrm{T}}(z) = \eta_{\mathrm{T}} \frac{1+\Gamma_{\mathrm{T}}(z)}{1-\Gamma_{\mathrm{T}}(z)} \Leftrightarrow \Gamma_{\mathrm{T}}(z) = \frac{Z_{\mathrm{T}}(z)-\eta_{\mathrm{T}}}{Z_{\mathrm{T}}(z)+\eta_{\mathrm{T}}}. \tag{2.36}$$

Fig. 2.2 illustrates the fields quantities $E_{\mathrm{T}}(z), H_{\mathrm{T}}(z), E_{\mathrm{T}+}(z), E_{\mathrm{T}-}(z), Z_{\mathrm{T}}(z), \Gamma_{\mathrm{T}}(z)$ propagated on the interfaces of a medium with the thickness of l m and the transverse impedance of η_{T}. The incident angle of waves is denoted by θ. It is easy to get $E_{\mathrm{T1}+} = e^{jk_z l} E_{\mathrm{T2}+}$ and $E_{\mathrm{T1}-} = e^{-jk_z l} E_{\mathrm{T2}-}$, which can be organised in a matrix form as:

$$\begin{bmatrix} E_{\mathrm{T1}+} \\ E_{\mathrm{T1}-} \end{bmatrix} = \begin{bmatrix} e^{jk_z l} & 0 \\ 0 & e^{-jk_z l} \end{bmatrix} \begin{bmatrix} E_{\mathrm{T2}+} \\ E_{\mathrm{T2}-} \end{bmatrix}.$$

Considering the summation of the forward and backward fields, we have

$$\begin{aligned} \begin{bmatrix} E_{\mathrm{T1}} \\ H_{\mathrm{T1}} \end{bmatrix} &= \begin{bmatrix} 1 & 1 \\ \eta_{\mathrm{T}}^{-1} & -\eta_{\mathrm{T}}^{-1} \end{bmatrix} \begin{bmatrix} E_{\mathrm{T1}+} \\ E_{\mathrm{T1}-} \end{bmatrix} = \begin{bmatrix} 1 & 1 \\ \eta_{\mathrm{T}}^{-1} & -\eta_{\mathrm{T}}^{-1} \end{bmatrix} \begin{bmatrix} e^{jk_z l} & 0 \\ 0 & e^{-jk_z l} \end{bmatrix} \begin{bmatrix} E_{\mathrm{T2}+} \\ E_{\mathrm{T2}-} \end{bmatrix} \\ &= \frac{1}{2} \begin{bmatrix} 1 & 1 \\ \eta_{\mathrm{T}}^{-1} & -\eta_{\mathrm{T}}^{-1} \end{bmatrix} \begin{bmatrix} e^{jk_z l} & 0 \\ 0 & e^{-jk_z l} \end{bmatrix} \begin{bmatrix} 1 & \eta_{\mathrm{T}} \\ 1 & -\eta_{\mathrm{T}} \end{bmatrix} \begin{bmatrix} E_{\mathrm{T2}} \\ H_{\mathrm{T2}} \end{bmatrix}, \end{aligned}$$

which can be simplified after the matrix calculations as

$$\begin{bmatrix} E_{\mathrm{T1}} \\ H_{\mathrm{T1}} \end{bmatrix} = \begin{bmatrix} \cos k_z l & j\eta_{\mathrm{T}} \sin k_z l \\ j\eta_{\mathrm{T}}^{-1} \sin k_z l & \cos k_z l \end{bmatrix} \begin{bmatrix} E_{\mathrm{T2}} \\ H_{\mathrm{T2}} \end{bmatrix}. \tag{2.37}$$

(2.37) is defined as propagation matrix [55, Ch 7].

Similarly, the transverse reflection coefficient and transverse wave impedance propagates as:

$$\Gamma_{\mathrm{T1}} = \frac{E_{\mathrm{T1}-}}{E_{\mathrm{T1}+}} = \frac{E_{\mathrm{T2}-} e^{-jk_z l}}{E_{\mathrm{T2}+} e^{jk_z l}} = \Gamma_{\mathrm{T2}} e^{-j2k_z l}, \tag{2.38}$$

$$Z_{\mathrm{T1}} = \frac{E_{\mathrm{T1}}}{H_{\mathrm{T1}}} = \frac{E_{\mathrm{T2}} \cos k_z l + j\eta_{\mathrm{T}} H_{\mathrm{T2}} \sin k_z l}{jE_{\mathrm{T2}} \eta_{\mathrm{T}}^{-1} \sin k_z l + H_{\mathrm{T2}} \cos k_z l} = \eta_{\mathrm{T}} \frac{Z_{\mathrm{T2}} + j\eta_{\mathrm{T}} \tan k_z l}{\eta_{\mathrm{T}} + jZ_{\mathrm{T2}} \tan k_z l}. \tag{2.39}$$

The propagation phase thickness is then defined by

$$\delta_z = k_z l = kl \cos\theta = \frac{2\pi}{\lambda} \sqrt{\varepsilon_{\mathrm{r}}} l \cos\theta. \tag{2.40}$$

2.2.3 Fresnel Reflection Coefficients

As shown in Fig. 2.1, the boundary conditions on the interface $z = 0$ for the transverse electrical and magnetic fields are given by $E_{\mathrm{T}} = \bar{E}_{\mathrm{T}}, H_{\mathrm{T}} = \bar{H}_{\mathrm{T}}$. In terms of the forward and backward fields, we have

$$\begin{aligned} E_{\mathrm{T}+} + E_{\mathrm{T}-} &= \bar{E}_{\mathrm{T}+} + \bar{E}_{\mathrm{T}-}, \\ \frac{1}{\eta_{\mathrm{T}}} \left(E_{\mathrm{T}+} - E_{\mathrm{T}-} \right) &= \frac{1}{\bar{\eta}_{\mathrm{T}}} \left(\bar{E}_{\mathrm{T}+} - \bar{E}_{\mathrm{T}-} \right), \end{aligned} \tag{2.41}$$

which can be organised into the matching matrix [55, Ch 7]

$$\begin{bmatrix} E_{\mathrm{T}+} \\ E_{\mathrm{T}-} \end{bmatrix} = \frac{1}{\tau_{\mathrm{T}}} \begin{bmatrix} 1 & \rho_{\mathrm{T}} \\ \rho_{\mathrm{T}} & 1 \end{bmatrix} \begin{bmatrix} \bar{E}_{\mathrm{T}+} \\ \bar{E}_{\mathrm{T}-} \end{bmatrix}, \tag{2.42}$$

$$\begin{bmatrix} \bar{E}_{\mathrm{T}+} \\ \bar{E}_{\mathrm{T}-} \end{bmatrix} = \frac{1}{\bar{\tau}_{\mathrm{T}}} \begin{bmatrix} 1 & \bar{\rho}_{\mathrm{T}} \\ \bar{\rho}_{T} & 1 \end{bmatrix} \begin{bmatrix} E_{\mathrm{T}+} \\ E_{\mathrm{T}-} \end{bmatrix}, \tag{2.43}$$

where $\{\rho_{\mathrm{T}} = \frac{E_{\mathrm{T}-}}{E_{\mathrm{T}+}}, \tau_{\mathrm{T}} = \frac{\bar{E}_{\mathrm{T}+}}{E_{\mathrm{T}+}}\}$ and $\{\bar{\rho}_{\mathrm{T}} = \frac{\bar{E}_{\mathrm{T}-}}{\bar{E}_{\mathrm{T}+}}, \bar{\tau}_{\mathrm{T}} = \frac{E_{\mathrm{T}-}}{\bar{E}_{\mathrm{T}-}}\}$ are defined as the elementary reflection and transmission coefficients from the left side and the right side of the interface:

$$\begin{aligned} \rho_{\mathrm{T}} &= \frac{\bar{\eta}_{\mathrm{T}} - \eta_{\mathrm{T}}}{\bar{\eta}_{\mathrm{T}} + \eta_{\mathrm{T}}} = \frac{n_{\mathrm{T}} - \bar{n}_{\mathrm{T}}}{n_{\mathrm{T}} + \bar{n}_{\mathrm{T}}}, \\ \tau_{\mathrm{T}} &= \frac{2\bar{\eta}_{\mathrm{T}}}{\bar{\eta}_{\mathrm{T}} + \eta_{\mathrm{T}}} = \frac{2n_{\mathrm{T}}}{n_{\mathrm{T}} + \bar{n}_{\mathrm{T}}}, \end{aligned} \tag{2.44}$$

$$\begin{aligned} \bar{\rho}_{\mathrm{T}} &= \frac{\eta_{\mathrm{T}} - \bar{\eta}_{\mathrm{T}}}{\bar{\eta}_{\mathrm{T}} + \eta_{\mathrm{T}}} = \frac{\bar{n}_{\mathrm{T}} - n_{\mathrm{T}}}{n_{\mathrm{T}} + \bar{n}_{\mathrm{T}}}, \\ \bar{\tau}_{\mathrm{T}} &= \frac{2\eta_{\mathrm{T}}}{\bar{\eta}_{\mathrm{T}} + \eta_{\mathrm{T}}} = \frac{2\bar{n}_{\mathrm{T}}}{n_{\mathrm{T}} + \bar{n}_{\mathrm{T}}}, \end{aligned} \tag{2.45}$$

where $\tau_{\mathrm{T}} = 1 + \rho_{\mathrm{T}}$, $\bar{\rho}_{\mathrm{T}} = -\rho_{\mathrm{T}}$, $\bar{\tau}_{\mathrm{T}} = 1 + \bar{\rho}_{\mathrm{T}} = 1 - \rho_{\mathrm{T}}$. Meanwhile, (2.44) and (2.45) are well known as Fresnel reflection coefficients.

Substituting (2.29) and (2.30) into (2.44), we get the Fresnel reflection coefficients for TE and TM polarised waves:

$$\begin{aligned} \rho_{\mathrm{TE}} &= \frac{\frac{\bar{\eta}}{\cos\bar{\theta}} - \frac{\eta}{\cos\theta}}{\frac{\bar{\eta}}{\cos\bar{\theta}} + \frac{\eta}{\cos\theta}} = \frac{n\cos\theta - \bar{n}\cos\bar{\theta}}{n\cos\theta + \bar{n}\cos\bar{\theta}}, \\ \rho_{\mathrm{TM}} &= \frac{\bar{\eta}\cos\bar{\theta} - \eta\cos\theta}{\bar{\eta}\cos\bar{\theta} + \eta\cos\theta} = \frac{\frac{n}{\cos\theta} - \frac{\bar{n}}{\cos\bar{\theta}}}{\frac{n}{\cos\theta} + \frac{\bar{n}}{\cos\bar{\theta}}}. \end{aligned} \tag{2.46}$$

2.2.4 ITU Reflection Coefficients

The Fresnel reflection coefficient in the previous section only works for the building material whose thickness is assumed to be electrically large when compared to the EM wavelength [64], without considering the multiple internal reflections inside the material of a specific thickness. In this section, we take into account the effects of multiple internal reflections on the equivalent reflection coefficient. We suppose that the EM waves impinge from the air ($c_0 = 3 \times 10^8$ m/s, $\eta_0 = \sqrt{\frac{\mu_0}{\varepsilon_0}} = 377$ ohm) to the material surface with the incident angle of θ, as shown in Fig. 2.3. The Fresnel reflection coefficient can be interpreted as the first-order reflection coefficient.

Single-layer materials: Supposing that the building material is a single-layer reflector, the multiple internal reflections inside it are strongly affected by the first-order reflection.

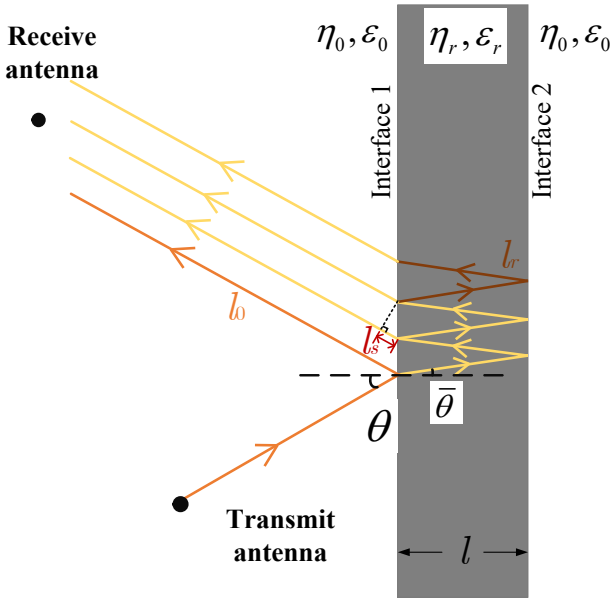

Fig. 2.3 Multiple internal reflections happened inside the building material. The receive antenna is in the far field.

Replacing n with $\sqrt{\varepsilon_r}$ in (2.46) and recalling (2.23), the first-order reflection coefficient Γ' for the incident electric field of TE polarisation Γ_{TE} and TM polarisation Γ_{TM} are given respectively by

$$\Gamma_{TE} = \frac{\cos\theta - \sqrt{\varepsilon_r - \sin^2\theta}}{\cos\theta + \sqrt{\varepsilon_r - \sin^2\theta}}, \tag{2.47}$$

or

$$\Gamma_{TM} = \frac{\cos\theta - \sqrt{(\varepsilon_r - \sin^2\theta)/\varepsilon_r{}^2}}{\cos\theta + \sqrt{(\varepsilon_r - \sin^2\theta)/\varepsilon_r{}^2}}, \tag{2.48}$$

Given the thickness of the considered wall as l, the equivalent reflection coefficient considering multiple internal reflections is represented by [20]

$$\Gamma_{single} = \frac{1 - \exp(-j2\delta)}{1 - \Gamma'^2 \exp(-j2\delta)}\Gamma', \tag{2.49}$$

where

$$\delta = \frac{2\pi l}{\lambda}\sqrt{\varepsilon_r - \sin^2\theta}, \tag{2.50}$$

and Γ' for TE or TM polarised incident wave is given in (2.47) or (2.48).

Proof: Based on the relationship observed from (2.44) and (2.45) and the first-order reflection coefficient at interface 1 denoted as $\Gamma^{'}$, we know the transmission coefficient from the air to the material and from the material to the air can be represented by $1+\Gamma^{'}$ and $1-\Gamma^{'}$, respectively, and first-order reflection coefficient at interface 2 can be given by $-\Gamma^{'}$. In these wall reflected paths, l_0 denotes the distance in the free space for the 0th reflected path (no internal reflections), while l_r denotes the distance of once reflection inside the wall. Thus, the distance of nth reflected path can be expressed as $l_0+nl_r-nl_s$, where $n=1,2,....$

Provided that $k_0=2\pi/\lambda$ and $k_{\mathrm{r}}=2\pi\sqrt{\varepsilon_r}/\lambda$ are the wave number in free space and inside the wall, respectively, the initial electric field strength is denoted by E_0, the received electric field strength of the 0th and the nth reflected path could be given as

$$\begin{aligned} E_{r,0} &= E_0\left(\frac{\lambda}{4\pi l_0}\right)e^{-jk_0l_0}\Gamma^{'}, \\ E_{r,n} &= E_0\left(\frac{\lambda}{4\pi l_0}\right)e^{-jk_0l_0}(1+\Gamma^{'})(-\Gamma^{'})^{2n-1}(1-\Gamma^{'})e^{-jn(k_rl_r-k_0l_s)}, n\in\{1,2,...\}. \end{aligned} \tag{2.51}$$

Thus the total received electric field strength due to reflections can be derived as

$$\begin{aligned} E_r &= \sum_{n=0}^{\infty}E_{r,n} = E_0\left(\frac{\lambda}{4\pi l_0}\right)e^{-jk_0l_0}\left[\Gamma^{'}+\sum_{n=1}^{\infty}\left(1-\Gamma^{'2}\right)(-\Gamma^{'})^{2n-1}e^{-jn(k_rl_r-k_0l_s)}\right] \\ &= E_0\left(\frac{\lambda}{4\pi l_0}\right)e^{-jk_0l_0}\left[\Gamma^{'}+\left(\Gamma^{'}-\frac{1}{\Gamma^{'}}\right)\sum_{n=1}^{\infty}\left(\Gamma^{'2}e^{-j(k_rl_r-k_0l_s)}\right)^n\right] \\ &= E_0\left(\frac{\lambda}{4\pi l_0}\right)e^{-jk_0l_0}\Gamma^{'}\frac{1-e^{-j(k_rl_r-k_0l_s)}}{1-\Gamma^{'2}e^{-j(k_rl_r-k_0l_s)}}. \end{aligned} \tag{2.52}$$

Leveraging the Snell's refraction law $\sin\bar{\theta}=\sin\theta/\sqrt{\varepsilon_{\mathrm{r}}}$ in (2.23), we get

$$k_rl_r-k_0l_s=\frac{2\pi}{\lambda}\sqrt{\varepsilon_r}\frac{2l}{\cos\bar{\theta}}-\frac{2\pi}{\lambda}2l\tan\bar{\theta}\sin\theta=\frac{2\pi}{\lambda}2l\sqrt{\varepsilon_r-\sin^2\theta}. \tag{2.53}$$

Substituting (2.53) into (2.52) and dividing (2.52) by $E_0\left(\frac{\lambda}{4\pi l_0}\right)e^{-jk_0l_0}$, (2.49)-(2.50) are obtained.

Fig. 2.4 shows the first-order reflection coefficient amplitude of five different materials for TE and TM polarised incident waves under 1 GHz. We observe significant differences

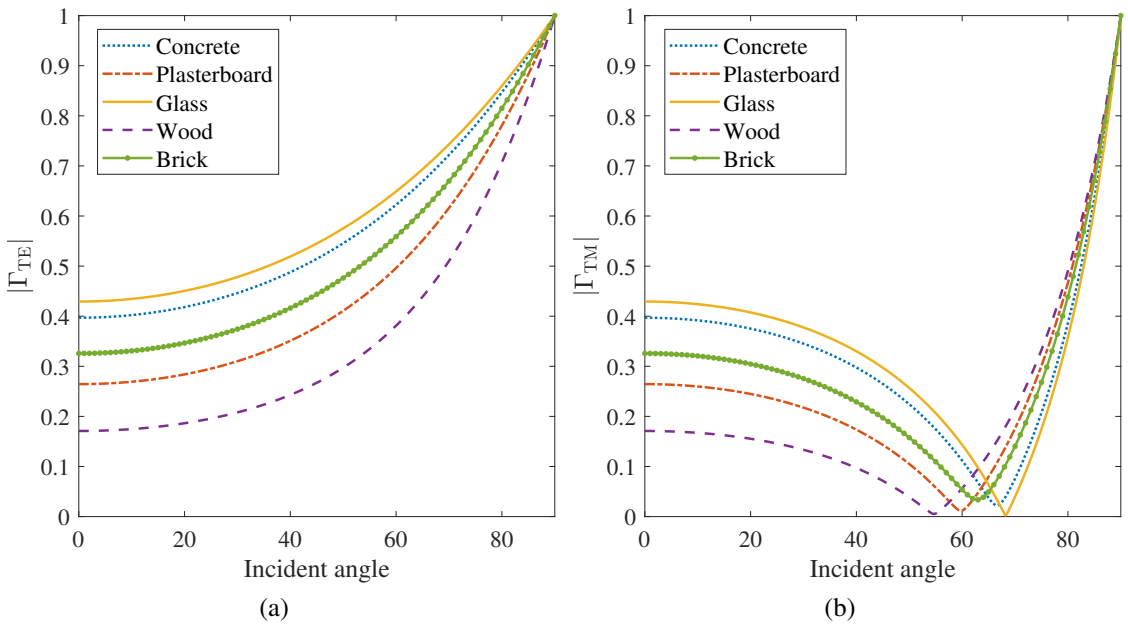

Fig. 2.4 The first-order reflection coefficient amplitude of five different single-layer materials for (a) TE and (b) TM polarised incident waves under 1 GHz.

between TE and TM polarisations in the first-order reflection coefficient amplitude when varying the incident angle from 0 to 90 degree.

Fig. 2.5 plots the multiple reflection coefficient amplitude versus concrete material's thickness for the TE and TM polarised 60-degree incident waves under 1 GHz, 6 GHz, 28 GHz. As the material thickness increases, the envelop of the multiple reflection coefficient first fluctuates and then gradually converges to a constant value. The convergence speed varies with the wavelength: the incident waves under 28 GHz converges fastest around 0.1 m, followed by the 6-GHz and 1-GHz waves converges around 0.3 m and 0.9 m, respectively. Besides, the fluctuation magnitude of the TM polarised incident waves are much severer than the TE polarised waves.

In Fig. 2.6, the multiple reflection coefficient amplitudes of five different materials for the TM polarised 60-degree incident waves under 6 GHz are depicted. The five materials are shown to have their inherent reflection characteristics. The reflection coefficient amplitudes fluctuates more slightly when the material's thickness becomes larger.

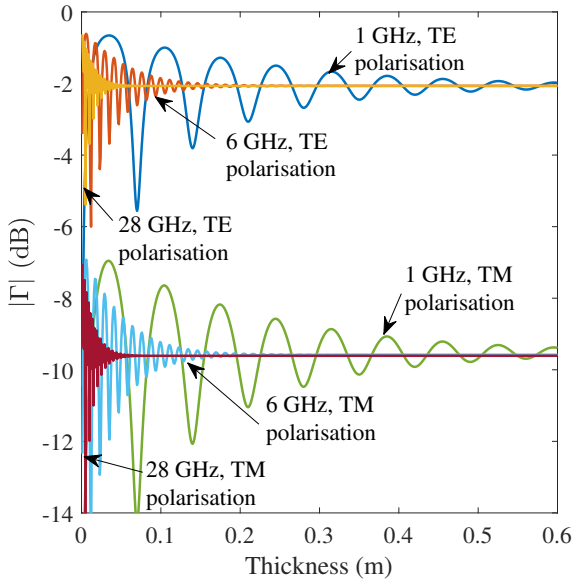

Fig. 2.5 The multiple reflection coefficient amplitudes of a concrete single-layer material for the TE and TM polarised 60-degree incident waves under 1 GHz, 6 GHz, 28 GHz.

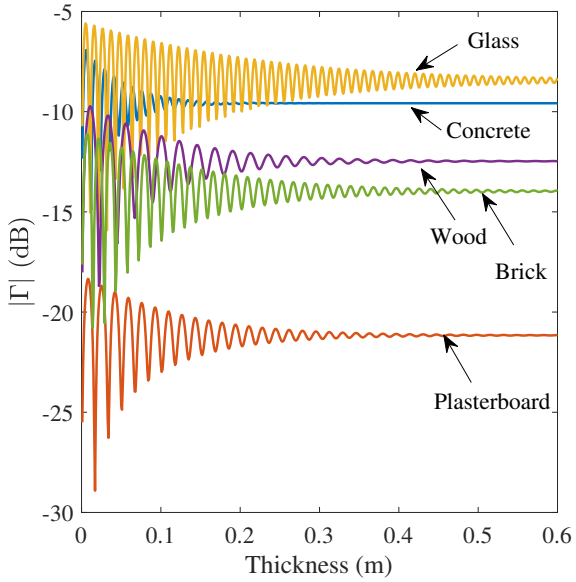

Fig. 2.6 The multiple reflection coefficient amplitudes of five different single-layer materials for the TM polarised 60-degree incident waves under 6 GHz.

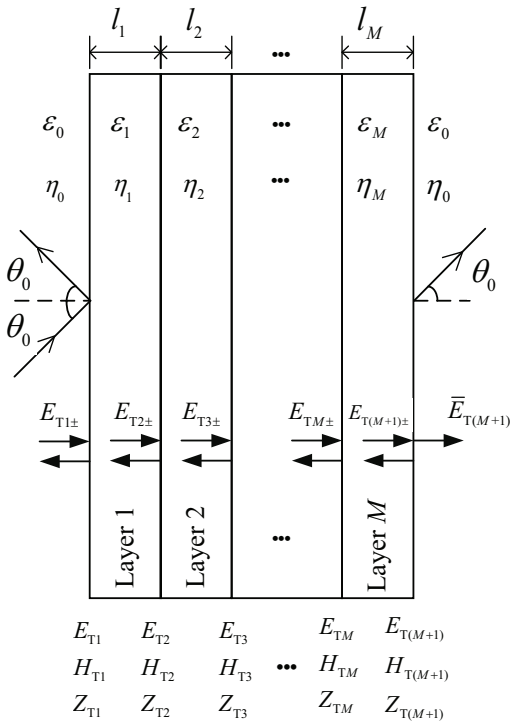

Fig. 2.7 Structure of a M-layered sandwich building material.

Sandwich materials: An iteration approach to deriving the reflection coefficient for an M-layer sandwich material that considers multiple internal reflections is given by [20]

$$\Gamma_{\text{sandwich}} = \frac{B/\eta_0 - C\eta_0}{2A + B/\eta_0 + C\eta_0}, \tag{2.54}$$

where

$$\begin{bmatrix} A & B \\ C & D \end{bmatrix} = \begin{bmatrix} A_1 & B_1 \\ C_1 & D_1 \end{bmatrix} \ldots \begin{bmatrix} A_m & B_m \\ C_m & D_m \end{bmatrix} \ldots \begin{bmatrix} A_N & B_N \\ C_N & D_N \end{bmatrix}, \tag{2.55}$$

$$\begin{aligned} A_m &= D_m = \cos(\zeta_m l_m), \\ B_m &= j\eta_m \sin(\zeta_m l_m), \\ C_m &= j\frac{\sin(\zeta_m l_m)}{\eta_m}, \\ k_m &= \frac{2\pi}{\lambda}\sqrt{\varepsilon_m}, \\ \zeta_m &= k_m \cos(\theta_m) = \frac{2\pi}{\lambda}\sqrt{\varepsilon_m - \sin^2\theta_0}, \end{aligned}$$

$$\eta_m = \begin{cases} \frac{120\pi}{\sqrt{\varepsilon_m}\cos\theta_m} = \frac{120\pi}{\sqrt{\varepsilon_m - \sin^2\theta_0}}, \text{ for TE polarisation,} \\ \frac{120\pi\cos\theta_m}{\sqrt{\varepsilon_m}} = 120\pi\sqrt{\frac{1}{\varepsilon_m} - \frac{\sin^2\theta_0}{\varepsilon_m^2}}, \text{ for TM polarisation.} \end{cases}$$

λ denotes the free-space wavelength, k_m and ζ_m denote the wave number in the mth layer and the propagation constant in the direction perpendicular to the mth layer, respectively, ε_m and l_m denote the complex relative permittivity and thickness of the mth layer, respectively, η_m denotes the transverse impedance in the mth layer according to the polarisation of the incident waves, and θ_0 is the incident angle.

Proof: Similarly as (2.37), the recursions for the total electric and magnetic fields shown in Fig. 2.7, which are continuous across each interface, are given by:

$$\begin{bmatrix} E_{\mathrm{T}m} \\ H_{\mathrm{T}m} \end{bmatrix} = \begin{bmatrix} \cos k_m l_m & j\eta_m \sin k_m l_m \\ j\eta_m^{-1}\sin k_m l_m & \cos k_m l_m \end{bmatrix} \begin{bmatrix} E_{\mathrm{T}(m+1)} \\ H_{\mathrm{T}(m+1)} \end{bmatrix}, m = M, M-1, ..., 1, \quad (2.56)$$

and initialised at the $(M+1)$st interface as follows:

$$\begin{bmatrix} E_{\mathrm{T}(M+1)} \\ H_{\mathrm{T}(M+1)} \end{bmatrix} = \begin{bmatrix} 1 \\ {\eta_0}^{-1} \end{bmatrix} E'_{\mathrm{T}(M+1)}, \quad (2.57)$$

Thus, the product of the propagation matrices is presented by (2.55), and

$$\begin{bmatrix} E_{\mathrm{T}1} \\ H_{\mathrm{T}1} \end{bmatrix} = \begin{bmatrix} A + B{\eta_0}^{-1} \\ C + D{\eta_0}^{-1} \end{bmatrix} E'_{\mathrm{T}(M+1)}, \quad (2.58)$$

Then, the overall reflection response is given by:

$$\Gamma_{\text{sandwich}} = \Gamma_1 = \begin{bmatrix} E_{\mathrm{T}1-} \\ H_{\mathrm{T}1+} \end{bmatrix} = \frac{\frac{E_{\mathrm{T}1}}{H_{\mathrm{T}1}} - \eta_0}{\frac{E_{\mathrm{T}1}}{H_{\mathrm{T}1}} + \eta_0}, \quad (2.59)$$

Substituting (2.58) and $A = D$ into (2.59), we get (2.54).

Fig. 2.8(a-b) show two typical sandwich materials used for the interior structures in office scenarios [45]. Their equivalent reflection coefficient amplitudes versus the incident

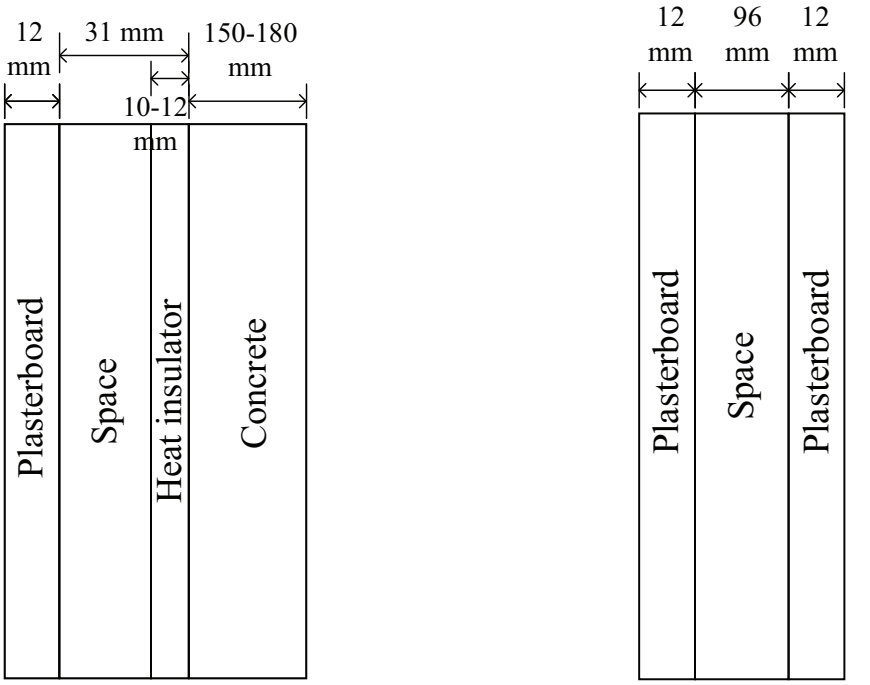

(a) Sandwich material A (b) Sandwich material B

Fig. 2.8 Two typical sandwich materials of interior structures in office scenarios [45].

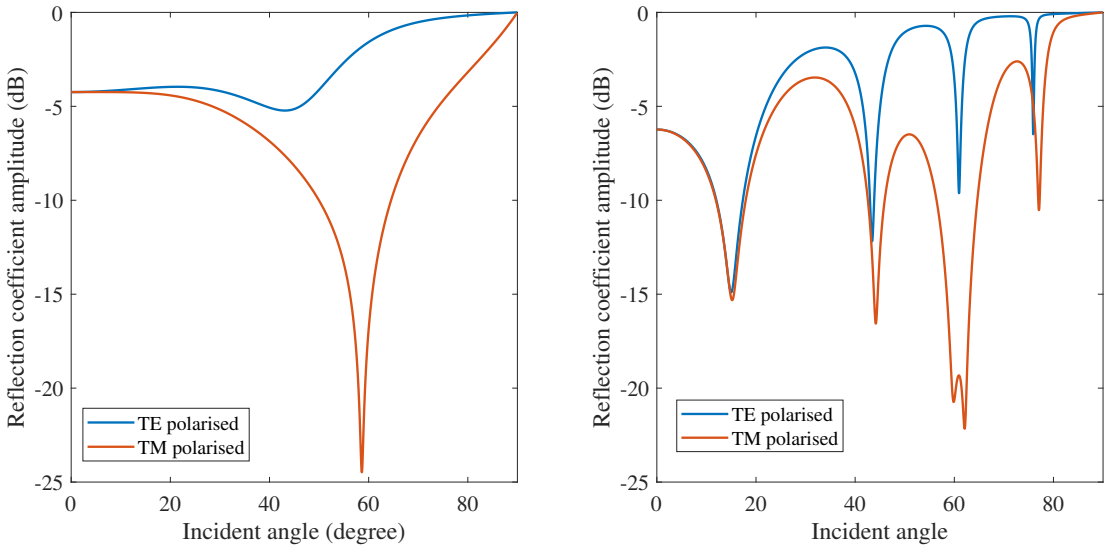

(a) (b)

Fig. 2.9 Reflection coefficient amplitude under 6 GHz (a) for sandwich material A, where the incident wave is either TE or TM polarised, $\varepsilon_1 = 2.94 - j0.1235$, $\varepsilon_3 = 1.3 - j0.3$ [53, 54], $\varepsilon_4 = 5.31 - j0.4166$, $[l_1, l_2, l_3, l_4] = [12, 21, 10, 180]$ mm; (b) for sandwich material B, where the incident wave is either TE or TM polarised, $\varepsilon_1 = \varepsilon_3 = 2.94 - j0.1235$, $[l_1, l_2, l_3] = [12, 96, 12]$ mm.

angle are presented in Fig. 2.9(a-b), respectively. We observe that the reflection coefficient amplitude of a sandwich material varies with the incident angle, which can be attributed to the interference among the EM waves reflected from all layers' interface changing with the incident angle. This variation with the incident angle becomes more dramatic for the thinner material B than for material A. Meanwhile, it is seen that the polarisation of the incident waves brings significant difference in the values of equivalent reflection coefficient amplitude, and that, for both material A and material B, the TE polarised incident waves result in larger reflection gain than the TM polarised incident waves.

2.3 Indoor MIMO Wireless Systems

In this section, several aspects of the indoor MIMO wireless systems are reviewed, including MIMO antenna arrays, indoor multipath channel modelling, and the capacity of MIMO multipath channels.

2.3.1 MIMO Antenna Arrays

It is known that a single antenna element provides very low directivity gain, since its radiation pattern is relatively wide. By assembling numerous radiating elements in an geometrical configuration, the physical dimensions of the antennas are enlarged, leading to good directive characteristics. This multi-element structure is referred to as an antenna array. Thus, to guarantee a fairly good wireless performance indoors, the indoor BSs need to be equipped with high-directional MIMO antenna arrays.

For the sake of simplicity and practicality, the elements of an antenna array are generally identical. The individual elements of an array may be of any form, such as, dipoles, loops, apertures, microstrips, horns, reflectors, and so on. The total field of an antenna array is dependent on the vector summation of the fields radiated from each individual antenna, assuming that the current in every antenna is the same and that the mutual coupling effects is negligible [71]. Alternatively, the total field of an array can be represented by the field of a single antenna located at the origin multiplied by a factor, which is widely referred to

as the array factor (AF). In order to offer a radiation pattern with high directivity, the fields from all antennas are expected to interfere constructively in a certain direction while interfere destructively in the remaining directions.

The following five factors can be adjusted to shape a desired overall radiation pattern [72, Ch 6]: 1) The geometrical configuration of the array: linear, planar, circular, spherical, etc. 2) The inter-antenna spacing: in most cases, set as an equal spacing of half wavelength. 3) The radiation pattern of each individual element. 4) The excitation amplitude of each individual element. 5) The excitation phase of each individual element.

A uniform array refers to the array whose elements are all with the same magnitude but each with a progressive phase. Uniform linear array (ULA) and uniform planar array (UPA) are two common MIMO antenna array examples.

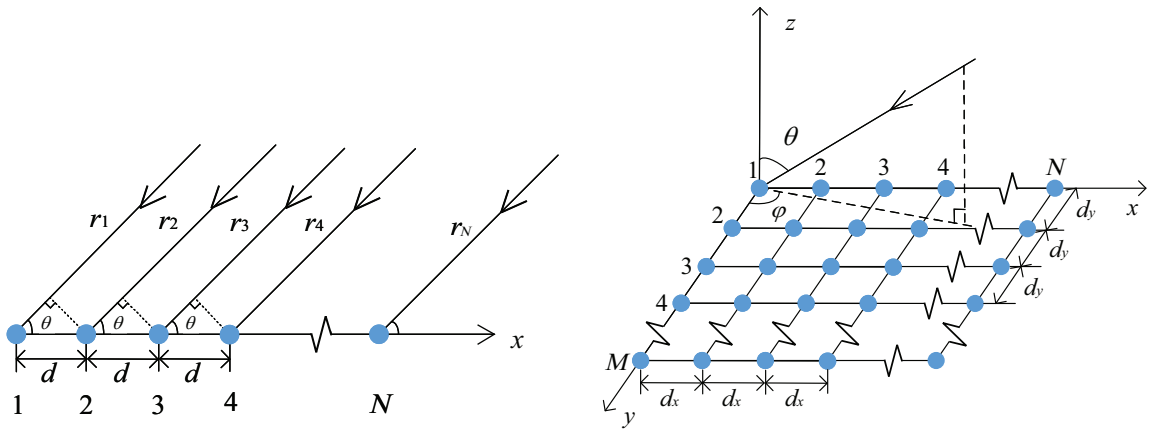

(a) (b)

Fig. 2.10 Geometries of (a) ULA and (b) UPA.

Figure 2.10(a) depicts the geometry of the EM waves from the angle θ impinging on an N-element ULA on x-axis with the inter-element spacing of d m. Assuming that γ denotes the progressive phase shift by which the current in each element leads the current of its preceding element, the AF is given by

$$\mathrm{AF}_{\mathrm{ULA}} = 1 + e^{-j(kd\cos\theta+\gamma)} + \ldots + e^{-j(N-1)(kd\cos\theta+\gamma)} = \sum_{n=1}^{N} e^{-j(n-1)(kd\cos\theta+\gamma)}, \quad (2.60)$$

Multiplying both sides of the first line of (2.60) with $e^{-jkd\cos\theta}$, we have

$$(\mathrm{AF_{ULA}})e^{-j(kd\cos\theta+\gamma)} = e^{-j(kd\cos\theta+\gamma)} + e^{-j2(kd\cos\theta+\gamma)} + ... + e^{-jN(kd\cos\theta+\gamma)}. \quad (2.61)$$

Subtracting (2.60) from (2.61), the AF becomes

$$\mathrm{AF_{ULA}} = \frac{e^{-jN(kd\cos\theta+\gamma)}-1}{e^{-j(kd\cos\theta+\gamma)}-1} = e^{-j(N-1)(kd\cos\theta+\gamma)/2}\frac{\sin(N(kd\cos\theta+\gamma)/2)}{\sin((kd\cos\theta+\gamma)/2)}. \quad (2.62)$$

If the reference point is located at the centre of the array, the AF is reduced to and normalised as

$$\mathrm{AF_{ULA}} = \frac{\sin(N(kd\cos\theta+\gamma)/2)}{N\sin((kd\cos\theta+\gamma)/2)}. \quad (2.63)$$

For small values of $(kd\cos\theta+\gamma)$, the AF can be approximated by

$$\mathrm{AF_{ULA}} \approx \frac{\sin(N(kd\cos\theta+\gamma)/2)}{N((kd\cos\theta+\gamma)/2)}. \quad (2.64)$$

The maximum occurs when

$$(kd\cos\theta+\gamma)/2 = 0, \Rightarrow \theta_m = \cos^{-1}\left(\frac{\lambda\gamma}{2\pi d}\right). \quad (2.65)$$

The 3-dB point for the AF occurs when

$$\frac{\sin(N(kd\cos\theta+\gamma)/2)}{N((kd\cos\theta+\gamma)/2)} = \frac{\sqrt{2}}{2}, \Rightarrow \theta_h = \cos^{-1}\left(\frac{\lambda}{2\pi d}\left(-\gamma \pm \frac{2.782}{N}\right)\right). \quad (2.66)$$

Then the half-power bandwidth of a symmetrical pattern is given by

$$\theta_{3\mathrm{dB}} = 2|\theta_m - \theta_h|. \quad (2.67)$$

Figure 2.10(b) depicts the geometry of the EM waves from the angle $\{\theta,\phi\}$ impinging on an $M\times N$-element UPA on $x-y$ plane with the inter-element spacing of $\{d_x,d_y\}$ m. Assuming γ_x and γ_y denote the progressive phase shift along x-axis and y-axis, respectively,

similarly as (2.63), the normalised AF is given by

$$\mathrm{AF_{UPA}} = \frac{\sin(N\left(kd_x \sin\theta \sin\phi + \gamma_x\right)/2)}{N\sin(\left(kd_x \sin\theta \sin\phi + \gamma_x\right)/2)} \frac{\sin(M\left(kd_y \sin\theta \cos\phi + \gamma_y\right)/2)}{M\sin(\left(kd_y \sin\theta \cos\phi + \gamma_y\right)/2)} \tag{2.68}$$

It should be noted that γ_x and γ_y are theoretically independent of each other, but practically, they are jointly adjusted to make sure $\frac{\sin(N(kd_x \sin\theta \sin\phi+\gamma_x)/2)}{N\sin(\left(kd_x \sin\theta \sin\phi+\gamma_x\right)/2)}$ and $\frac{\sin(M\left(kd_y \sin\theta \cos\phi+\gamma_y\right)/2)}{M\sin(\left(kd_y \sin\theta \cos\phi+\gamma_y\right)/2)}$ in $\mathrm{AF_{UPA}}$ direct their maxima towards the same direction, i.e., the main beam direction [72, Ch 6]. Suppose the main beam is directed along $\theta = \theta_0$ and $\phi = \phi_0$, it is required that

$$\begin{aligned} \gamma_x &= -kd_x \sin\theta_0 \sin\phi_0, \\ \gamma_y &= -kd_y \sin\theta_0 \cos\phi_0. \end{aligned} \tag{2.69}$$

Accordingly, θ_0 and ϕ_0 are derived as

$$\begin{aligned} \tan\phi_0 &= \frac{d_y\gamma_x}{d_x\gamma_y}, \\ \sin^2\theta_0 &= \left(\frac{\gamma_x}{kd_x}\right)^2 + \left(\frac{\gamma_y}{kd_y}\right)^2. \end{aligned} \tag{2.70}$$

Thus, the maxima are located at the directions $\{\theta, \phi\}$ satisfying:

$$\begin{aligned} kd_x\left(\sin\theta\sin\phi - \sin\theta_0\sin\phi_0\right) &= \pm 2m\pi, m = 0,1,2,... \\ kd_y\left(\sin\theta\cos\phi - \sin\theta_0\cos\phi_0\right) &= \pm 2n\pi, n = 0,1,2,... \end{aligned} \tag{2.71}$$

Then, the solutions of $\{\theta, \phi\}$ are derived as

$$\phi = \tan^{-1}\left(\frac{\sin\theta_0\sin\phi_0 \pm m\lambda/d_x}{\sin\theta_0\cos\phi_0 \pm n\lambda/d_y}\right), \tag{2.72}$$

$$\theta = \sin^{-1}\left(\frac{\sin\theta_0\sin\phi_0 \pm m\lambda/d_x}{\sin\phi}\right) = \sin^{-1}\left(\frac{\sin\theta_0\cos\phi_0 \pm n\lambda/d_y}{\cos\phi}\right), \tag{2.73}$$

where $m = n = 0$ corresponds to the main lobe, and the remaining $\{m, n\}$ combinations correspond to the grating lobes.

2.3.2 Indoor Multipath Channel Modelling

In a typical indoor environment, EM waves interact frequently with the physical objects through reflection, refraction, diffraction and diffuse scattering. As a result, many copies of the transmitted signal, known as the multipath components, are produced, which differ from the transmitted signal in power, delay, frequency and phase shift. The multipath components and the line-of-sight (LOS) path components will jointly influence indoor wireless performance. Hence, the multipath components should be well considered in channel modelling. Generally, indoor multipath channel models contain two categories: deterministic channel models, stochastic channel models.

Deterministic Channel Modelling

Deterministic channel model makes best use of the geographical and morphological information from a database to describe the EM wave propagation process in a specific site. For indoor environments, the location, shape, and dielectric and conductive properties of surrounding building structures need to be taken into account when determining the field strength at all points and times. This modelling approach requires large computational effort and has inherent errors due to the inaccuracies in the underlying database. Nevertheless, it can be easily used in computer simulations, omitting costly and complicated measurement campaigns.

Ray launching techniques can reveal the channel characteristics, e.g., coverage and delay spread, in the whole environment, for many different receiver positions and a given transmitter position. Specifically, the transmit antenna sends out rays in the three-dimensional (3D) spatial angular space of 4π. Each ray propagates towards a specific direction until it either hits the receiver or becomes too weak to be significant (e.g., drops below the noise level) [73]. The number of launched rays is chosen to strike a balance between the accuracy and the complexity.

Ray-tracing techniques determine all rays that go from one transmitter location to one receiver location. Ray tracing approximates the propagation of EM waves by treating the wavefronts as simple particles and assuming the energy to be radiated through ray tubes

infinitesimally [74]. Thus, the reflection, diffraction, and scattering effects on the wavefront are approximated using simple geometric equations instead of Maxwell's more complex wave equations [75, 76]. The well-known two-ray model is the simplest ray-tracing based channel model where the single wall reflection or ground reflection dominates the multipath effects [76, 77], which facilitates analytical tractability for providing guidelines.

Stochastic Channel Modelling

Deterministic channel models discussed above require massive site-specific information, which are often unavailable in practice. Instead of correctly predicting the impulse response in one specific location, stochastic channel models can statistically predict the probability density function (PDF) of channel impulse response over a large area [73, 78]. The stochastic models are sometimes derived from measurements, which may lead to inaccuracies due to the finite measurement times and unavoidable measurement errors. However, although the stochastic models are simplified probabilistic models, they have been highly useful and creative for providing insights into the design and comparison of wireless systems, especially used as the starting points of high-level analysis. Note that it is important to understand the robustness of the results based on these models [79].

A very simple example is the Raleigh fading model. Theoretically, both the in-phase and the quadrature-phase components are the sum of many random variables, none of which are dominant. The PDF of such a sum follows a Gaussian distribution following the central limit theorem (CLT), regardless of the exact PDF of the constituent amplitudes. Hence, the amplitude of the total signal has a Rayleigh distribution [76], and the phase of the total signal obeys the uniform distribution in the range of 0 and 2π. The Rayleigh fading model depends only on a single parameter, the mean received power, making the complete signal statistics easily known and the error probabilities presented in closed-form [80]. Nonetheless, this model is oversimplified and inaccurate for indoor scenarios [23].

A more practical example is the Rician fading model, which describes a random multipath channel model with a dominant component, e.g., a LOS component, a dominant specular component, or their superposition [78, 80]. The in-phase component has a non-zero-mean

Gaussian distribution and the quadrature-phase component has a zero-mean Gaussian distribution, whilst both have equal variance. The phase distribution of the total signal is changed duo to the presence of a dominant component. For an extreme example, when the dominant component is very strong, the phase distribution converges to a delta function, because the phase of the total signal must be very close to the phase of the dominant component [73]. One of the important parameters of Rician fading model is Rician factor K, which determines the power ratio of the dominant multipath component to the diffused components and is therefore used as a relative measure of the severity of fading [23, 76]. For $K \to 0$, the power of dominant multipath component approaches 0. The model approximates Rayleigh fading model, and the channel experiences severe fading. While for a large K, the model approximately has a Gaussian distribution and the channel experiences mild fading. It has been verified through measurement that the value of the Rician factor is a function of LOS path length [81]. The detailed results of the Rician factor are listed in Table. 2.3.

Table 2.3 The fitted Rician factor K (dB) versus LOS path length d (m) under WINNER scenarios [81]

Scenario	Applicability	Frequency (GHz)	K (dB) versus d (m)
A1	Indoor small office	5.25	$K = 8.7 + 0.051d$
B1	Urban micro-cell	5	$K = 3 + 0.0142d$
B3	Indoor hotspot	-	$K = 6 - 0.26d$
C1	Suburban macro-cell	-	$K = 17.1 - 0.0205d$
D1	Rural macro-cell	5.25	$K = 3.7 + 0.019d$

Another more generalised model is two-wave with diffuse power (TWDP) fading model, which is due to the interference of two strong radio signals and numerous relative small signals. The Rayleigh fading and Rician fading models are special cases of TWDP models [78, Table III]. The PDF of a TWDP model can sometimes be approximated by Rayleigh and Rician distribution when the product of the power ratio of specular to diffuse components and the two-wave parameter meets certain requirements [78, (20), (21)].

Generally speaking, deterministic models are preferable in specific sites for network planning and system deployment, while stochastic models are employed for the design and

comparison of systems. In addition, the combination of the deterministic and stochastic models can enhance the efficiency of a model, that is, the large-scale averaged power is obtained from deterministic models, while the variations within an averaging area are modelled stochastically [73].

2.3.3 Capacities of MIMO Multipath Channels

We consider the narrowband downlink transmission from the N_{T}-antenna BS to the N_{R}-antenna UE. The MIMO system between them is then built as

$$\mathbf{y} = \mathbf{H}\mathbf{x} + \mathbf{n}, \tag{2.74}$$

where $\mathbf{x} \in \mathbb{C}^{N_{\mathrm{T}}}$, $\mathbf{y} \in \mathbb{C}^{N_{\mathrm{R}}}$, and $\mathbf{n} \in CN(0, N_0\mathbf{I}_{N_{\mathrm{R}}})$ denote the transmit signal, received signal, and the white Gaussian noise, respectively. The channel matrix $\mathbf{H} \in \mathbb{C}^{N_{\mathrm{R}} \times N_{\mathrm{T}}}$ can be either deterministic or faded.

Suppose that the N_{T} and N_{R} antennas at the BS and UE are all placed in ULAs, and that an arbitrary number of propagation paths between the ULAs at the BS and UE, the MIMO multipath channel is constructed by

$$\mathbf{H} = \sum_i a_i \sqrt{N_{\mathrm{T}} N_{\mathrm{R}}} \exp\left(-\frac{j2\pi r_i}{\lambda}\right) \mathbf{e}_{\mathrm{R}}\left(\Omega_{\mathrm{R}i}\right) \mathbf{e}_{\mathrm{T}}\left(\Omega_{\mathrm{T}i}\right)^{\dagger}, \tag{2.75}$$

where

$$\mathbf{e}_{\mathrm{R}}(\Omega_{\mathrm{R}i}) := \frac{1}{\sqrt{N_{\mathrm{R}}}} \left[\ 1, \exp\left(-j2\pi\Delta_{\mathrm{R}}\Omega_{\mathrm{R}i}\right), ..., ..., \exp\left(-j2\pi\left(N_{\mathrm{R}}-1\right)\Delta_{\mathrm{R}}\Omega_{\mathrm{R}i}\right)\ \right]^{\dagger}, \tag{2.76}$$

$$\mathbf{e}_{\mathrm{T}}(\Omega_{\mathrm{T}i}) := \frac{1}{\sqrt{N_{\mathrm{T}}}} \left[\ 1, \exp\left(-j2\pi\Delta_{\mathrm{T}}\Omega_{\mathrm{T}i}\right), ..., ..., \exp\left(-j2\pi\left(N_{\mathrm{T}}-1\right)\Delta_{\mathrm{T}}\Omega_{\mathrm{T}i}\right)\ \right]^{\dagger}, \tag{2.77}$$

where the ith path with the attenuation of a_i and the length of r_i, makes the angle of departure (AOD) $\phi_{\mathrm{T}i}$ at the transmit ULA and the angle of arrival (AOA) $\phi_{\mathrm{R}i}$ at the receive ULA, $\Omega_{\mathrm{T}i} = \cos\phi_{\mathrm{T}i}$, $\Omega_{\mathrm{R}i} = \cos\phi_{\mathrm{R}i}$, Δ_{T} and Δ_{R} are the inter-antenna spacing normalised by the

wavelength at the transmit and receive ULAs, respectively, and $(\cdot)^{\dagger}$ denotes the conjugate transpose of a matrix or a vector.

The capacity of the MIMO channel can be computed by decomposing the vector channel into a set of parallel, independent scalar sub-channels. The channel matrix $\mathbf{H}$ has a singular value decomposition (SVD) formed by

$$\mathbf{H} = \mathbf{U}\mathbf{Z}\mathbf{V}^{\dagger}, \tag{2.78}$$

where $\mathbf{U} \in \mathbb{C}^{N_{\mathrm{R}} \times N_{\mathrm{R}}}$ and $\mathbf{V} \in \mathbb{C}^{N_{\mathrm{T}} \times N_{\mathrm{T}}}$ are (rotation) unitary matrices and $\mathbf{Z} \in \mathbb{C}^{N_{\mathrm{R}} \times N_{\mathrm{T}}}$ is a rectangular matrix whose diagonal elements are non-negative real numbers and whose off-diagonal elements are zero. The diagonal elements $\zeta_1 \geq \zeta_2 \geq ... \geq \zeta_{n_{\min}}$ are the ordered singular values of the matrix $\mathbf{H}$, where $n_{\min} = \min(N_{\mathrm{T}}, N_{\mathrm{R}})$. Since $\mathbf{H}\mathbf{H}^{\dagger} = \mathbf{U}\mathbf{Z}\mathbf{Z}^{\dagger}\mathbf{U}^{\dagger}$, the squared singular values ζ_i^2 are the eigenvalues of the matrix $\mathbf{H}\mathbf{H}^{\dagger}$ and also of $\mathbf{H}^{\dagger}\mathbf{H}$. Consequently, the channel matrix can be expressed as

$$\mathbf{H} = \sum_{i=1}^{n_{\min}} \zeta_i \mathbf{u}_i \mathbf{v}_i^{\dagger}, \tag{2.79}$$

where $\mathbf{u}_i$ and $\mathbf{v}_i$ are the ith column of $\mathbf{U}$ and $\mathbf{V}$, respectively.

Defining $\tilde{\mathbf{x}} = \mathbf{V}^{\dagger}\mathbf{x}$, $\tilde{\mathbf{y}} = \mathbf{U}^{\dagger}\mathbf{y}$, $\tilde{\mathbf{n}} = \mathbf{U}^{\dagger}\mathbf{n}$, (2.74) becomes

$$\tilde{\mathbf{y}} = \mathbf{Z}\tilde{\mathbf{x}} + \tilde{\mathbf{n}}. \tag{2.80}$$

Alternatively,

$$\tilde{y}_i = \zeta_i \tilde{x}_i + \tilde{n}_i. \tag{2.81}$$

Each of the the squared singular values ζ_i^2 corresponds to an eigenmode of the channel, also referred to as an eigenchannel. Each non-zero eigenchannel can support a data stream. In this manner, the MIMO channel can support the spatial multiplexing of multiple streams.

Deterministic MIMO Channels

When the channel is deterministic and the transmitter knows the channel, it can allocate different amounts of power to the different eighenchannels depending on their strengths via water filling algorithm, i.e.,

$$C = \sum_{i=1}^{n_{\min}} \log_2 \left(1 + \frac{P_i^* \zeta_i^2}{N_0}\right), \tag{2.82}$$

where $P_1^*, \ldots, P_{n_{\min}}^*$ are the water filling power allocations and given by

$$P_i^* = \left(q - \frac{N_0}{\zeta_i^2}\right)^+, \tag{2.83}$$

in which q is chosen to meet the power constraint of $\sum_i P_i^* = P$.

In the high signal-to-noise ratio (SNR) regime, the equal power allocation strategy for the non-zero eighenchannels is asymptotically optimal due to the relatively deep water filling level. The capacity is accordingly approximated by

$$C \approx \sum_{i=1}^{k} \log_2 \left(1 + \frac{P\zeta_i^2}{kN_0}\right) \approx k \log_2 \frac{P}{N_0} + \sum_{i=1}^{k} \log_2 \left(\frac{\zeta_i^2}{k}\right), \tag{2.84}$$

where k is the number of non-zero ζ_i, which is equal to the rank of the channel $\mathbf{H}$. When the channel is full rank, $k = n_{\min}$. k can also be interpreted as the number of spatial degrees of freedom per second per Hertz. Thus, the capacity scales like $k \log_2 \frac{P}{N_0}$ bit/s/Hz.

Given that

$$\frac{1}{k} \sum_{i=1}^{k} \log_2 \left(1 + \frac{P}{kN_0} \zeta_i^2\right) \leq \log_2 \left(1 + \frac{P}{kN_0} \left(\frac{1}{k} \sum_{i=1}^{k} \zeta_i^2\right)\right),$$

by Jensen's inequality and

$$\sum_{i=1}^{k} \zeta_i^2 = \mathrm{Tr}\left[\mathbf{H}\mathbf{H}^\dagger\right] = \sum_{i,j} \left|h_{ij}\right|^2,$$

where $\mathrm{Tr}(\cdot)$ denotes the trace of a matrix, and $h_{i,j}$ denotes the (i,j)th element of the channel matrix $\mathbf{H}$. It is found that the highest value of the capacity at high SNR is obtained when all the singular values are equal. In other words, the singular values are spread out evenly. The distribution of the singular values can be described by the conditional number of the channel matrix, which is defined by $\frac{\max_i \zeta_i}{\min_i \zeta_i}$ [79, Ch 7]. The channel matrix is said to be well-conditioned if the condition number is close to 1.

In the low SNR regime, the optimal policy is to allocate power only to the strongest eigenchannel. By using the approximation of $\log_2(1+x) \approx x \log_2 e$ for a small x, the capacity is approximated by

$$C \approx \frac{P}{N_0} \left(\max_i \zeta_i^2 \right) \log_2 e, \tag{2.85}$$

yielding the power gain of $\max_i \zeta_i^2$.

Fast Fading MIMO Channels

When the channel experiences independent and identically distributed (i.i.d.) Rayleigh fast fading channel and the transmitter does not know the channel, the optimal solution results from allocating equal power to all the eigenchannels [79, (8.12)], i.e.,

$$\begin{aligned} C &= \mathbb{E}\left[\log_2 \det \left(\mathbf{I}_{N_\mathrm{R}} + \frac{P}{N_\mathrm{T} N_0} \mathbf{H}\mathbf{H}^\dagger \right) \right] \\ &= \sum_{i=1}^{n_{\min}} \mathbb{E}\left[\log_2 \left(1 + \frac{P}{N_\mathrm{T} N_0} \zeta_i^2 \right) \right], \end{aligned} \tag{2.86}$$

where $\mathbb{E}(\cdot)$ denotes the expectation.

In the high SNR regime, the capacity is approximated by

$$C \approx n_{\min} \log_2 \frac{P}{N_\mathrm{T} N_0} + \sum_{i=1}^{n_{\min}} \mathbb{E}\left[\log_2 \zeta_i^2 \right], \tag{2.87}$$

where $\mathbb{E}\left[\log_2 \zeta_i^2\right] > -\infty$ for all i. Hence, the full $n_{\min}$ degrees of freedom is attained, and the capacity scales like $n_{min} \log_2 \frac{P}{N_0}$ bit/s/Hz.

In the low SNR regime, the capacity is approximated by

$$C \approx \sum_{i=1}^{n_{\min}} \frac{P}{N_{\mathrm{T}} N_0} \mathbb{E}\left[\zeta_i^2\right] \log_2 e = \frac{P}{N_{\mathrm{T}} N_0} \mathbb{E}\left[\mathrm{Tr}\left[\mathbf{H}\mathbf{H}^{\dagger}\right]\right] \log_2 e = N_{\mathrm{R}} \frac{P}{N_0} \log_2 e. \tag{2.88}$$

Hence, at low SNR, the N_{R} by N_{T} system can only provide a power gain of N_{R} over a single-antenna system. This is attributed to the fact that the channel knowledge is unknown for the transmitter so that the transmit beamforming cannot add the transmit signals constructively, while the receiver can use the receive beamforming to combine the received signals coherently [79, Ch 8].

When the channel experiences correlated Rayleigh fading channel and the transmitter does not know the channel, the channel can be reconstructed by

$$\mathbf{H}' = \Psi^{\mathrm{R}} \mathbf{H} \Psi^{\mathrm{T}}, \tag{2.89}$$

using the assumed fading correlation structure in [82], where Ψ^{T} and Ψ^{R} denote the fading correlations at the transmitter and at the receiver, respectively. It is found that the capacity of correlated Rayleigh fading channel

$$C' = \mathbb{E}\left[\log_2 \det\left(\mathbf{I}_{N_{\mathrm{R}}} + \frac{P}{N_{\mathrm{T}} N_0} \mathbf{H}' \mathbf{H}'^{\dagger}\right)\right] \tag{2.90}$$

will be always smaller than the capacity of i.i.d. fading channel in (2.86) at any SNR, indicating that fading correlation will always reduce capacity over the entire range of SNRs [82]. Meanwhile, as the number of antennas increases at both transmitter and receiver, the difference between the capacities in (2.86) and (2.90) becomes more pronounced [82, Fig. 3].

2.4 Summary

In section 2.1 and 2.2, the EM and physical properties of building materials, and how these properties affect the reflection characteristics of building materials have been reviewed.

It is found that the existing works mainly focus on measuring or simulating the signal attenuations, reflection coefficients, and relative permittivities of common building materials. These experimental results are only applicable to the measured building materials or their similar substitutes under a specific frequency band, which however cannot be generalised to a material with different EM and physical properties or working under a different frequency band. The schemes for evaluating the wireless friendliness of building materials needs to be universally applicable to a variety of materials working in a wide frequency range. It will be useful to establish the analytical relationship between the EM and physical parameters of a building material and the indoor wireless performance, because, compared with measurement campaigns, the analytical relationship facilitates a faster and more economic way of predicting how friendly a building material is to indoor wireless communications and obtaining the optimal values of the EM and physical parameters.

In Section 2.3, the MIMO antenna arrays and indoor multipath channel modelling adopted in the indoor MIMO wireless systems, and the capacities of MIMO multipath channel have been reviewed. However, as far as the author knows, there exists no analytically tractable indoor MIMO channel model that explicitly incorporates the EM and physical properties of a building material, which is an important prerequisite for constructing the analytical relationship required to reveal the impact of the EM and physical properties of a building material on the indoor wireless performance.

Chapter 3

Contributions of the Thesis

This thesis leads to the pioneering research of establishing a systematic framework to evaluate the impact of EM and physical properties of building materials on indoor wireless performance, which has laid a solid foundation for subsequent research on the impacts of the diversified internal structure of building materials on their wireless friendliness. The general idea of creating a wireless friendliness evaluation scheme is to first construct a channel model that incorporates the impact of building materials on the indoor EM wave propagations, then design an appropriate evaluation metric, and finally propose an evaluation approach. To the best of our knowledge, this is the first attempt to explore the potential improvement of indoor wireless capacity from the perspective of selecting and designing building materials. The outcomes of this thesis would enable appropriate design and/or selection of building materials for building designers, e.g. civil engineers and architects, and provides necessary environmental information for communications engineers.

The main contributions of this thesis are briefly summarised as follows, which will be embodied in the following Papers I-III:

- A new two-ray channel model and a new multipath channel model that incorporate the LOS path and the wall reflection (WR) path are proposed for indoor LOS MIMO downlink transmissions. For the first time, the relative permittivity (EM property) and thickness (physical property) of building materials are encapsulated into the channel models through the reflection coefficient of the building material.

- The relationship between the relative permittivity and thickness of building materials and the MIMO channel capacity is analytically obtained, revealing the significant influence of the relative permittivity and thickness on indoor wireless capacity. By exploiting the expressions of indoor wireless capacity and their asymptotic forms, four simple and effective metrics used for evaluating the wireless friendliness of building materials are proposed, i.e., the spatially averaged capacity, the spatially averaged logarithmic eigenvalue sum (LES), the spatially averaged logarithmic eigenvalue product (LEP), and the upper-bound outage probability, which are all over the room of interest.

- The evaluation schemes for the wireless friendliness of building materials are developed. The optimal values of the relative permittivity and thickness of a building material that maximise the indoor spatially averaged capacity are obtained, providing guidance on the selection and/or design of a building material accordingly, and thus paving the way for wireless friendly architectural design.

- The effects of the WR from building materials are investigated and found to exaggerate the unevenness of the per-antenna power distribution over the precoded transmit antenna array, especially for the BS deployed near a wall. The impacts of the building material's relative permittivity and thickness on this power distribution are analysed, providing guidelines on how to select and/or design building material to alleviate the unevenness of per-antenna power distribution and thus maintain a high RF power amplifier efficiency.

Note that all the simulations in Papers I-III are done with Matlab solvers and that all the channel models in Papers I-III are 2D models without considering the reflections from side/opposite walls.

The main ideas expressed in the following Papers I-III are the results of discussions among all the authors. The author of this thesis plays a major role as the first author of Papers I-III, working on problem formulation, mathematical modelling and analysis, algorithm design, verifying analytical derivations by simulations, and paper writing. Dr. Jiliang Zhang

provides guidance in the analytical derivations and simulation realisations. Prof. Xiaoli Chu and Prof. Jie Zhang supervise the contents and significance of these research. All authors comment on the technical issues and help polish the manuscripts.

3.1 Papers Included in the Thesis

Paper I: How Friendly are Building Materials as Reflectors to Indoor LOS MIMO Communications?, Yixin Zhang, Chen Chen, Songjiang Yang, Jiliang Zhang, Xiaoli Chu, and Jie Zhang. This paper has been published in IEEE Internet of Things Journal, Volume: 7, Issue: 9, Pages: 9116-9127, Sept. 2020. Date of Publication: 29 Jun. 2020.

In the first paper, our objective is to evaluate the wireless friendliness of a building material by studying the impact of the EM and physical properties of building materials, i.e., their relative permittivity and thickness, on indoor wireless capacity. For the first time, we investigate the indoor capacity from the perspective of building material design. The outcomes of this work would enable appropriate selection/design of building materials during building design, thus enhancing the capacity of indoor LOS MIMO communications.

To be specific, we originally propose a new indoor multipath channel model considering the WRs from a building material. This model is created based on the distance-dependant Rician fading model, which incorporates the deterministic part (i.e., the LOS path and the WR path) and the random part (i.e., other multipath components). The WR path is taken into account to capture the impact of building materials on the indoor wireless propagation channel. Then, we derive the squared singular values of its deterministic part and the marginal probability distribution function (MPDF) of an unordered squared singular value in closed forms, based on which the ergodic capacity of the proposed channel is derived by taking the expectation over an unordered squared singular value. These analytical expressions reveal the relationship between the indoor wireless capacity and the relative permittivity and thickness of the building material. Next, to evaluate how friendly a building material is to indoor communications, we build a two-dimensional (2D) Cartesian coordinate system inside a room and take dense sample points spatially evenly distributed throughout the room. The

spatially averaged capacity over the room of interest is designed as a metric for measuring the wireless friendliness of a building material. A higher spatially averaged capacity corresponds to a better wireless friendliness of a building material. Moreover, the impact of the directivity of the BS antenna array on the indoor spatially averaged capacity is considered.

Finally, in numerical results performed at 6 GHz, we show how the wireless friendliness of a building material change with its relative permittivity and thickness, and obtain their optimal values that maximise the indoor spatially averaged capacity for both the omnidirectional and directional BS antenna arrays. Monte Carlo simulation results validate the correctness of analytical results. We find that the difference between the capacity of the proposed channel that considers both LOS and WR paths and the capacity of the Rician channel that only considers the LOS path is substantial, indicating the impact of the WR path that characterises the EM and physical properties of building materials is non-negligible for indoor LOS MIMO communications. We also find that the impact of relative permittivity on a material's wireless friendliness is much greater that the impact of thickness. The envelope of the spatially averaged capacity curve presents an upward trend against the material's relative permittivity under the BS-distance of 3/4 wavelength. For a given permittivity, as the wall thickness increases, the spatially averaged capacity first fluctuates with it under a decreasing envelope and gradually converges to a constant value when the thickness goes beyond 0.25 m. A tiny lapse in the relative permittivity or thickness will significantly change the spatially averaged capacity by nearly 13.5% and 4.8%, respectively, for the omnidirectional and directional BS antenna arrays. Therefore, the combinations of the relative permittivity and thickness are worthy of careful consideration in the selection and/or design of building materials to avoid the risk of reducing indoor wireless capacity.

Note that the channel model proposed in Papers I is essentially different from the TWDP fading model in [78]. The channel model in (9-13) in Paper I considers both the large-scale fading and the small-scale fading, where for large-scale fading, the distance-dependent power decay and distance-dependent phase rotations in the specular LOS and WR paths are incorporated, and for small-scale fading, the multipath components following Gaussian distributions are included. However, [78] only discussed the small-scale TWDP fading

experienced by a receiver in relatively confined area, and talked nothing about the impact of distances.

Paper II: Lower-bound Capacity Based Wireless Friendliness Evaluation for Walls as Reflectors, Yixin Zhang, Jiliang Zhang, Xiaoli Chu, and Jie Zhang. This paper has been published in IEEE Transactions on Broadcasting, Volume: 67, Issue: 4, Pages: 917-924, Dec. 2021. Date of Publication: 27 Sep. 2021.

In the second paper, we aim to design three new metrics to facilitate fast and simple wireless friendliness evaluations of a building material. By exploiting the lower-bound capacity of a two-ray channel model that comprises of the LOS path and the WR path, the influence of the BS transmission power on a material's wireless friendliness can be removed. Compared with the metric in Paper I, the three new metrics no longer require the calculation of the following four parameters: the BS transmit SNR, the power ratio of the LOS and WR paths to the other multipath components, and the two eigenvalues of the two-ray channel, which thus reduces the complexity of evaluating the wireless friendliness of a building material. The proposed approach based on the three new metrics will enable architects and civil engineers to quickly select building materials according to their wireless friendliness.

Since the capacity of the two-ray channel comprising of the LOS path and the WR path and the capacity of a multipath channel that incorporates other multipath components in addition to the LOS path and the WR path are proved to have the same monotonicity, it is reasonable to study a wall material's wireless friendliness based on the capacity of the two-ray channel. We first derive the lower-bound capacity per unit bandwidth in the medium and high SNR regimes in closed-form, and find that the LES and LEP therein can be used to separate the BS transmit SNR from the interference between the LOS path and the WR path that determines the wireless friendliness of a wall material. On this basis, three new metrics have been proposed, i.e., the spatially averaged LES, the spatially averaged LEP, and the upper-bound outage probability of the room, for evaluating the wall material's wireless friendliness. The first two metrics constitute as parts of the lower-bound capacity. The larger their values are, the friendlier the wall material is to wireless communications. The third metric can be leveraged to quickly evaluate the capacity at a UE position against a

given downlink capacity threshold and reveal the percentage of all possible UE locations not achieving the target downlink capacity, whose value can be calculated by the cumulative distribution function (CDF) of the UE location-specific LES and LEP in the medium and high SNR regimes, respectively. A lower value means a better wireless signal coverage inside the room, indicating that the wall material is more wireless-friendly.

The three new metrics are compared with respect to their advantages, limitations, and applicability. Generally, the spatially averaged LES and spatially averaged LES of a room are preferred when evaluating the impact of a room setting factor on the indoor wireless capacity and obtaining its optimal configuration. The upper-bound outage probability of a room should be adopted when a room setting factor needs to be properly set to meet the capacity requirement. In addition, numerical results conducted at 6 GHz validate the effectiveness of the three proposed metrics under different room sizes and aspect ratios, wall permittivities and conductivities, wall thicknesses, and BS-wall distances.

In conclusions, the impact of the thickness of a wall material is far weaker than that of its relative permittivity. Compared with the imaginary part of a wall material's relative permittivity, its real part exerts a greater impact on the three proposed metrics. The real part of a wall material's relative permittivity determines the upward or downward curve trend versus the first two metrics. Note that this trend is also dependent on the BS-wall distance. The imaginary part of a wall material's relative permittivity, affected by the material's conductivity, strongly influences the fluctuation magnitude shaking around the curve of the (asymptotic) channel capacity with respect to the real part of a building material's relative permittivity. Generally, a severer fluctuation arises out of a smaller conductivity. Besides, the size and aspect ratio of a room determine the transverse dimension of the wall material, which also influence the capacity level achieved in a room. Given the same room aspect ratio, the wall material of a smaller size are more beneficial to the spatially averaged capacity in the room. Given the same room size, deploying the BS near the long side wall of the room with an aspect ratio close to 2 leads to the largest spatially averaged capacity in the room.

Note that neglecting the impact of multipath components in Paper II will not lead to any different conclusions on the wireless friendliness of building materials from that in Paper I,

because the the capacity of the two-ray channel in Paper II has the same monotonicity with the capacity of the multipath channel in Paper I.

Also note that even though the curves in Fig. 6(b) seem to be close to each other, the differences caused by the permittivities of building materials are non-negligible, because by using the logarithmic scale of the sum of the channel eigenvalues, the impact of the permittivity of a building material on the channel capacity has been understated.

Paper III: Effects of Wall Reflection on the Per-Antenna Power Distribution of ZF-Precoded ULA for Indoor mmWave MU-MIMO Transmissions, Yixin Zhang, Jiliang Zhang, Xiaoli Chu, and Jie Zhang. This paper has been published in IEEE Communications Letters, Volume: 25, Issue: 1, Pages: 13-17, Jan. 2021. Date of Publication: 09 Sep. 2020.

In the third paper, we investigate the effects of WR from building materials on the per-antenna power distribution of a transmit ULA adopting a zero-forcing (ZF) precoder for indoor multi-user (MU) MIMO downlink scenarios. To avoid the possible low efficiency of RF power amplifiers caused by the non-uniform power excitation across the transmit antennas, it would be useful to know how much power is assigned to each individual antenna to serve multiple users simultaneously.

To capture the effects of WR on the per-antenna power distribution across the precoded ULA, a new channel model characterising both the LOS path and the WR path is proposed for indoor MU-MIMO downlink scenarios. The intended symbols for multiple UEs are firstly precoded at the transmit ULA, and then propagate through the proposed channel under flat fading, e.g. in an mmWave orthogonal frequency division multiplexing (OFDM) system [83, 84]. The impact of mutual coupling is considered by incorporating the empirical mutual coupling coefficient for each transmit antenna. The entries of ZF precoding matrix for a dual-UE case are analytically derived and verified through simulations. For the scenario where the BS is deployed close to a wall, we apply two metrics, i.e., the normalised power distribution, and the maximum power ratio (MPR), to evaluate the power distribution across the transmit precoded ULA. The normalised power allocated to a transmit antenna to serve a specific UE is defined by the squared absolute value of the corresponding entry in the precoding matrix normalised by the Frobenius norm of the precoding vector for this UE,

while the MPR for a specific UE is defined as the ratio between the maximum and the minimum of the normalised power allocated to all the antennas for serving this UE. In terms of these two metrics, we study the effects of WR on the per-antenna power distribution across the ZF-precoded ULA through the comparisons between our proposed channel model and the pure LOS channel model under 28 GHz, and also investigate how the per-antenna power distribution over the ZF-precoded ULA changes with the building material's relative permittivity and thickness, the BS-wall distance, the MU spatial distribution, and the mutual coupling level.

Through the numerical results, we gain the following conclusions. It is found that the per-antenna power distribution over the ZF-precoded ULA becomes more uneven under the effects of WR. The power distribution across the ZF-precoded ULA is greatly affected by the relative permittivity of the building material. The power difference as large as 8 dB is observed between the ends of the ULA when the real part of the relative permittivity is 9, while this difference will be gradually reduced to less than 3 dB when the real part of the relative permittivity decreases from 9 to 1. Nonetheless, the power distribution across the ZF-precoded ULA almost does not change with the building material's thickness. As the UE moves farther away from the wall (i.e., the length of the LOS path increases), the normalised power across the transmit antennas varies slower within a smaller dynamic range. The ZF precoder needs to allocate highly different power levels across the ULA to distinguish the two UEs that are very close to each other. The variation in the power distribution across the ZF-precoded ULA first becomes more drastic when the BS-wall distance increases from 0.01 to 0.05 m, and then gradually flattens across the transmit antennas when the BS-wall distance goes beyond 0.05 to 0.09 m. Mutual coupling affects the power distribution slightly when the mutual coupling level is below -10 dB, whereas needs to be considered when this coupling level becomes higher.

3.2 Papers not Included in the Thesis

- **On the Performance of Indoor Multi-Story Small-Cell Networks**, Chen Chen, Yixin Zhang, Jiliang Zhang, Xiaoli Chu and Jie Zhang. This paper has been published on IEEE Transactions on Wireless Communications, 2021.

- **On the Wireless Friendliness Evaluations for Sandwich Building Materials as Reflectors**, Yixin Zhang, Jiliang Zhang, Xiaoli Chu, and Jie Zhang. This paper is under preparation and is planned to be submitted to IEEE Transactions on Wireless Communications.

3.3 Conclusions and Future Works

In this thesis, we have proposed four effective metrics and schemes for evaluating the wireless friendliness of building materials based on the proposed two-ray channel model and multipath channel model that incorporate the LOS and WR paths, and studied the effects of WR from a building material on the per-antenna power distribution across a precoded transmit antenna array. The main conclusion is that, in the building design and planning stage, building materials as reflectors have to be well selected or designed to avoid the risk of reducing indoor wireless capacity and RF power amplifier working efficiency.

Observed from the numerical results, we obtain the following useful insights. The combined value pair of the relative permittivity and thickness of a building material is worthy of careful consideration, which might lead to nearly 13.5% difference in indoor wireless capacity. The relative permittivity of a building material has more significant impact on its wireless friendliness than the material's thickness. Compared with the imaginary part of a building material's relative permittivity, its real part plays a more dominant role in affecting the material's wireless friendliness. The upward and downward trend of (asymptotic) channel capacity versus the real part of a building material's relative permittivity is affected by and sensitive to the BS-wall distance. The imaginary part of a building material's relative permittivity, determined by the material's conductivity, strongly influences the fluctuation

magnitude shaking around the curve of the (asymptotic) channel capacity with respect to the real part of a building material's relative permittivity, in which a smaller conductivity leads to a severer fluctuation. The effects of the WRs from a building material will exacerbate the unevenness of the power distribution across the ZF-precoded ULA as large as 8 dB, which may lead to the potential low working efficiencies of the antennas' corresponding RF power amplifiers. The relative permittivity of the building material can be adjusted to alleviate the unevenness of the per-antenna power distribution, while the thickness of the building material hardly help.

The results yielded in this thesis are inspiring for the following future extensive research directions, including but not limit to:

1) Sandwich building materials: Given that the practical buildings are commonly coated with multi-layer composite materials, it is of great necessity to analyse the wireless friendliness of sandwich building materials. One of the challenges is that the analytical indoor wireless capacity is hard to be characterised by the EM and physical properties of sandwich building materials due to the non closed-form reflection coefficients in (2.54). Moreover, the optimal configuration of sandwich building materials would be formulated into a multivariate optimisation problem, the complexity of which would increase with the number of layers.

2) Shared building materials between rooms: The wall shared by two adjacent rooms would influence the wireless performance in both rooms. The signal leakage to a neighbouring room may cause huge energy waste and unexpected interference. Therefore, the shared building material between rooms should be delicately selected and/or designed to achieve desirable performance in the room that the BS intends to serve and suppress or even eliminate the unwanted interference on its neighbouring room behind the shared wall. This leads to the research on the RF transparency of the shared building materials, which is dependent on its reflection and transmission characteristics.

3) Joint optimisation of building materials and building layouts: In fact, the selections of building materials should take the essential building utilities into account, such as the load-bearing characteristic of a building. Changing the materials of non load-bearing walls for desirable indoor wireless performance is feasible. However, changing the materials of

load-bearing walls may cause safety risks. Hence, the building materials used for different applicability may need to exhibit different wireless friendliness performance. This calls for the joint optimisation of building materials and building layouts.

4) Experimental validations: all the analytical results of the proposed channel models and the evaluation schemes in this thesis are verified by simulation results. It is also critical to validate the above numerical results with experimental results. A comprehensive measurement campaign will be held in future works.

References

[1] W. Saad, M. Bennis and M. Chen, "A vision of 6G wireless systems: applications, trends, technologies, and open research problems," *IEEE Network*, vol. 34, no. 3, pp. 134-142, May/Jun. 2020.

[2] F. Guo, *et al.*, "Enabling massive IoT toward 6G: a comprehensive survey," *IEEE Internet Things J.*, early access, 2021.

[3] Telecom Advisory Services, LLC, "The economic value of Wi-Fi: a global view (2018 and 2023)," Aug. 2018.

[4] Nokia Bell Labs, "Extreme massive MIMO for macro cell capacity boost in 5G-Advanced and 6G", white paper, Oct. 2021. [Online]. Available: https://www.bell-labs.com/institute/white-papers/extreme-massive-mimo-for-macro-cell-capacity-boost-in-5g-advanced-and-6g/

[5] Y. L. Lee, *et al.*, "6G massive radio access networks: key applications, requirements and challenges," *IEEE Open Journal of Vehicular Technology*, vol. 2, pp. 54-66, 2021.

[6] D. Lopez-Perez, *et al.*, "IEEE 802.11be extremely high throughput: the next generation of Wi-Fi technology beyond 802.11ax," *IEEE Commun. Mag.*, vol. 57, no. 9, pp. 113-119, Sept. 2019.

[7] V. Gokhale, *et al.*, "Toward enabling high-five over WiFi: a tactile internet paradigm" *IEEE Commun. Mag.*, vol. 59, no. 12, pp. 90-96, Dec. 2021.

[8] Cisco, “Cisco vision: 5G-thriving indoors,” Feb. 2017. [Online]. Available: cisco.com/c/dam/en/us/solutions/collateral/service-provider/ultra-services-platform/5g-ran-indoor.pdf

[9] Aragón-Zavala, Alejandro. “Indoor wireless communications : from theory to implementation,” *John Wiley & Sons*, Incorporated, 2017.

[10] J. Zhang, *et al.*, “Fundamental wireless performance of a building,” *IEEE Wirel. Commun.*, accepted, 2021.

[11] J. Zhang, A. A. Glazunov and J. Zhang, “Wireless energy efficiency evaluation for buildings under design based on analysis of interference gain,” *IEEE Trans. Veh. Tech.*, vol. 69, no. 6, pp. 6310–6324, Jun. 2020.

[12] J. Zhang, A. A. Glazunov and J. Zhang, “Wireless performance evaluation of building layouts: closed-form computation of figures of merit,” *IEEE Transactions on Communications*, early access, 2021.

[13] W. Wang, *et al.*, “Compact quad-element vertically-polarized high-isolation wideband MIMO antenna for vehicular base station," *IEEE Trans. Veh. Tech.*, vol. 69, no. 9, pp. 10000-10008, Sep. 2020.

[14] S. Yang and L. Hanzo, “Fifty years of MIMO detection: the road to large-scale MIMOs," *IEEE Commun. Surveys Tuts.*, vol. 17, no. 4, pp. 1941–1988, 4th Quart., 2015.

[15] B. Rohani, *et al.*, “Improving channel capacity in indoor 4×4 MIMO base station utilizing small bidirectional antenna," *IEEE Trans. Antennas Propag.*, vol. 66, no. 1, pp. 393-400, Jan. 2018.

[16] G. Li, *et al.*, “AMC-loaded wideband base station antenna for indoor access point in MIMO system," *IEEE Trans. Antennas Propag.*, vol. 63, no. 2, pp. 525-533, Feb. 2015.

[17] Y. Zeng and X. Xu, “Toward environment-aware 6G communications via channel knowledge map,” *IEEE Wirel. Commun.*, early access, 2021.

[18] W. Yang, *et al.*, “Line-of-sight probability for channel modeling in 3-D indoor environments,” *IEEE Antennas Wirel. Propag. Lett.*, vol. 19, no. 7, pp. 1182-1186, Jul. 2020.

[19] C. Chen, *et al.*, “On the performance of indoor multi-story small-cell networks,” *IEEE Trans. Wirel. Commun.*, vol. 20, no. 2, pp. 1336-1348, Feb. 2021.

[20] ITU-R, “Effects of building materials and structures on radiowave propagation above about 100 MHz P series radiowave propagation,” *Recomm. ITU-R P.2040-1*, Jul. 2015.

[21] L. Azpilicueta, *et al.*, “Impact of material changes in electromagnetic dosimetry estimation of complex indoor scenarios,” *European Conference on Antennas and Propagation (EUCAP)*, Prague, 2012, pp. 2048-2050.

[22] K. Haneda, *et al.*, “Indoor 5G 3GPP-like channel models for office and shopping mall environments,” *IEEE International Conference on Communications Workshops (ICC)*, Kuala Lumpur, 2016, pp. 694-699.

[23] S. K. Yoo, *et al.*, “Ceiling- or wall-mounted access points: an experimental evaluation for indoor millimeter wave communications,” *13th European Conference on Antennas and Propagation (EuCAP)*, Krakow, Poland, 2019, pp. 1-5.

[24] X. Zhang, *et al.*, “Analysis of millimeter-wave channel characteristics based on channel measurements in indoor environments at 39 GHz,” *11th International Conference on Wireless Communications and Signal Processing (WCSP)*, 2019, pp. 1-6.

[25] D. R. Morgan and J. Ling, “Simulation and analysis of 2.4 GHz propagation in a medium-size conference room,” *Fortieth Asilomar Conference on Signals, Systems and Computers*, 2006, pp. 433-437.

[26] W. Yang, *et al.*, “Measurements of reflection and penetration loss in indoor environments in the 39-GHz band,” *15th European Conference on Antennas and Propagation (EuCAP)*, 2021, pp. 1-5.

[27] Y. Ai, J. B. Andersen and M. Cheffena, "Path-loss prediction for an industrial indoor environment based on room electromagnetics," *IEEE Trans. on Antennas Propag.*, vol. 65, no. 7, pp. 3664-3674, Jul. 2017.

[28] F. Sagnard and G. E. Zein, "In situ characterization of building materials for propagation modeling: frequency and time responses," *IEEE Trans. Antennas Propag.*, vol. 53, no. 10, pp. 3166-3173, Oct. 2005.

[29] C. Jansen, *et al.*, "The impact of reflections from stratified building materials on the wave propagation in future indoor terahertz communication systems," *IEEE Trans. Antennas Propag.*, vol. 56, no. 5, pp. 1413-1419, May 2008.

[30] G. Narimani, *et al.*, "Analysis of ultrawideband pulse distortion due to lossy dielectric walls and indoor channel models," *IEEE Trans. Antennas Propag.*, vol. 64, no. 10, pp. 4423-4433, Oct. 2016.

[31] Y. Z. Goh, *et al.*, "Effects of complex wall structures on antenna radiation characteristics," *IEEE International Symposium on Antennas and Propagation & USNC/URSI National Radio Science Meeting*, Boston, MA, 2018, pp. 2485-2486.

[32] J. Zhang, *et al.*, "Two-ray reflection resolution algorithm for planar material electromagnetic property measurement at the millimeter-wave bands," *Radio Sci.*, vol. 55, no. 3, Mar. 2020.

[33] Y. Azar, H. Zhao and M. E. Knox, "Polarization diversity measurements at 5.8 GHz for penetration loss and reflectivity of common building materials in an indoor environment," *Third International Conference on Future Generation Communication Technologies (FGCT)*, Luton, 2014.

[34] O. Landron, M. J. Feuerstein, and T. S. Rappaport, "A comparison of theoretical and empirical reflection coefficients for typical exterior wall surfaces in a mobile radio environment," *IEEE Trans. Antennas Propag.*, vol. 44, no. 3, pp. 341-351, Mar. 1996.

[35] N. Yu, P. Genevet, M. A. Kats, F. Aieta, J.-P. Tetienne, F. Capasso, and Z. Gaburro, "Light propagation with phase discontinuities: Generalized laws of reflection and refraction," *Science*, vol. 334, no. 6054, pp. 333-337, Oct. 2011.

[36] P. Skrimponis, *et al.*, "Power consumption analysis for mobile mmWave and sub-THz receivers," *2020 2nd 6G Wireless Summit (6G SUMMIT)*, Levi, Finland, 2020, pp. 1-5.

[37] P. Angeletti and G. Toso, "Array antennas with jointly optimized elements positions and dimensions Part I: linear arrays," *IEEE Trans. Antennas Propag.*, vol. 62, no. 4, pp. 1619-1626, Apr. 2014.

[38] N. Amani, *et al.*, "Per-antenna power distribution of a zero-forcing beamformed ULA in pure LOS MU-MIMO," *IEEE Commun. Lett.*, vol. 22, no. 12, pp. 2515–2518, Dec. 2018.

[39] T. M. Pham, *et al.*, "Efficient zero-forcing precoder design for weighted sum-rate maximization with per-antenna power constraint," *IEEE Trans. Veh. Technol.*, vol. 67, no. 4, pp. 3640–3645, Apr. 2018.

[40] A. Asp, *et al.*, "Impact of different concrete types on radio propagation: fundamentals and practical RF measurements," *4th International Conference on Smart and Sustainable Technologies (SpliTech)*, Split, Croatia, 2019, pp. 1-8.

[41] A. Asp, *et al.*, "Impact of modern construction sandwich building sandwich building materials on radio signal propagation: practical measurements and network planning aspects," *IEEE 79th Vehicular Technology Conference (VTC Spring)*, Seoul, 2014, pp. 1-7.

[42] A. Asp, *et al.*, "Impact of concrete moisture on radio propagation: fundamentals and measurements of concrete samples," *16th International Symposium on Wireless Communication Systems (ISWCS)*, Oulu, Finland, 2019, pp. 542-547.

[43] A. Asp, *et al.*, “Effect of plastering mesh on radio signals: modelling and practical measurements,” *European Conference on Networks and Communications (EuCNC), Dubrovnik*, Croatia, 2020, pp. 68-73.

[44] D. Ferreira, *et al.*, “Assessing transparency control of southern European building wall structures using frequency-selective surfaces [Wireless Corner],” *IEEE Antennas Propag. Mag.*, vol. 60, no. 5, pp. 137-153, Oct. 2018.

[45] K. Sato et al., "Measurements of reflection and transmission characteristics of interior structures of office building in the 60-GHz band," *IEEE Trans. on Anten. and Propag.*, vol. 45, no. 12, pp. 1783-1792, Dec. 1997.

[46] A. Karttunen, *et al.*, “Window and wall penetration loss on-site measurements with three methods,” *12th European Conference on Antennas and Propagation (EuCAP)*, London, 2018, pp. 1-5.

[47] X. Liao, *et al.*, “Experimental study of diffuse scattering from typical construction materials over 40-50GHz,” *IEEE Asia-Pacific Conference on Antennas and Propagation (APCAP)*, Auckland, 2018, pp. 216-218.

[48] Y. Shao, X. Liao and Y. Wang, “Complex permittivity of typical construction materials over 40–50 GHz,” *IEEE International Symposium on Antennas and Propagation & USNC/URSI National Radio Science Meeting*, Boston, MA, 2018, pp. 2003-2004.

[49] A. Asp, *et al.*, “Radio signal propagation and attenuation measurements for modern residential buildings,” *IEEE Globecom Workshops*, Anaheim, CA, 2012, pp. 580-584.

[50] S. Gerges, P. Gkorogias, “Concrete sandwich element design in terms of passive housing recommendations and moisture safety,” Master Thesis in Building Technology, KTH Architecture and the Built Environment.

[51] K. A. Al-Sallal, “Comparison between polystyrene and fiberglass roof insulation in warm and cold climates,” *Renewable Energy*, vol. 28, no. 4, pp. 603-611, Apr. 2003.

[52] D. Illera, *et al.*, “Cellulose aerogels for thermal insulation in buildings: trends and challenges,” *Coatings*, vol. 8, no. 10, pp. 345, Sep. 2018.

[53] X. Liang, *et al.*, “Investigations on the basic electrical properties of Polyurethane foam material," *IEEE 11th International Conference on the Properties and Applications of Dielectric sandwich building sandwich building materials (ICPADM)*, Sydney, NSW, Australia, 2015, pp. 863-866.

[54] C. Eyraud, *et al.*, “Complex permittivity determination from far-field scattering patterns,” *IEEE Antennas Wirel. Propag. Lett.*, vol. 14, pp. 309-312, 2015.

[55] S. J. Orfanidis, *Electromagnetic Waves and Antennas*, online book, 2004-2010. Available: https://www.ece.rutgers.edu/ orfanidi/ewa/

[56] Rajeev Bansal, Fundamentals of Engineering Electromagnetics, 1st Edition. CRC Press. https://doi.org/10.1201/9781315221830

[57] Raymond Kwok, Lossy Medium. [Online]. Available: https://www.sjsu.edu/people/raymond.kwok/docs/ee140/Lossy_Medium.pdf.

[58] S .M. Bida, *et al.*, “Advances in precast concrete sandwich panels toward energy efficient structural buildings,” *Preprints Posted*, Oct. 2018, doi:10.20944/preprints201810.0147.v1

[59] M. Inomata, *et al.*, “Diffuse scattering prediction for 26GHz band in indoor office environments,” *International Symposium on Antennas and Propagation (ISAP)*, Phuket, 2017, pp. 1-2.

[60] H. Tian, *et al.*, “Diffuse scattering characteristics of rough materials at mm-Wave frequencies,” *IEEE International Symposium on Antennas and Propagation and USNC-URSI Radio Science Meeting*, Atlanta, GA, USA, 2019, pp. 377-378.

[61] C. R. Anderson and T. S. Rappaport, “In-building wideband partition loss measurements at 2.5 and 60 GHz," *IEEE Trans. Wireless Commun.*, vol. 3, no. 3, pp. 922-928, May 2004.

[62] J. Lee, *et al.*, "Permittivity effect of building materials on 28 GHz mmWave channel using 3D ray tracing simulation," *2017 IEEE Global Communications Conference, 2017*, pp. 1-6.

[63] Sung-Sil Cho, *et al.*, "Prediction of electromagnetic transmission properties using dielectric property modeling of foamed concrete containing BFS", *Construction and Building Materials*, vol. 151, pp. 650-660, 2017.

[64] D. Ferreira, I. Cuiñas, R. F. S. Caldeirinha and T. R. Fernandes, "A review on the electromagnetic characterisation of building materials at micro- and millimetre wave frequencies," *The 8th European Conference on Antennas and Propagation (EuCAP)*, 2014, pp. 145-149, doi: 10.1109/EuCAP.2014.6901713.

[65] S. S. Zhekov, O. Franek and G. F. Pedersen, "Dielectric properties of common building materials for ultrawideband propagation studies [Measurements corner]," *IEEE Antenn. and Propag. Mag.*, vol. 62, no. 1, pp. 72-81, Feb. 2020.

[66] N. Makul, "Dielectric permittivity of various cement-based building materials during the first 24 hours hydration," *Open Journal of Inorganic Non-metallic materials*, vol. 3, no. 4, pp. 53-57, Aug. 2013.

[67] H. Zhao, *et al.*, "28 GHz millimeter wave cellular communication measurements for reflection and penetration loss in and around buildings in New York city", *Proc. IEEE Int. Conf. Commun. (ICC)*, 2013, pp. 5163-5167.

[68] D. Pena, *et al.*, "Measurement and modeling of propagation losses in brick and concrete walls for the 900-MHz band," *IEEE Trans. Antennas Propag.*, vol. 51, no. 1, pp. 31-39, Jan. 2003.

[69] B. Feitor, *et al.*, "Estimation of dielectric concrete properties from power measurements at 18.7 and 60 GHz," *Loughborough Antennas & Propagation Conference*, Loughborough, 2011, pp. 1-5.

[70] J. Ahmadi-Shokouh, *et al.*, “Reflection Coefficient Measurement for House Flooring Materials at 57-64 GHz," *IEEE Global Telecommunications Conference*, 2009, pp. 1-6.

[71] X. Gao, *et al.*, “Massive MIMO performance evaluation based on measured propagation data,” *IEEE Trans. Wirel. Commun.*, vol. 14, no. 7, pp. 3899–3911, Jul. 2015.

[72] Constantine A. Balanis. *Antenna Theory: Analysis and Design, Fourth Edition*. Fourth Edition. John Wiley & Sons, Inc, 2016.

[73] A. F. Molisch, *Wireless Communications*, John Wiley & Sons, 2012.

[74] S. Y. Seidel and T. S. Rappaport, “Site-specific propagation prediction for wireless in-building personal communication system design,” *IEEE Transactions on Vehicular Technology*, vol. 43, no. 4, pp. 879–891, Nov. 1994.

[75] R. Valenzuela, “A ray tracing approach to predicting indoor wireless transmission,” *IEEE 43rd Vehicular Technology Conference*, May 1993, pp. 214–218.

[76] A. Goldsmith, *Wireless Communications*, Cambridge University Press, 2005.

[77] E. Zöchmann, K. Guan and M. Rupp, “Two-ray models in mmWave communications,” *IEEE 18th International Workshop on Signal Processing Advances in Wireless Communications (SPAWC)*, Sapporo, 2017, pp. 1-5.

[78] G. D. Durgin, T. S. Rappaport and D. A. de Wolf, “New analytical models and probability density functions for fading in wireless communications,” *IEEE Transactions on Communications*, vol. 50, no. 6, pp. 1005-1015, Jun. 2002.

[79] D. Tse, and P. Viswanath, *Fundamentals of Wireless Communication*, Cambridge University Press, 2004.

[80] T. K. Sarkar, *et al.*, “A survey of various propagation models for mobile communication,” *IEEE Antennas and Propagation Magazine*, vol. 45, no. 3, pp. 51-82, Jun. 2003.

[81] M. B. Zetterberg, *et al.*, “IST-2003-507581 WINNER D5.4 v1.4 final report on link level and system level channel models,” Nov. 2005.

[82] Chen-Nee Chuah, *et al.*, “Capacity scaling in MIMO wireless systems under correlated fading,” *IEEE Trans. Inform. Theory*, vol. 48, no. 3, pp. 637-650, March 2002.

[83] R. W. Heath, *et al.*, “An overview of signal processing techniques for millimeter wave MIMO systems,” *IEEE J. Sel. Top. Sign. Proces.*, vol. 10, no. 3, pp. 436-453, Apr. 2016.

[84] G. Wang, P. Karanjekar and G. Ascheid, “Beamforming with time-delay compensation for 60 GHz MIMO frequency-selective channels," *IEEE 26th Annual International Symposium on Personal, Indoor, and Mobile Radio Communications (PIMRC)*, 2015, pp. 387-391.

Part II

Papers

Paper I

How Friendly are Building Materials as Reflectors to Indoor LOS MIMO Communications?

Yixin Zhang, Chen Chen, Songjiang Yang, Jiliang Zhang, Xiaoli Chu, and Jie Zhang.

Published in *IEEE Internet of Things Journal, Volume: 7, Issue: 9, Pages: 9116-9127, Sept. 2020.* Date of Publication: 29 Jun. 2020.

How Friendly are Building Materials as Reflectors to Indoor LOS MIMO Communications?

Yixin Zhang[1], Chen Chen[1], Songjiang Yang[1], Jiliang Zhang[1], Xiaoli Chu[1], Jie Zhang[1,2]

[1] Department of Electronic and Electrical Engineering, the University of Sheffield, Sheffield, S10 2TN, UK

[2] Research and Development Department, Ranplan Wireless Network Design Ltd., Cambridge, CB23 3UY, UK

Abstract

The tremendous popularity of internet of things (IoT) applications and wireless devices have prompted a massive increase of indoor wireless traffic. To further explore the potential of indoor IoT wireless networks, creating constructive interactions between indoor wireless transmissions and the built environments becomes necessary. The electromagnetic (EM) wave propagation indoors would be affected by the EM and physical properties of the building material, e.g., its relative permittivity and thickness. In this paper, we construct a new multipath channel model by characterising wall reflection (WR) for an indoor line-of-sight (LOS) single-user multiple-input multiple-output (MIMO) system and derive its ergodic capacity in closed-form. Based on the analytical results, we define the wireless friendliness of a building material based on the spatially averaged indoor capacity and propose a scheme for evaluating the wireless friendliness of building materials. Monte Carlo simulations validate our analytical results and manifest the significant impact of the relative permittivity and thickness of a building material on indoor capacity, indicating that the wireless friendliness of building materials should be considered in the planning and optimisation of indoor wireless networks. The outcomes of this paper would enable appropriate selection of wall materials during building design, thus enhancing the capacity of indoor LOS MIMO communications.

1 Introduction

Internet of things (IoT) connects numerous heterogeneous devices, and provides infrastructures for smart buildings [1, 2], smart grids [3], and smart cities [4]. With the roll-out of 5G systems and the opening horizon of 6G systems, cellular networks will provide economical, flexible and reliable wireless connectivities for IoT devices, e.g., by leveraging 5G massive machine type communication (mMTC) [5] and 6G massive broad bandwidth machine type (mBBMT) [6] technologies.

It is predicted that 80-96% of wireless data traffic will be consumed indoors in the future [7]. As a result, indoor wireless traffic required by IoT is growing at an unprecedented rate. Notably, physical obstacles like walls would affect the indoor propagation of electromagnetic (EM) waves. Therefore, indoor wireless performance should be one of the indispensable prerequisites when designing buildings [8, 9].

To meet the high data demand and address the capacity crunch in-building, indoor small base stations (BSs) are usually equipped with large-scale antenna arrays [10], e.g. consisting of hundreds of antennas, facilitated by multiple-input multiple-output (MIMO) technology to achieve spatial multiplexing/diversity gains [11–13]. In order to guarantee a low spatial correlation, the space intervals among antenna elements of the MIMO antenna array have to be larger than half wavelength [14], which therefore will increase the physical dimension of the indoor small BSs and generate negative weight and visual consequence on a room. Especially in industrial environment, deploying BSs in the workspace may increase the risk of accidents.

To avoid any possible negative impact on the functionality and appearance of a room, a desirable indoor BS deployment is to integrate MIMO antenna arrays with interior walls[10, 16], which however will result in non-negligible coupling between MIMO antenna arrays and building materials [17–19]. Specifically, when an EM wave impinges on a wall surface, the intensity of the wall reflected wave can be measured by the reflection coefficient, which depends on the EM and physical properties of the wall material, i.e., its relative permittivity and thickness [20–25]. The wall reflected EM waves would be superposed with other EM waves, which may jointly influence the indoor wireless performance. Hence, enhancing

indoor wireless performance requires a rational selection and/or design of building materials. In this paper, we define the wireless friendliness as a new performance metric of a building material, which is characterised by its relative permittivity and thickness. A building material with desirable wireless friendliness would be beneficial to the performance of indoor wireless networks.

Metamaterials are known as novel artificial structures, which can be customized to build a programmable EM propagation environment [26]. The meta-atoms in metamaterials are software-controlled to firstly capture the signals from the source and then reflect the signal to the destination actively or passively [27, 28]. Although metamaterials are expected to contribute to indoor capacity improvement, they are facing major challenges such as their design complexity growing exponentially with the number of meta-atoms. Besides, the energy efficiency of metamaterial-aided wireless networking is no better than massive MIMO [29] and relay-supported transmissions [30].

By contrast, the wireless friendliness of concrete as a widely used building material has not been sufficiently studied. Most of the existing works on the EM wave propagation loss through concrete walls were based on measurements [21, 31, 32]. As far as we know, a theoretical analysis of indoor multipath capacity influenced by the EM and physical properties of concrete is still missing. As will be shown in the subsequent sections, the appropriate selection of building materials will increase the baseline value of indoor capacity. Accordingly, the wireless performance of building materials should be considered inherently in the design of future smart/green buildings. Hence, it is of vital importance to build an evaluation scheme to identify the relationship between the wireless friendliness of a building material and its EM and physical properties [34].

In this paper, we study the impact of building materials, especially their relative permittivity and thickness, on the performance of indoor line-of-sight (LOS) MIMO communications. To the best of our knowledge, this is the first attempt to study the indoor capacity from the perspective of wall material design.

The main contributions of this paper are summarized as follows:

- Taking the wall reflection (WR) path into account and based on distance-dependant Rician fading model, a new indoor LOS MIMO channel model is proposed.
- The marginal probability distribution function (MPDF) of an unordered squared singular value, the ergodic capacity of the indoor LOS MIMO channel, and the squared singular values of its deterministic part are analytically obtained in closed forms. These analytical expressions reveal the relationship between the indoor MIMO channel capacity and the relative permittivity and thickness of the building material.
- We propose a scheme based on spatially averaged indoor capacity, which can be used to evaluate the wireless friendliness of building materials and to guide the design of a wireless-friendly building.
- The wireless friendliness performance of building materials is analysed. The optimal values of the permittivity and thickness of building materials that maximise the spatially averaged indoor capacity are obtained for both the omnidirectional and directional BS antenna arrays.
- The analytical results are verified through Monte Carlo simulations.

The remainder of this paper is organized as follows. Section II introduces system model for indoor LOS MIMO downlink transmissions. In Section III, the analytical MPDF of an unordered squared singular value, the ergodic capacity of an indoor LOS MIMO channel, and the squared singular values of its deterministic part are derived in closed forms. Then a scheme used for evaluating the wireless friendliness of a building material is proposed in Section IV. The impact of directional radiation pattern is discussed in Section V. Monte Carlo simulation results are provided to verify all analytical results in Section VI. Finally, Section VII concludes this paper.

2 System Model

In this section, we introduce a novel system model for indoor LOS MIMO communications that incorporates the WR path and the EM and physical properties of the building material.

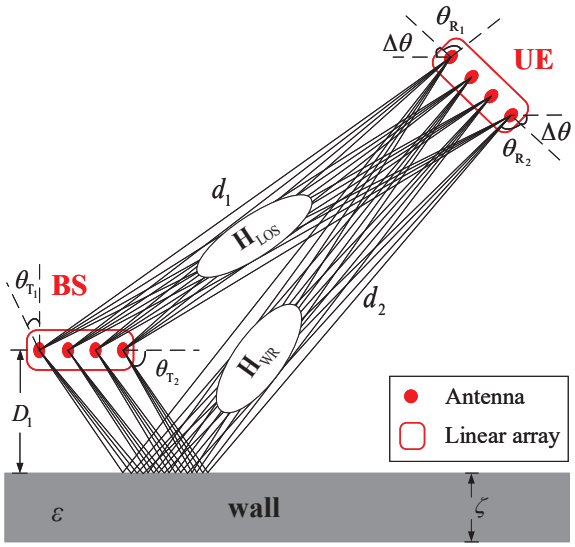

Fig. 1. The LOS path and the WR path between indoor BS and UE.

We consider indoor LOS MIMO downlink transmissions, as shown in Fig. 1. In the considered room, one BS is deployed close to one of the walls and one user equipment (UE) could be arbitrarily positioned. Since the strength of a WR path from a wall other than the wall that is closest to the BS will be dominated by the distance-dependent path loss, the reflected paths from the other walls would be much weaker than the WR path from the wall closest to the BS. Hence, the considered wall refers to the wall closest to the BS hereafter, and the WR path refers to the wall reflected path from the considered wall. The BS is deployed in parallel with the considered wall with a small distance of D_1 from the wall. The BS and a typical UE are equipped with N_{T} and N_{R} omnidirectional antennas, respectively, both in linear arrays with inter-antenna spacing D. The complex frequency-flat linear channel from the BS to the typical UE is constructed as

$$\mathbf{y} = \mathbf{H}\mathbf{x} + \mathbf{n}, \tag{1}$$

where $\mathbf{x} \in \mathbb{C}^{N_\mathrm{T}\times 1}$, $\mathbf{y} \in \mathbb{C}^{N_\mathrm{R}\times 1}$ denote the transmitted signal and the received signal, respectively, $\mathbf{n}$ denotes the additive white Gaussian noise, and $\mathbf{H}$ is a $N_\mathrm{R} \times N_\mathrm{T}$ channel matrix, subject to $\mathbb{E}[\mathrm{Tr}\{\mathbf{H}\mathbf{H}^\dagger\}] = N_\mathrm{R}N_\mathrm{T}$, where $\mathbb{E}(\cdot)$ and $\mathrm{Tr}\{\cdot\}$ denote the expectation and the trace of a matrix, respectively.

Other than the LOS path, the WR path is taken into account to capture the impact of building materials on the indoor wireless propagation channel. For a certain position in the room, the LOS path and the WR path are deterministically modelled by Friis' formula as $N_\mathrm{R} \times N_\mathrm{T}$ matrix $\mathbf{H}_\mathrm{LOS}$ and $\mathbf{H}_\mathrm{WR}$, respectively, whose elements are given in (2) and (3), respectively,

$$[\mathbf{H}_\mathrm{LOS}]_{n_\mathrm{R},n_\mathrm{T}} = \frac{\mu}{4\pi d_1} e^{-j2\pi\frac{d_1}{\mu} - j2\pi\frac{D}{\mu}\left(\left(n_\mathrm{R}-\frac{N_\mathrm{R}-1}{2}\right)\cos\left(\theta_{\mathrm{R}_1}+\Delta\theta\right)+\left(n_\mathrm{T}-\frac{N_\mathrm{T}-1}{2}\right)\cos\theta_{\mathrm{T}_1}\right)} \tag{2}$$

$$[\mathbf{H}_\mathrm{WR}]_{n_\mathrm{R},n_\mathrm{T}} = \frac{\mu\Gamma}{4\pi d_2} e^{-j2\pi\frac{d_2}{\mu} - j2\pi\frac{D}{\mu}\left(\left(n_\mathrm{R}-\frac{N_\mathrm{R}-1}{2}\right)\cos\left(\theta_{\mathrm{R}_2}+\Delta\theta\right)+\left(n_\mathrm{T}-\frac{N_\mathrm{T}-1}{2}\right)\cos\theta_{\mathrm{T}_2}\right)} \tag{3}$$

in which $n_\mathrm{T} \in \{0,1,...,N_\mathrm{T}-1\}$ and $n_\mathrm{R} \in \{0,1,...,N_\mathrm{R}-1\}$ are the indices of transmit and receive antenna elements, μ denotes the wavelength of EM waves in the air, d_1 and d_2 denote the length of the LOS path and the WR path, respectively, θ_{T_1} and θ_{T_2} denote the approximated angle of departure (AoD) of the LOS path and the WR path at the BS array, respectively, while θ_{R_1} and θ_{R_2} denote the approximated angle of arrival (AoA) of the LOS path and the WR path at the UE array, respectively, $\Delta\theta$ denotes the arbitrary orientation angle of the UE array, where $\theta_{\mathrm{T}_1}, \theta_{\mathrm{T}_2}, \theta_{\mathrm{R}_1}, \theta_{\mathrm{R}_2}, \Delta\theta \in \{0,\pi\}$, $(\theta_{\mathrm{R}_1}+\Delta\theta)$ and $(\theta_{\mathrm{R}_2}+\Delta\theta)$ denote equivalent AoA of the LOS path and the WR path at the UE array, respectively, and Γ represents the equivalent reflection coefficient of the WR path.

Along the WR path, multiple internal reflections are considered when the EM wave interacts with the building material. Using plane wave far-field approximation, the incident angles of different order reflections are all approximated by α. When the building material is assumed to be a homogenous dielectric reflector with relative permittivity ε and thickness ζ, the equivalent reflection coefficient of the WR path is represented as [20]

$$\Gamma = \frac{1-\exp(-j2\delta)}{1-\Gamma'^{2}\exp(-j2\delta)}\Gamma', \tag{4}$$

where

$$\delta = \frac{2\pi\zeta}{\mu}\sqrt{\varepsilon-\sin^2\alpha}, \tag{5}$$

and the first-order reflection coefficient Γ' represents the transverse electric (TE) polarisation Γ_{TE} or the transverse magnetic (TM) polarisation Γ_{TM} of the incident electric field, respectively, which are given by:

$$\Gamma_{\mathrm{TE}} = \frac{\cos\alpha-\sqrt{\varepsilon-\sin^2\alpha}}{\cos\alpha+\sqrt{\varepsilon-\sin^2\alpha}}, \tag{6}$$

or

$$\Gamma_{\mathrm{TM}} = \frac{\cos\alpha-\sqrt{(\varepsilon-\sin^2\alpha)/\varepsilon^2}}{\cos\alpha+\sqrt{(\varepsilon-\sin^2\alpha)/\varepsilon^2}}. \tag{7}$$

For simplicity, $\mathbf{H}_{\mathrm{LOS}}$ and $\mathbf{H}_{\mathrm{WR}}$ are merged as one matrix $\mathbf{H_1}$, which can be decomposed as

$$\mathbf{H_1} = A_1\mathbf{h}_{\beta_1}^{\mathrm{H}}\mathbf{h}_{\alpha_1} + A_2\mathbf{h}_{\beta_2}^{\mathrm{H}}\mathbf{h}_{\alpha_2}, \tag{8}$$

$$A_1 = \frac{\mu\sqrt{N_{\mathrm{T}}N_{\mathrm{R}}}}{4\pi d_1}e^{-j2\pi\frac{d_1}{\mu}},$$

$$A_2 = \frac{\mu\Gamma\sqrt{N_{\mathrm{T}}N_{\mathrm{R}}}}{4\pi d_2}e^{-j2\pi\frac{d_2}{\mu}},$$

$$\alpha_l = 2\pi D\cos\theta_{\mathrm{T}_l}/\mu,$$

$$\beta_l = 2\pi D\cos\left(\theta_{\mathrm{R}_l}+\Delta\theta\right)/\mu,$$

$$\mathbf{h}_{\alpha_l} = \left(\frac{e^{-j\left(-\frac{N_{\mathrm{T}}-1}{2}\right)\alpha_l}}{\sqrt{N_{\mathrm{T}}}}, \frac{e^{-j\left(1-\frac{N_{\mathrm{T}}-1}{2}\right)\alpha_l}}{\sqrt{N_{\mathrm{T}}}}, \ldots, \frac{e^{-j\left(\frac{N_{\mathrm{T}}-1}{2}\right)\alpha_l}}{\sqrt{N_{\mathrm{T}}}}\right),$$

$$\mathbf{h}_{\beta_l} = \left(\frac{e^{j\left(-\frac{N_{\mathrm{R}}-1}{2}\right)\beta_l}}{\sqrt{N_{\mathrm{R}}}}, \frac{e^{j\left(1-\frac{N_{\mathrm{R}}-1}{2}\right)\beta_l}}{\sqrt{N_{\mathrm{R}}}}, \ldots, \frac{e^{j\left(\frac{N_{\mathrm{R}}-1}{2}\right)\beta_l}}{\sqrt{N_{\mathrm{R}}}}\right),$$

where $l \in \{1,2\}$.

Based on distance-dependant Rician fading model and the multipath (MP) effect, our channel matrix $\mathbf{H}$ consists of three components including the LOS part, the WR part, and the MP part, which can be presented as

$$\mathbf{H} = \sqrt{\frac{\bar{K}}{1+\bar{K}}}\bar{\mathbf{H}} + \sqrt{\frac{1}{1+\bar{K}}}\mathbf{H}_{\mathrm{MP}}, \tag{9}$$

where the deterministic matrix $\bar{\mathbf{H}}$, including the LOS part and the WR part, is expressed as

$$\bar{\mathbf{H}} = \frac{\mathbf{H_1}}{\|\mathbf{H_1}\|}\sqrt{N_{\mathrm{R}}N_{\mathrm{T}}}, \tag{10}$$

subject to $\mathbb{E}[\mathrm{Tr}\{\mathbf{H}\mathbf{H}^{\dagger}\}] = N_{\mathrm{R}}N_{\mathrm{T}}$, with $\|\cdot\|$ denoting the F-norm. The MP components are assumed to be independent and identically distributed zero mean and unit variance complex Gaussian random variables arranged in the $N_{\mathrm{R}} \times N_{\mathrm{T}}$ matrix $\mathbf{H}_{\mathrm{MP}}$. $\bar{K}$ is the power ratio between the deterministic part $\bar{\mathbf{H}}$ and the random part $\mathbf{H}_{\mathrm{MP}}$, which can be obtained through

$$\bar{K} = KS, \tag{11}$$

where K is the distance-dependant Rician factor as a function of d_1 defining the power ratio between the LOS part and the MP part, given by [33, Eq. (5.22)]

$$K = 8.7 + 0.051d_1(\mathrm{dB}), \tag{12}$$

and

$$S = \frac{\|\mathbf{H}_1\|^2}{\left\|A_1\mathbf{h}_{\beta_1}^{\mathrm{H}}\mathbf{h}_{\alpha_1}\right\|^2} = \frac{d_1^2}{d_2^2}|\Gamma|^2 + \frac{2Md_1}{N_{\mathrm{T}}N_{\mathrm{R}}d_2} + 1 \tag{13}$$

in which $M = \mathrm{Re}\left(\Gamma e^{-j2\pi\frac{d_2-d_1}{\mu}}\right)\frac{\sin\left(\frac{N_{\mathrm{T}}}{2}(\alpha_2-\alpha_1)\right)}{\sin\left(\frac{1}{2}(\alpha_2-\alpha_1)\right)}\frac{\sin\left(\frac{N_{\mathrm{R}}}{2}(\beta_2-\beta_1)\right)}{\sin\left(\frac{1}{2}(\beta_2-\beta_1)\right)}$, and $\mathrm{Re}(\cdot)$ denotes the real part of a complex value.

3 Analysis of Ergodic Capacity

In this section, for an arbitrary position in the room, we derive the two non-zero squared singular values of $\mathbf{H_1}$, the MPDF of an unordered squared singular value and the ergodic capacity of an indoor LOS MIMO channel $\mathbf{H}$ in closed forms.

3.1 The distribution of the squared singular value of channel

For notational convenience, we define $m = \min\{N_{\mathrm{R}}, N_{\mathrm{T}}\}$ and $n = \max\{N_{\mathrm{R}}, N_{\mathrm{T}}\}$.

Lemma 1: Suppose $\varphi_1, \varphi_2, ..., \varphi_m$ are the m squared singular values of $\mathbf{H_1}$, where $\varphi_1, \varphi_2, ..., \varphi_{m-2} = 0$ and $\varphi_{m-1}, \varphi_m > 0$. The two non-zero squared singular values of $\mathbf{H_1}$ are computed in closed-form as

$$\varphi_{m-1} = \frac{\|\mathbf{X}\|^2 - \sqrt{\|\mathbf{X}\|^4 - 4|\det(\mathbf{X})|^2}}{2}, \tag{14}$$

$$\varphi_m = \frac{\|\mathbf{X}\|^2 + \sqrt{\|\mathbf{X}\|^4 - 4|\det(\mathbf{X})|^2}}{2}, \tag{15}$$

$$\mathbf{X} = \begin{bmatrix} A_1 + A_2\Delta\beta\Delta\alpha & A_2\Delta\beta\,\|\mathbf{h}_{\alpha_*}\| \\ A_2\Delta\alpha\,\left\|\mathbf{h}_{\beta_*}\right\| & A_2\,\|\mathbf{h}_{\alpha_*}\|\,\left\|\mathbf{h}_{\beta_*}\right\| \end{bmatrix},$$

$$\mathbf{h}_{\beta_*}^{\mathrm{H}} = \mathbf{h}_{\beta_2}^{\mathrm{H}} - \Delta\beta\mathbf{h}_{\beta_1}^{\mathrm{H}},$$

$$\mathbf{h}_{\alpha_*} = \mathbf{h}_{\alpha_2} - \Delta\alpha\mathbf{h}_{\alpha_1},$$

and $\Delta\beta$ and $\Delta\alpha$ are given in (16) and (17), respectively [35]

$$\begin{aligned}\Delta\beta = \left\langle \mathbf{h}_{\beta_2}^{\mathrm{H}}, \mathbf{h}_{\beta_1}^{\mathrm{H}} \right\rangle &= \frac{1}{N_{\mathrm{R}}} \sum_{q=-(N_{\mathrm{R}}-1)/2}^{(N_{\mathrm{R}}-1)/2} \exp\left(jq(\beta_1-\beta_2)\right) \\ &= \frac{\sin\left(\pi N_{\mathrm{R}} D\left(\cos\left(\theta_{\mathrm{R}_1}+\Delta\theta\right)-\cos\left(\theta_{\mathrm{R}_2}+\Delta\theta\right)\right)/\mu\right)}{N_{\mathrm{R}}\sin\left(\pi D\left(\cos\left(\theta_{\mathrm{R}_1}+\Delta\theta\right)-\cos\left(\theta_{\mathrm{R}_2}+\Delta\theta\right)\right)/\mu\right)}\end{aligned} \tag{16}$$

$$\begin{aligned}\Delta\alpha = \langle \mathbf{h}_{\alpha_2}, \mathbf{h}_{\alpha_1} \rangle &= \frac{1}{N_{\mathrm{T}}} \sum_{q=-(N_{\mathrm{T}}-1)/2}^{(N_{\mathrm{T}}-1)/2} \exp\left(jq(\alpha_1-\alpha_2)\right) \\ &= \frac{\sin\left(\pi N_{\mathrm{T}} D(\cos\theta_{\mathrm{T}_1}-\cos\theta_{\mathrm{T}_2})/\mu\right)}{N_{\mathrm{T}}\sin\left(\pi D(\cos\theta_{\mathrm{T}_1}-\cos\theta_{\mathrm{T}_2})/\mu\right)}\end{aligned} \tag{17}$$

Proof. See Appendix. □

Theorem 1: The MPDF of an unordered squared singular value λ of $\mathbf{H}$ is computed in (18) [36], where the two non-zero squared singular values of $\sqrt{\bar{K}}\bar{\mathbf{H}}$ are given by

$$\phi_{m-1} = \frac{\bar{K}N_{\mathrm{R}}N_{\mathrm{T}}\varphi_{m-1}}{\|\mathbf{H_1}\|^2} = \frac{KN_{\mathrm{R}}N_{\mathrm{T}}\varphi_{m-1}}{\|A_1\|^2}, \tag{19}$$

and

$$\phi_m = \frac{\bar{K}N_{\mathrm{R}}N_{\mathrm{T}}\varphi_m}{\|\mathbf{H_1}\|^2} = \frac{KN_{\mathrm{R}}N_{\mathrm{T}}\varphi_m}{\|A_1\|^2}, \tag{20}$$

and $D_{i,j}$ is the (i,j)-co-factor of the $m \times m$ matrix $\mathbf{Z}$ whose (l,k)th entry is given by

$$(\mathbf{Z})_{l,k} = \begin{cases} (n-m+k+l-2)!, & 1 \le l \le m-2, \\ \frac{{}_1F_1(n-m+l,n-m+1,\phi_k)}{((n-m+l-1)!)^{-1}}, & \text{otherwise.} \end{cases} \tag{21}$$

The hypergeometric function ${}_0F_1\left(w,z^2\right)$ in (18) is defined in the series form by

$${}_0F_1\left(w,z^2\right) = \sum_{s=0}^{\infty} \frac{(z)^{2s}}{s![w]_s}, \tag{22}$$

and the hypergeometric function ${}_1F_1\left(e,o,g\right)$ in (21) is given by

$${}_1F_1\left(e,o,g\right) = \sum_{s=0}^{\infty} \frac{[e]_s g^s}{[o]_s s!}, \tag{23}$$

where $[r]_t = \frac{(r+t-1)!}{(r-1)!}$.

Proof. Given the channel model in (8)-(13), the channel matrix $\mathbf{H}$ is an N_{R}-by-N_{T} non-central Wishart matrix with mean $\sqrt{\frac{\bar{K}}{1+\bar{K}}}\bar{\mathbf{H}}$. Hence, the MPDF of an arbitrary squared value of $\mathbf{H}$ can be found in [36, (3)], which is derived by the squared singular values of $\sqrt{\bar{K}}\bar{\mathbf{H}}$.

Since $\mathbf{H_1}$ has only two non-zero squared singular values given in Lemma 1 and the relationship between $\mathbf{H_1}$ and $\bar{\mathbf{H}}$ is given in (10), the two non-zero squared singular values of $\sqrt{\bar{K}}\bar{\mathbf{H}}$ are given in (19) and (20), respectively, based on (14) and (15).

Meanwhile, using [36, Lemma 2], we get

$$\begin{aligned}&\lim_{\tau\to\mathbf{0}}\frac{{}_0F_1(n-m+1,(\bar{K}+1)(\phi_i+\tau_i)\lambda)C_{i,j}(\phi_i+\tau_i)}{\prod_{k<l}^{m}((\phi_l+\tau_l)-(\phi_k+\tau_k))}\\&=\frac{f_i(\lambda)D_{i,j}(\phi_i+\tau_i)}{\prod_{l=1}^{m-2}(l-1)!\prod_{l=m-1}^{m}\phi_l^{m-2}(\phi_m-\phi_{m-1})},\end{aligned}\tag{24}$$

where $\tau=\{\tau_1,\tau_2,...,\tau_m\}$ is an m-dimensional vector whose elements are distinct,

$$f_i(\lambda)=\begin{cases}\lambda^{i-1}[n-m+1]_{i-1}^{-1}, & 1\le i\le m-2,\\ {}_0F_1\left(n-m+1,(\bar{K}+1)\phi_i\lambda\right), & \text{otherwise},\end{cases}\tag{25}$$

$D_{i,j}$ is given in (21) and $C_{i,j}$ in [36, (3)] is the (i,j)-co-factor of the $m\times m$ matrix $\mathbf{A}$ whose (i,j)th entry is $\mathbf{A}_{i,j}=(n-m+j-1)!{}_0F_1\left(n-m+j,n-m+1,\phi_i\right)$. Since the $\mathbf{H}$ has only two non-zero squared values, its MPDF can be derived as (18) by substituting (24) and (25) into [36, (3)]. □

3.2 Closed-form ergodic capacity

Theorem 2: The ergodic capacity at a typical position is given by (26), where the average signal-to-noise-ratio (SNR) at each receiver branch is given by

$$\rho=\frac{(\bar{K}+1)\left\|\mathbf{H}_1\right\|^2\rho_{\mathrm{T}}}{\bar{K}N_{\mathrm{R}}N_{\mathrm{T}}},\tag{27}$$

in which $\rho_{\mathrm{T}}=\mathbb{E}\left(\|\mathbf{x}\|^2\right)\Big/\mathbb{E}\left(\|\mathbf{n}\|^2\right)$ refers to the SNR at transmitter side,

$$\kappa=\frac{\exp\left(\frac{\bar{K}+1}{\mathrm{SNR}/N_{\mathrm{T}}}-\phi_m-\phi_{m-1}\right)}{\ln 2\left((n-m)!\right)^{m-1}\left(\phi_m\phi_{m-1}\right)^{m-2}\left(\phi_m-\phi_{m-1}\right)\prod_{l=0}^{m-3}l!},\tag{28}$$

$\vartheta = n-m+j+i-1$, $\tau = n-m+j+p$, and $E_Q(x) = \int_1^\infty e^{-xt}t^{-Q}\,\mathrm{d}t$.

Proof. The ergodic capacity can be derived by taking the expectation with respect to λ as follows [37]

$$\begin{aligned} C(\rho) &= m\mathbb{E}\left[\log_2\left(1+\frac{\rho}{N_\mathrm{T}}\lambda\right)\right] \\ &= m\int_0^\infty \log_2\left(1+\frac{\rho}{N_\mathrm{T}}\lambda\right) f(\lambda)\mathrm{d}\lambda, \end{aligned} \tag{29}$$

where $f(\lambda)$ is given in (18). The integral over λ in (29) is computed by the series expansion of ${}_0F_1\left(n-m+1,(\bar{K}+1)\,\phi_i\lambda\right)$ in (22) and

$$\int_0^\infty \ln(1+\varpi\lambda)\lambda^{\eta-1}e^{-\gamma\lambda}\mathrm{d}\lambda = \frac{(\eta-1)!}{e^{-\frac{\gamma}{\varpi}}\gamma^\eta}\sum_{l=1}^{\eta} E_{\eta-l+1}\left(\frac{\gamma}{\varpi}\right) \tag{30}$$

in [38, Appendix A]. Thus, the ergodic capacity at a typical UE position is given in (26). □

4 Wireless Friendliness Evaluation Scheme for Building Materials

In this section, we investigate how friendly a wall is to indoor LOS MIMO transmissions. Aiming to quantify the wireless friendliness of a building material, a reasonable indicator is the expectation of capacity $\mathbb{E}(C)$. However, the value of $\mathbb{E}(C)$ cannot be calculated straightforwardly. An alternative solution is to average the capacity values over dense sample points inside the room, since the limit of the mean capacity values over sample points equals $\mathbb{E}(C)$ as the sampling density approaches infinity.

Building a two-dimensional Cartesian coordinate system inside a $W\times L$ rectangular room as shown in Fig. 2, we take $X\times Y$ sample points spatially evenly distributed throughout the room. For a UE at the location (x_i,y_j) where $i\in\{1,2,...,X\}$ and $j\in\{1,2,...,Y\}$, its downlink ergodic capacity can be computed by (26)-(28) and denoted as $C\left(x_i,y_j\right)$ in bit/s/Hz. The capacity spatially averaged over all sample points, used as an evaluation indicator for

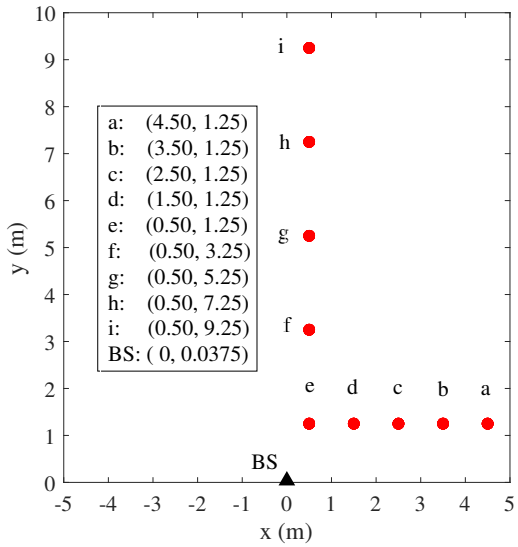

Fig. 2. Cartesian coordinates for a room, e.g. $W = L = 10$ (m), where the BS is close to the considered wall and there is an L-shaped route inside.

measuring the wireless friendliness of a building material, is given by

$$C_{\text{avg}} = \frac{1}{XY} \sum_{i=1}^{X} \sum_{j=1}^{Y} C\left(x_i, y_j\right). \tag{31}$$

According to [20], a simple expression of relative permittivity ε is given by $\varepsilon = \varepsilon_0 - j\varepsilon_1$, where the real part and the imaginary part can be expressed as a function of frequency f, i.e., $\varepsilon_0 = uf^v$ and $\varepsilon_1 = 17.98\sigma/f$, where $\sigma = rf^t$ is the conductivity of the building material, and constants u, v, r and t are compiled in [20, Table III]. In the following, we focus on the permittivity and thickness of the building material.

Permittivity: The permittivity in this paper refers to the real part of relative permittivity ε_0. The imaginary part is assumed to be a constant. Note that both ε and ε_0 are unitless.

Thickness: Since the building material in this paper is assumed to be a homogenous dielectric reflector, the building material's thickness of ζ equals to that of the wall.

The scheme for evaluating the wireless friendliness of a building material is given in Algorithm I. The permittivity ε_0 and the thickness ζ of a wall material are the inputs, and the output C_{avg} is computed following (31) as an indicator of its wireless friendliness. A higher

Algorithm 1: An Wireless Friendliness Evaluation Scheme for a Building Material

Input: ε_0, ζ, K, μ, W, L, X, Y, N_{T}, N_{R}, D, D_1, ρ_{T}
Output: C_{avg}
Calculate the step in x axis: $\Delta_x = \frac{W}{X}$;
Calculate the step in y axis: $\Delta_y = \frac{L-D_1}{Y-1}$;
Determine the coordinates (x,y) of all sample points :
$x = -W/2 + (\Delta_x/2) : \Delta_x : W/2 - (\Delta_x/2)$; $y = D_1 : \Delta_y : L$;
Determine the BS position located at $(0, D_1)$;
for $i = 1; i \leq X$ **do**
  for $j = 1; j \leq Y$ **do**
    Determine the UE location (x_i, y_j);
    Calculate d_1, d_2, θ_{T_1}, θ_{T_2}, θ_{R_1} and θ_{R_2}, α;
    Calculate Γ with (4)-(7);
    Constructe $\mathbf{H}$ with (8)-(13);
    Derive $C\left(x_i, y_j\right)$ with (26)-(28);
  end
end
Calculate C_{avg} with (31);
return C_{avg};

C_{avg} indicates that a wall made of this kind of material would be more friendly to indoor LOS MIMO communications.

5 Impact of directional radiation pattern

In this section, we consider each transmit element in the BS linear array as a directional antenna, as shown in Fig. 3. The main lobe directivity gain and the back lobe directivity gain are denoted as ν_{m} and ν_{b}, respectively, where $\nu_{\mathrm{m}}^2 + \nu_{\mathrm{b}}^2 = 2$ according to the energy conservation law. Due to the dynamic attitude of UE, we assume an omnidirectional antenna for the UE antenna for analytical tractability. The deterministic part of $\mathbf{H_1}$ should be rewritten accordingly as

$$\mathbf{H}_1' = \nu_{\mathrm{m}} A_1 \mathbf{h}_{\beta_1}^{\mathrm{H}} \mathbf{h}_{\alpha_1} + \nu_{\mathrm{b}} A_2 \mathbf{h}_{\beta_2}^{\mathrm{H}} \mathbf{h}_{\alpha_2}. \tag{32}$$

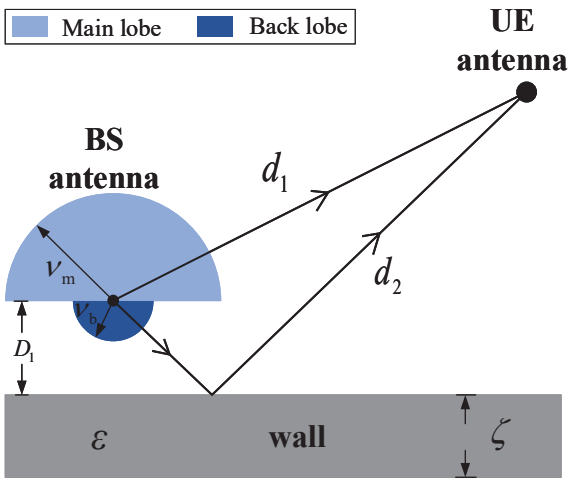

Fig. 3. The impact of the radiation pattern of a directional BS antenna on the EM propagation along the LOS path and the WR path.

The two non-zero squared singular values of $\mathbf{H}_1'$ are derived by replacing $\mathbf{X}$ in (14) and (15) with

$$\mathbf{X}' = \begin{bmatrix} v_m A_1 + v_b A_2 \Delta\beta\Delta\alpha & v_b A_2 \Delta\beta \, \|\mathbf{h}_{\alpha_*}\| \\ v_b A_2 \Delta\alpha \, \|\mathbf{h}_{\beta_*}\| & v_b A_2 \, \|\mathbf{h}_{\alpha_*}\| \, \|\mathbf{h}_{\beta_*}\| \end{bmatrix}. \tag{33}$$

The $\bar{K}$ in channel model (9)-(13), the squared singular distribution of channel (18)-(20) and the ergodic capacity (26)-(28) should all be replaced by K', where $K' = KS'$, K is the Rician factor given by (12), and

$$S' = \frac{\left\|\mathbf{H}_1'\right\|^2}{\left\|v_m A_1 \mathbf{h}_{\beta_1}^H \mathbf{h}_{\alpha_1}\right\|^2} = \frac{d_1^2 v_b^2}{d_2^2 v_m^2}|\Gamma|^2 + \frac{2Md_1 v_b}{N_T N_R d_2 v_m} + 1 \tag{34}$$

Meanwhile, the ergodic capacity $C(\rho')$ for directional antenna cases should be derived by the average SNR at each receiver antenna ρ', which is given by

$$\rho' = \frac{(K'+1)\left\|\mathbf{H}_1'\right\|^2 \rho_T}{K' N_R N_T} \tag{35}$$

TABLE I Main simulation assumption

Parameter name	**Parameter value**
Frequency f (GHz)	6
Room width W (m)	10
Room length L (m)	10
Inter-antenna spacing $D = \mu/2$ (m)	0.025
The distance from BS to wall D_1 (m)	0.0375
Number of BS antennas N_{T}	4
Number of UE antennas N_{R}	4
Samples along room x axis X	100
Samples along room y axis Y	100

The wireless friendliness evaluation scheme for directional BS antenna arrays is similar to Algorithm 1 by using (32)-(35).

6 Numerical results

In this section, we present and analyse the numerical results for both omnidirectional and directional BS antenna arrays to present a comprehensive understanding of the impact of building materials as reflectors on indoor LOS MIMO communications. Subsection 6.1-6.3 show the results for the omnidirectional BS antenna array, while Subsection D shows the results for the directional BS antenna array.

The parameters used in the simulations are given in Table I. The incident wave is assumed to be TE polarised. The transmission power of the BS is assumed to be equally allocated to every transmit antenna element. The BS is deployed at point $(0, D_1)$ and its antenna array is deployed parallel to the considered wall. In the Monte Carlo simulations, the ergodic capacity at point (x_i, y_j) is computed by

$$C_{\mathrm{sim}}\left(x_i, y_j\right) = \mathbb{E}\left[\log_2 \det\left(\mathbf{I} + \frac{\rho}{N_{\mathrm{T}}}\mathbf{H}\mathbf{H}^{\dagger}\right)\right]. \tag{36}$$

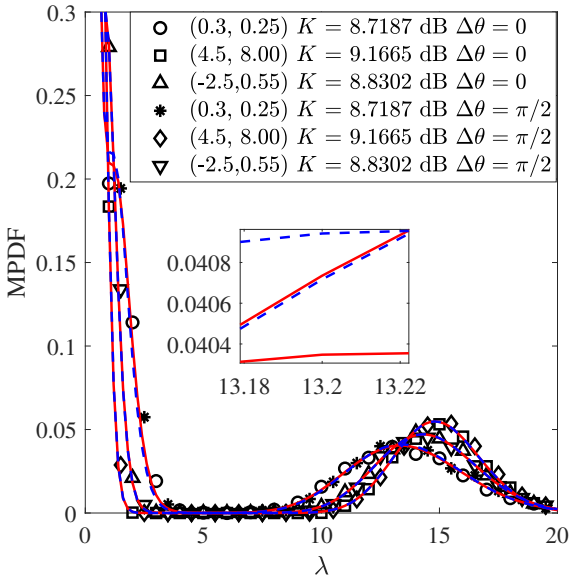

Fig. 4. The MPDF of an unordered squared singular value at three points, for $\zeta = 0.2$, $\varepsilon = 5.31 - j0.5861 f^{-0.1905}$ [20, Table III]. Markers represent simulation values while red solid lines and blue dash lines represent analytical values when $\Delta\theta = 0$ and $\Delta\theta = \pi/2$, respectively.

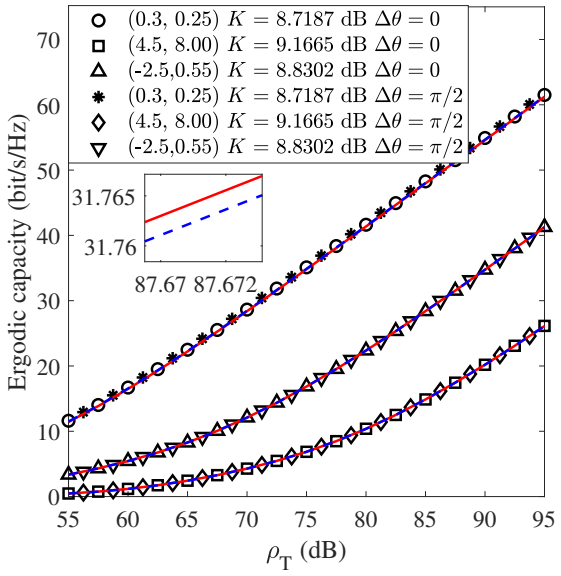

Fig. 5. Relationship between ergodic capacity and transmit SNR at three points, for $\zeta = 0.2$, $\varepsilon = 5.31 - j0.5861 f^{-0.1905}$. Markers represent simulation values while red solid lines and blue dash lines represent analytical values when $\Delta\theta = 0$ and $\Delta\theta = \pi/2$, respectively.

6.1 The ergodic capacity for a specific sample point

In this subsection, we take three points, i.e. (0.3, 0.25), (4.5, 8.0) and (-2.5, 0.55), as examples to verify the correctness of analytical expression of (18)-(20) and (26)-(28). The Rician factor K of the three points is computed by (12) accordingly.

Fig. 4 depicts the MPDF of an unordered squared singular value of the LOS MIMO channel. It is found that the MPDF becomes more concentrated as K is reduced, which reveals that the squared singular values of matrix $\mathbf{H}$ are more evenly distributed and thus results in a larger ergodic capacity.

Fig. 5 shows the ergodic capacity versus the transmit SNR. The ergodic capacity increases when the transmit SNR increases. Meanwhile, a larger K leads to a lower ergodic capacity under the same transmit SNR due to the less concentrated MPDF of an unordered squared singular value of channel matrix $\mathbf{H}$.

From the results for $\Delta\theta$ being 0 and $\pi/2$ in Fig. 4 and Fig. 5, respectively, we can see that $\Delta\theta$ has a limited impact on the MPDF of an unordered squared singular value and the ergodic capacity of indoor LOS MIMO channel. This is because $\Delta\beta$ in (16) is hardly affected by $\Delta\theta$. When $\Delta\theta$ increase from 0 to π, $\Delta\beta$ is always very close to 1. As a result, the squared singular values of $\mathbf{H}$ derived by (14)-(15) will not change much with $\Delta\theta$. Consequently, the MPDF of an unordered squared singular value in (18)-(20) and the ergodic capacity in (26)-(28) of $\mathbf{H}$ will stay nearly constant for varying $\Delta\theta$. Therefore, due to the space limitation, all the numerical results hereinafter are conducted when $\Delta\theta = 0$.

6.2 The ergodic capacity distribution in a square room

To verify the accuracy of the evaluation indicator C_{avg} in (31) and the usefulness of Algorithm 1, the ergodic capacity at different positions is studied in this subsection.

We design a L-shaped route that includes some typical UE positions in the square room, as shown in Fig. 2. The ergodic capacities from point a to j along this route, in the presence or absence of WR path, are shown in Fig. 6. The dash lines illustrate the results taking into account the WR path. From point a to e, we observe an increase in capacity as the

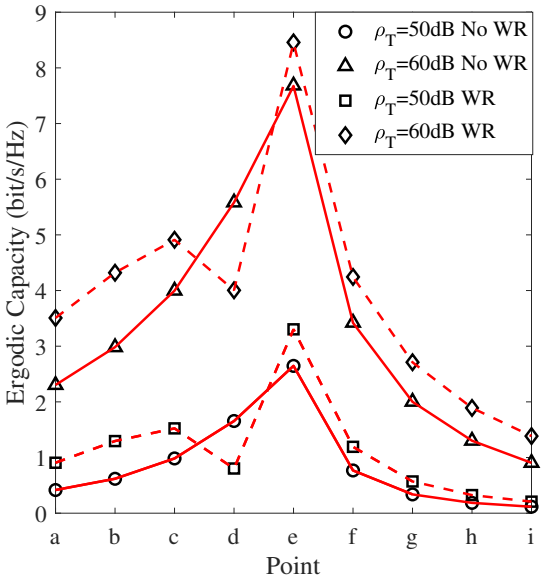

Fig. 6. Ergodic capacity at the points for L-shaped route, for $\zeta = 0.2$, $\varepsilon = 5.31 - j0.5861 f^{-0.1905}$. Markers represent simulation values while both the solid and dash lines represent analytical values.

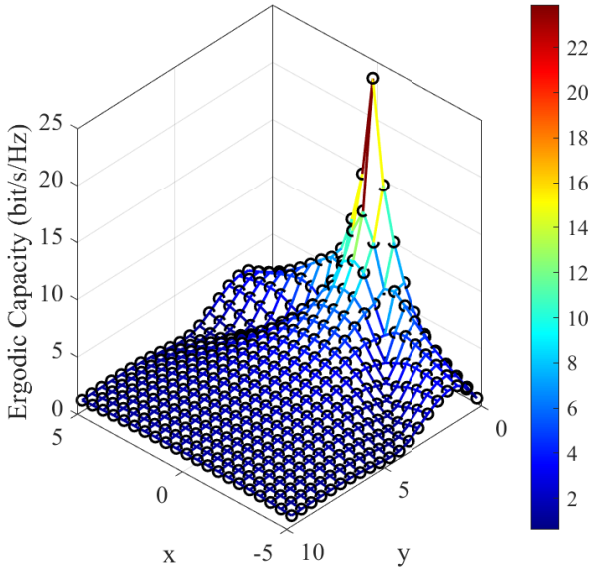

Fig. 7. Ergodic capacity distribution in the 10 m $\times$ 10 m square room, for $\rho_T = 60$ dB, $\zeta = 0.2$, $\varepsilon = 5.31 - j0.5861 f^{-0.1905}$. Markers represent simulation values while the lines represent analytical values.

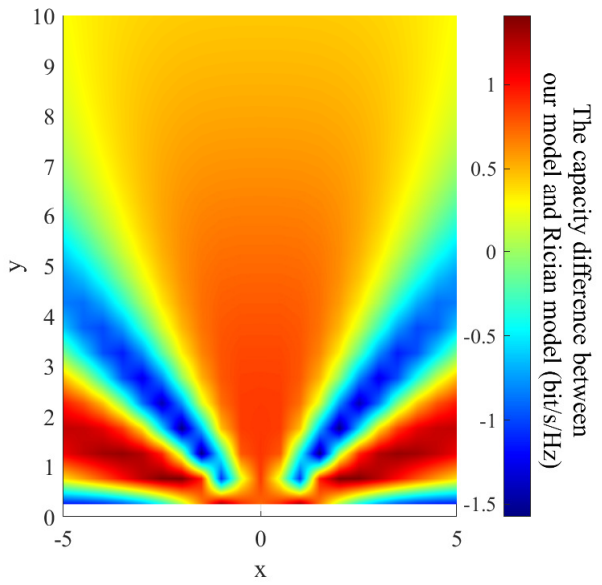

Fig. 8. The ergodic capacity difference between our proposed channel and the Rician channel, for $\rho_{\mathrm{T}} = 60$ dB, $\zeta = 0.2$, $\varepsilon = 5.31 - j0.5861 f^{-0.1905}$. The positive/negative difference indicates constructive/destructive interference.

UE is approaching the BS except for point d, where the slump in ergodic capacity is due to the power cancellation caused by the destructive combination of the LOS path and the WR path. When the UE moves from point e to i, the capacity declines. This is different from the ergodic capacity under the Rician fading model without considering the WR path that would monotonically decrease with an increasing UE-BS distance, as shown by the solid lines in Fig. 6.

The spatial distribution of the ergodic capacity in a square room using our proposed model is shown in Fig. 7. It is observed that the ergodic capacity is not a monotonic function of the UE-BS distance. This phenomenon can be attributed to the constructive and destructive interference between the EM waves along the LOS path and the WR path. The length difference in $O(\lambda)$ leads to the great changes of the amplitude and phase of the superposed EM wave arriving at the UE.

Fig. 8 plots the ergodic capacity difference between our proposed channel model based on (8)-(13) and the Rician fading channel model. The position with a positive/negative difference corresponds to a location that experiences the constructive/destructive interference

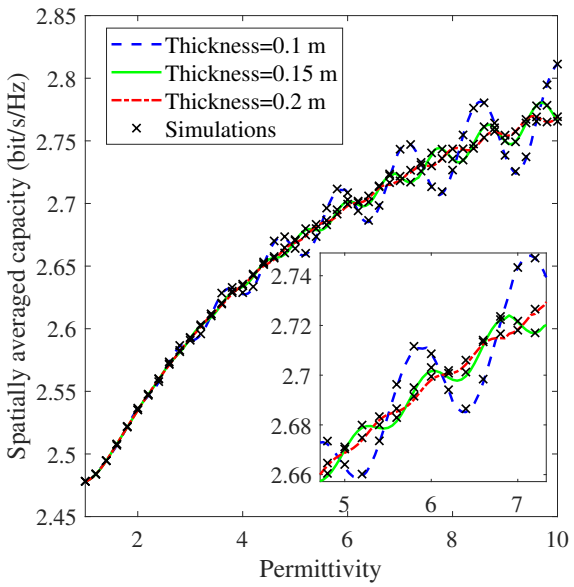

Fig. 9. Impact of wall permittivity on spatially averaged capacity for the omnidirectional BS antenna array for $\rho_{\mathrm{T}} = 60$ dB.

between the EM waves along the LOS path and the WR path. We can see that the positions suffering from the destructive interference appear in certain directions, along which the Fabry-Pérot resonance phenomenon of EM waves is observed.

Concluded from Fig. 6-8, the impact of the WR path that characterises the EM and physical properties of building materials on indoor ergodic capacity is non-trivial, which cannot be ignored in indoor LOS MIMO communications.

6.3 The impact of wall permittivity and thickness on spatially averaged capacity

In order to identify a wall material with desirable wireless friendliness, the relationship between the evaluation indicator named spatially averaged capacity C_{avg} and the key parameters, i.e., the permittivity ε_0 and the thickness ζ of building materials is shown in this subsection.

Fig. 9 and Fig. 10 plot the spatially averaged capacity as a function of the permittivity and the thickness of building materials, respectively. In Fig. 9, as the permittivity increases

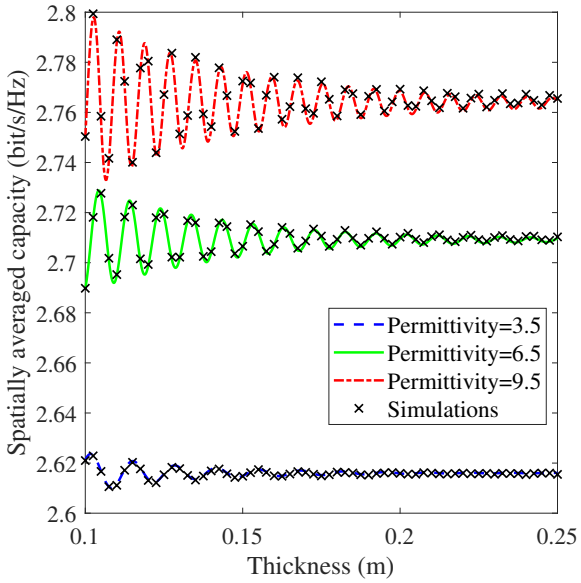

Fig. 10. Impact of wall thickness on spatially averaged capacity for the omnidirectional BS antenna array for $\rho_{\mathrm{T}} = 60$ dB.

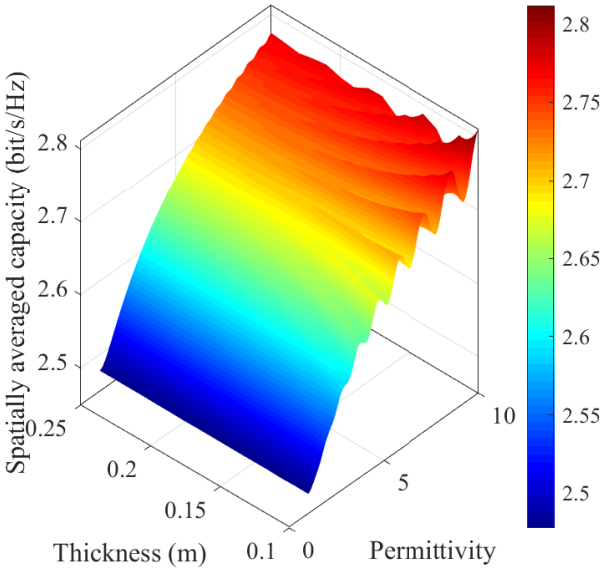

Fig. 11. The composite impact of permittivity and thickness on spatially averaged capacity for the omnidirectional BS antenna array for $\rho_{\mathrm{T}} = 60$ dB.

from 1 to 10, the envelope of the spatially averaged capacity presents a upward trend. The variation in the spatially averaged capacity becomes more significant with the increase of the permittivity. In Fig. 10, for a given permittivity, as the wall thickness increases, the spatially averaged capacity first fluctuates with it under a decreasing envelope and gradually converges to a constant value when the thickness goes beyond 0.25 m. We observe quite severe fluctuations of the spatially averaged capacity at relatively small wall-thickness values. That is because the reflection coefficient amplitude fluctuates more severely when the wall is thinner. According to Fig. 9 and Fig. 10, we note that a tiny lapse in the wall permittivity or thickness will change the spatially averaged capacity by up to 0.333 bit/s/Hz.

The composite impact of the building material's permittivity and thickness on the spatially averaged capacity is illustrated in Fig. 11. When the permittivity and the thickness are configured in the range from 1 to 10 and from 0.1 to 0.25 m, respectively, we observe that the optimal pair of $[\varepsilon_0, \zeta]$ resulting in the highest spatially averaged capacity of 2.812 bit/s/Hz is [10, 0.1], while the worst pair resulting in the lowest spatially averaged capacity of 2.478 bit/s/Hz is [1, 0.1]. We can conclude that certain combinations of the wall thickness and permittivity values lead to peak values of the spatially averaged capacity, which can be more than 13.5% higher than the lowest spatially averaged capacity values. The combinations of the wall thickness and permittivity values associated with the latter should be avoided during the selection and/or design of building materials.

6.4 Analysis for directional BS antenna array

In this subsection, Fig. 12-17 depict the numerical results for the directional BS antenna array. The main lobe directivity gain and the back lobe directivity gain are assumed as $\nu_{\mathrm{m}} = \sqrt{1/3}$ and $\nu_{\mathrm{b}} = \sqrt{5/3}$, respectively.

Fig. 12 and Fig. 13 are plotted for the same three sample points shown in Fig. 4 and Fig. 5, i.e. (0.3, 0.25), (4.5, 8.0) and (-2.5, 0.55). It is found in Fig. 12 that the MPDF of an unordered squared singular value of the LOS MIMO channel becomes more concentrated and that the largest squared singular value of the LOS MIMO channel becomes larger, when compared with the omnidirectional BS antenna array in Fig. 4. Moreover, the difference

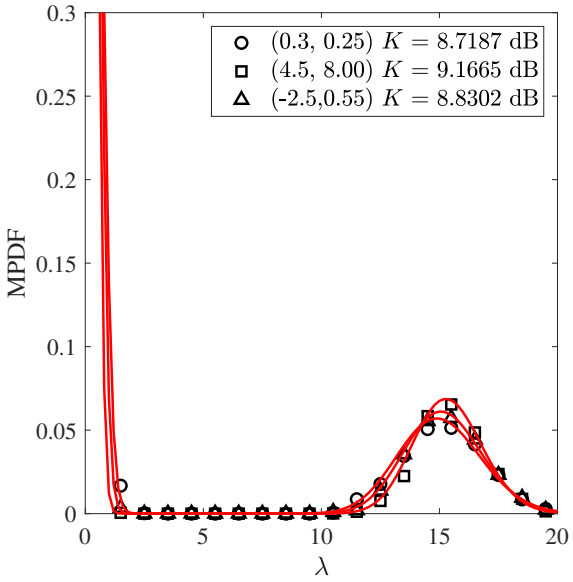

Fig. 12. The MPDF of an unordered squared singular value at three points, for $\zeta = 0.2$, $\varepsilon = 5.31 - j0.5861 f^{-0.1905}$. Markers represent simulation values while lines represent analytical values.

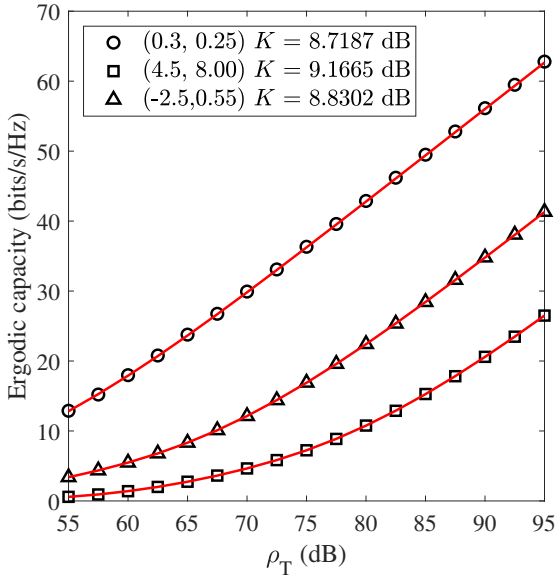

Fig. 13. Relationship between ergodic capacity and transmit SNR at three points, for $\zeta = 0.2$, $\varepsilon = 5.31 - j0.5861 f^{-0.1905}$. Markers represent simulation values while lines represent analytical values.

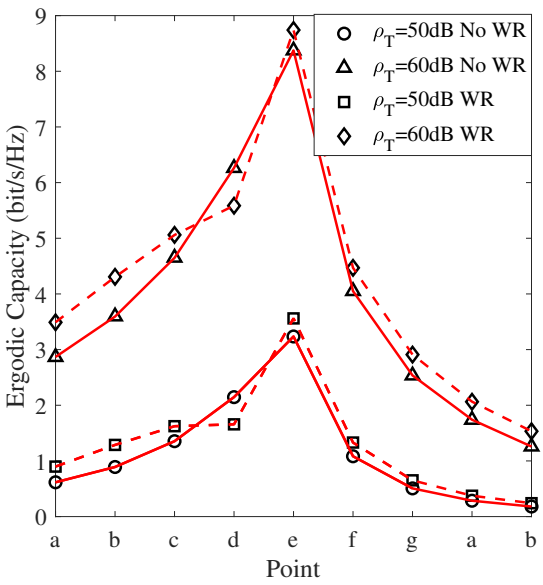

Fig. 14. Ergodic capacity at the points for L-shaped route, for $\zeta = 0.2$, $\varepsilon = 5.31 - j0.5861 f^{-0.1905}$. Markers represent simulation values while both the solid and dash lines represent analytical values.

between the MPDF under different Rician factor K becomes less substantial. In Fig. 13, the ergodic capacity shows an increasing trend with the rise of transmit SNR. When comparing the red lines in Fig. 5 with the red lines in Fig. 13, the ergodic capacity under the directional BS antenna array is shown to be larger than that under the omnidirectional BS antenna array.

Given the same 9 points along the L-route drawn in Fig. 2, Fig. 14 shows similar results from Fig. 6. Even though there is less change in ergodic capacity in the presence or absence of the WR path compared with the omnidirectional BS antenna array, it still appears some positions that suffer destructive interference, such as point d.

With regards to the impact of the wall permittivity and thickness on the spatially averaged capacity, significant variations of up to 0.151 bit/s/Hz can be observed in Fig. 15 and Fig. 16. In Fig. 17, it is found that the optimal pair of $[\varepsilon_0, \zeta]$ leading to the highest spatially averaged capacity of 3.292 bit/s/Hz is [10, 0.1], while the worst pair leading to the lowest spatially averaged capacity of 3.141 bit/s/Hz is [1, 0.1]. The potential 4.8% difference in the spatially averaged capacity generated by different combinations of the wall permittivity and thickness is worthy of careful consideration in the selection and/or design of building materials.

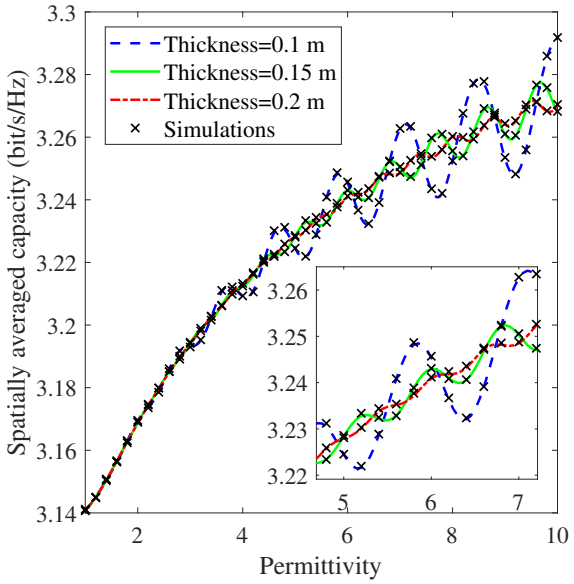

Fig. 15. Impact of wall permittivity on spatially averaged capacity for the directional BS antenna array for $\rho_{\mathrm{T}} = 60$ dB.

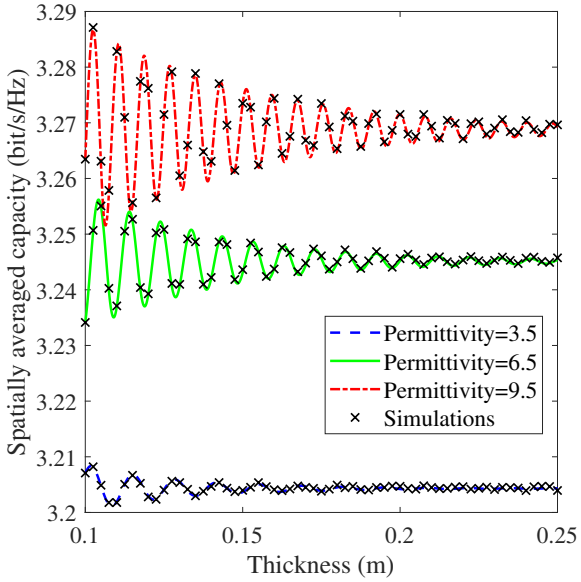

Fig. 16. Impact of wall thickness on spatially averaged capacity for the directional BS antenna array for $\rho_{\mathrm{T}} = 60$ dB.

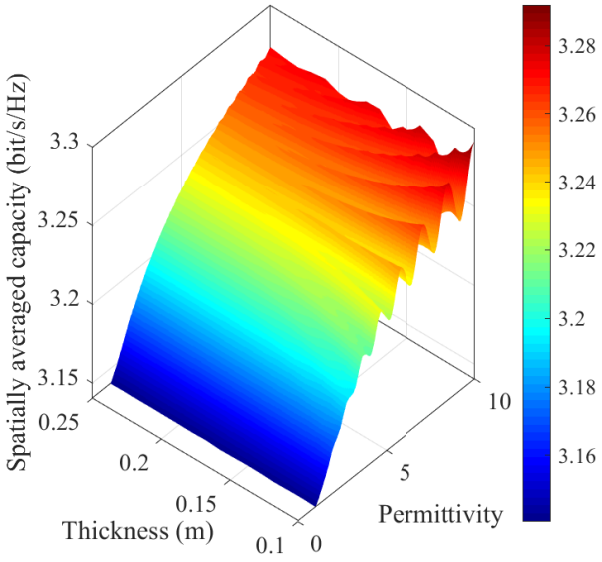

Fig. 17. The composite impact of permittivity and thickness on spatially averaged capacity for the directional BS antenna array for $\rho_{\mathrm{T}} = 60$ dB.

The results above indicate that for directional BS antenna arrays, the EM and physical properties of building materials will definitely exert a substantial influence on a room's wireless performance.

7 Conclusions and Future works

In this paper, we firstly construct a new indoor LOS MIMO downlink channel model by considering the impact of building materials on indoor wireless performance. Then, the MPDF of the squared singular value and the ergodic capacity of the indoor LOS MIMO channel and the squared singular value of its deterministic part are obtained in closed forms. On this basis, a scheme for evaluating the wireless friendliness of building materials is provided. The analytical results are verified through Monte Carlo simulations conducted in the 6 GHz band. Numerical results demonstrate that building materials as reflectors have to be well selected or designed to avoid the risk of reducing indoor wireless performance, because a minor discrepancy in the configuration of the relative permittivity and thickness of the wall material might cause over 14.4% losses in indoor capacity.

This work is the first attempt to investigate how indoor capacity is influenced by the EM and physical properties of building materials, which has laid a solid foundation of wireless friendliness evaluation of indoor built environments. In future works, there are some extensive research directions worthy of in-depth study, including but not limit to:

1) Multi-layer building materials: It is of great necessity to analyse both single-layer and multi-layer building materials. One of the challenges is that the analytical relationship between the indoor MIMO capacity and the EM and physical properties of multi-layer building materials is hard to find due to the non-closed-form reflection coefficients [20]. Moreover, the optimal configuration of multi-layer materials would be formulated into a multi-variate optimisation problem, the complexity of which would increase with the number of layers.

2) Millimetre wave (mmWave): MmWave bands have been a promising candidate for 5G and B5G wireless network, which has been widely studied in both theoretical and experimental study. The propagation mechanism for sub-6 GHz bands and mmWave bands are substantially different due to the orders of magnitude change in the wavelength [10, 15, 39]. Hence, the work extending to mmWave bands should start from the accurate and tractable modelling of indoor mmWave propagation. Another scheme is required to evaluate the wireless friendliness of building materials at mmWave bands.

3) Experimental validation: It is critical to verify the numerical results of the proposed channel model and the evaluation scheme with experimental results. A comprehensive measurement campaign will be held in future work.

Appendix: Proof of Lemma 1

Since two deterministic components including the LOS path and the WR path are considered in our model as shown in (8), it is obvious that $\mathbf{H_1}$ has two non-zero singular values. The singular value decomposition of deterministic part $\mathbf{H_1}$ can be given as

$$\mathbf{H_1} = \mathbf{B}^{\mathrm{H}}\mathbf{X}\mathbf{A}, \tag{37}$$

where

$$\mathbf{B} = \begin{pmatrix} \mathbf{h}_{\beta_1} & \mathbf{h}_{\beta_*} / \left\| \mathbf{h}_{\beta_*} \right\| \end{pmatrix}^{\mathrm{T}},$$

$$\mathbf{A} = \begin{pmatrix} \mathbf{h}_{\alpha_1} & \mathbf{h}_{\alpha_*} / \left\| \mathbf{h}_{\alpha_*} \right\| \end{pmatrix}^{\mathrm{T}},$$

$$\mathbf{X} = \begin{pmatrix} 1 & \Delta\beta \\ 0 & \left\| \mathbf{h}_{\beta_*} \right\| \end{pmatrix} \begin{pmatrix} A_1 & 0 \\ 0 & A_2 \end{pmatrix} \begin{pmatrix} 1 & 0 \\ \Delta\alpha & \left\| \mathbf{h}_{\alpha_*} \right\| \end{pmatrix}.$$

Initially using Gram-Schmidt process, $\mathbf{h}_{\alpha_1}$ and $\mathbf{h}_{\beta_1}^{\mathrm{H}}$ are orthonormalized with $\mathbf{h}_{\alpha_*} / \left\| \mathbf{h}_{\alpha_*} \right\|$ and $\mathbf{h}_{\beta_*}^{\mathrm{H}} / \left\| \mathbf{h}_{\beta_*} \right\|$, respectively, which means that $\mathbf{B}^{\mathrm{H}}\mathbf{B} = \mathbf{I}$ and $\mathbf{A}^{\mathrm{H}}\mathbf{A} = \mathbf{I}$.

Then $\mathbf{X}$ can be simplified as a 2×2 matrix, with four elements given in (14). Assuming $\mathbf{X}$ could be decomposed as

$$\mathbf{X} = \mathbf{P}^{\mathrm{H}} \begin{pmatrix} \sqrt{\varphi_{m-1}} & 0 \\ 0 & \sqrt{\varphi_m} \end{pmatrix} \mathbf{Q}, \tag{38}$$

where $\mathbf{P}^{\mathrm{H}}\mathbf{P} = \mathbf{I}$ and $\mathbf{Q}^{\mathrm{H}}\mathbf{Q} = \mathbf{I}$, then φ_{m-1} and φ_m are two squared singular values of matrix $\mathbf{X}$. Hence we obtain

$$\mathbf{H_1} = (\mathbf{PB})^{\mathrm{H}} \begin{pmatrix} \sqrt{\varphi_{m-1}} & 0 \\ 0 & \sqrt{\varphi_m} \end{pmatrix} \mathbf{QA}. \tag{39}$$

Here it is interesting to find that φ_{m-1} and φ_m are the two squared singular values of $\mathbf{H_1}$ as well, since $(\mathbf{PB})^{\mathrm{H}}\mathbf{PB} = \mathbf{I}$ and $(\mathbf{QA})^{\mathrm{H}}\mathbf{QA} = \mathbf{I}$.

Therefore, the two non-zero squared singular values of $\mathbf{H_1}$, i.e. φ_{m-1} and φ_m, can be easily obtained by conducting singular value decomposition to low dimensional matrix $\mathbf{X}$, as given in (14) and (15), respectively.

References

[1] D. Minoli, *et al.*, "IoT considerations, requirements, and architectures for smart buildings-energy optimization and next-generation building management systems," *IEEE Internet Things J.*, vol. 4, no. 1, pp. 269-283, Feb. 2017.

[2] X. Zhang, *et al.*, "An IoT-based thermal model learning framework for smart buildings," *IEEE Internet Things J.*, vol. 7, no. 1, pp. 518-527, Jan. 2020.

[3] Y. Li, *et al.*, "Smart choice for thesmart grid: narrowband internet of things (NB-IoT)," *IEEE Internet Things J.*, vol. 5, no. 3, pp. 1505-1515, Jun. 2018.

[4] J. Santos, *et al.*, "City of things: enabling resource provisioning in smartcities," *IEEE Commun. Mag.*, vol. 56, no. 7, pp. 177-183, Jul. 2018.

[5] J. G. Andrews, *et al.*, "What will 5G be?" *IEEE J Sel. Areas Commun.*, vol. 32, no. 6, pp. 1065-1082, June, 2014.

[6] G. Gui, *et al.*, "6G: opening new horizons for integration of comfort, security and intelligence," *IEEE Wireless Commun. Mag.*, early access, 2020.

[7] Cisco, "Cisco vision: 5G-thriving indoors," Feb. 2017. [Online]. Available: cisco.com/c/dam/en/us/solutions/collateral/service-provider/ultra-services-platform/5g-ran-indoor.pdf

[8] Huawei, "Five trends to small cell 2020," *Mobile World Congress (MWC)*, Barcelona, Spain, Feb. 2016.

[9] J. Zhang, *et al.*, "Wireless energy efficiency evaluation for buildings under design based on analysis of interference gain," *IEEE Trans. Veh. Tech.*, early access, 2020.

[10] E. Bjornson, *et al.*, "Massive MIMO in sub-6 GHz and mmWave: physical, practical, and use-case differences," *IEEE Wireless Communications*, vol. 26, no. 2, pp. 100-108, April 2019.

[11] M. Jensen and J. Wallace, "A review of antennas and propagation for MIMO wireless communications," *IEEE Trans. Antennas Propag.*, vol. 52, no. 11, pp. 2810–2824, Nov. 2004.

[12] J. Zhang, *et al.*, "Bit error probability of spatial modulation over measured indoor channels," *IEEE Trans. Wirel. Commun.*, vol. 13, no. 3, pp. 1380-1387, March 2014.

[13] Y. Yang, *et al.*, "Multiband MIMO antenna for GSM, DCS, and LTE indoor applications," *IEEE Antennas Wireless Propagat. Lett.*, vol. 15, pp. 1573-1576, Jan. 2016.

[14] D. S. Shiu, *et al.*, "Fading correlation and its effect on the capacity of multielement antenna systems," *IEEE Trans. Commun.*, vol. 48, no. 3, pp. 502-513, March 2000.

[15] K. Haneda, *et al.*, "Indoor 5G 3GPP-like channel models for office and shopping mall environments," *IEEE International Conference on Communications Workshops (ICC)*, Kuala Lumpur, 2016, pp. 694-699.

[16] S. K. Yoo, *et al.*, "Ceiling- or wall-mounted access points: an experimental evaluation for indoor millimeter wave communications," *13th European Conference on Antennas and Propagation (EuCAP)*, Krakow, Poland, 2019, pp. 1-5.

[17] G. Narimani, *et al.*, "Analysis of ultrawideband pulse distortion due to lossy dielectric walls and indoor channel models," *IEEE Trans. Antennas Propag.*, vol. 64, no. 10, pp. 4423-4433, Oct. 2016.

[18] C. Jansen, *et al.*, "The impact of reflections from stratified building materials on the wave propagation in future indoor terahertz communication systems," *IEEE Trans. Antennas Propag.*, vol. 56, no. 5, pp. 1413-1419, May 2008.

[19] F. Sagnard and G. E. Zein, "In situ characterization of building materials for propagation modeling: frequency and time responses," *IEEE Trans. Antennas Propag.*, vol. 53, no. 10, pp. 3166-3173, Oct. 2005.

[20] "Effects of building materials and structures on radiowave propagation above about 100 MHz P series radiowave propagation," IETF, ITU Recommendation P.2040-1, Jul. 2015.

[21] L. Azpilicueta, *et al.*, "Impact of material changes in electromagnetic dosimetry estimation of complex indoor scenarios," *European Conference on Antennas and Propagation (EUCAP)*, Prague, 2012, pp. 2048-2050.

[22] V. Degli-Esposti, *et al.*, "A method for the electromagnetic characterization of construction materials based on Fabry–Pérot resonance," *IEEE Access*, vol. 5, pp. 24938-24943, Oct. 2017.

[23] H. Tian, *et al.*, "Effect level based parameterization method for diffuse scattering models at millimeter-wave frequencies," *IEEE Access*, vol. 7, pp. 93286-93293, July 2019.

[24] J. Luo, *et al.*, "Complex permittivity estimation for construction materials based on PSO method," *Proc. IEEE International Symposium on Antennas and Propagation and USNC-URSI Radio Science Meeting*, pp. 1045-1046, July 2019.

[25] J. Zhang, *et al.*, "Two-ray reflection resolution algorithm for planar material electromagnetic property measurement at the millimeter-wave bands," *Radio Science*, early access.

[26] C. Liaskos, *et al.*, "A new wireless communication paradigm through software-controlled metasurfaces," *IEEE Commun. Mag.*, vol. 56, no. 9, pp. 162–169, Sep. 2018.

[27] M. Faenzi, *et al.*, "Metasurface antennas: new models, applications and realizations," *Sci. Rep.*, vol. 9, no. 1, pp. 1–14, Jul. 2019.

[28] Q. Wu and R. Zhang, "Intelligent reflecting surface enhanced wireless network via joint active and passive beamforming," *IEEE Trans. Wirel. Commun.*, vol. 18, no. 11, pp. 5394-5409, Nov. 2019.

[29] E. Björnson and L. Sanguinetti, "Demystifying the power scaling law of intelligent reflecting surfaces and metasurfaces," Aug. 2019. [Online]. Available: https://arxiv.org/pdf/1908.03133.pdf

[30] E. Björnson, *et al.*, "Intelligent reflecting surface vs. decode-and-forward: how large surfaces are needed to beat relaying?," Jun. 2019. [Online]. Available: https://arxiv.org/pdf/1906.03949.pdf.

[31] D. Pena, *et al.*, "Measurement and modeling of propagation losses in brick and concrete walls for the 900-MHz band," *IEEE Trans. Antennas Propag.*, vol. 51, no. 1, pp. 31-39, Jan. 2003.

[32] B. Feitor, *et al.*, "Estimation of dielectric concrete properties from power measurements at 18.7 and 60 GHz," *Loughborough Antennas & Propagation Conference*, Loughborough, 2011, pp. 1-5.

[33] M. B. Zetterberg, *et al.*, "IST-2003-507581 WINNER D5.4 v1.4 final report on link level and system level channel models," Nov. 2005.

[34] EU H2020 AceLSAA Project. [Online]. Available: https://cordis.europa.eu/project/id/752644

[35] E. Torkildson, *et al.*, "Indoor millimeter wave MIMO: feasibility and performance," *IEEE Trans. Wirel. Commun.*, vol. 10, no. 12, pp. 4150-4160, Dec. 2011.

[36] G. Alfano, *et al.*, "Mutual information and eigenvalue distribution of MIMO ricean channels," *Proc. IEEE Int. Symp. Inf. Theory Appl. (ISITA)*, Parma, Italy, Oct. 2004, pp. 1-6.

[37] A. Maaref and S. Aïssa, “Capacity of MIMO Rician fading channels with transmitter and receiver channel state information,” *IEEE Trans. Wirel. Commun.*, vol. 7, no. 5, pp. 1687–1698, May 2008.

[38] M. Alouini and A. J. Goldsmith, “Capacity of Rayleigh fading channels under different adaptive transmission and diversity-combining techniques,” *IEEE Trans. Veh. Technol.*, vol. 48, no. 4, pp. 1165-1181, Jul. 1999.

[39] I. A. Hemadeh, *et al.*, “Millimeter-wave communications: physical channel models, design considerations, antenna constructions, and link-budget," *IEEE Commun. Surveys Tuts.*, vol. 20, no. 2, pp. 870-913, Secondquarter 2018.

Paper II

Lower-bound Capacity Based Wireless Friendliness Evaluation for Walls as Reflectors

Yixin Zhang, Jiliang Zhang, Xiaoli Chu, and Jie Zhang.

Published in *IEEE Transactions on Broadcasting, Volume: 67, Issue: 4, Pages: 917-924, Dec. 2021.* Date of Publication: 27 Sep. 2021.

Lower-bound Capacity Based Wireless Friendliness Evaluation for Walls as Reflectors

Yixin Zhang[1], Jiliang Zhang[1], Xiaoli Chu[1], Jie Zhang[1,2]

[1] Department of Electronic and Electrical Engineering, the University of Sheffield, Sheffield, S10 2TN, UK

[2] Research and Development Department, Ranplan Wireless Network Design Ltd., Cambridge, CB23 3UY, UK

Abstract

Indoor base stations (BSs) equipped with multiple-input multiple-output (MIMO) antenna arrays are commonly deployed in the vicinity of a wall. The wireless friendliness of the wall, determined by the intrinsic electromagnetic (EM) and physical properties of the wall material, significantly influences the indoor wireless performance and thus needs to be thoroughly considered during building design. In this article, for a rectangular room with a BS deployed near one of the walls, by deriving the asymptotic expression of lower-bound indoor wireless capacity of a UE location-specific channel, we reveal that the impact of the BS transmission power and that of the wall material properties on the lower-bound indoor capacity can be decoupled. More specifically, in our derived lower-bound indoor wireless capacity, the properties of the wall material are captured by the logarithmic eigenvalue summation (LES) and logarithmic eigenvalue product (LEP), which are both independent of the BS transmit signal-to-noise ratio (SNR). To simplify the wireless-friendliness evaluation of a wall by leveraging such decoupling, we derive both the LES and LEP in closed forms for a UE location-specific channel, and define the spatially averaged LES, the spatially averaged LEP, and the upper-bound outage probability (all over the room of interest) as new metrics for fast evaluating the wireless friendliness of the wall closest to the BS. Numerical results verify the effectiveness of the three proposed metrics and reveal the crucial impact of room settings and wall materials on the indoor capacity. The proposed approach will enable architects and civil engineers to quickly select building materials according to their wireless friendliness.

1 Introduction

It is predicted that mobile video will rise to account for nearly 80% of all mobile data traffic by 2022, while 70% to 90% of the overall mobile data will be generated indoors [1]. Superior indoor multimedia experience can be supported by the wireless broadcast services [2–4] of mobile networks, e.g., with the LTE-Broadcast (LTE-B) technology [5]. It is noteworthy that an indoor mobile network needs to ensure a high capacity to support high-data-rate services such as live video streaming [6].

Multiple-input multiple-output (MIMO) technique can be used to boost indoor wireless performance by enabling multiple parallel spatial streams between transceivers without requiring additional bandwidth or higher transmission power [7–9]. To avoid any negative visual impact or inconvenience on a room, a popular way of deploying indoor base stations (BSs) equipped with MIMO antenna arrays is to put the BSs in the edge part of a room, i.e., close to a wall [10, 11].

The settings of indoor environments, in terms of room sizes and aspect ratios, wall material's thicknesses and relative permittivities, and BS locations and configurations, will affect the indoor wireless performance [12–15]. As such, the materials of walls have to be carefully selected taking their impacts of properties on the indoor wireless performance into account in the building planning and design stage. Generally, the wall in the vicinity of a BS can be regarded as a lossy dielectric structure [16–18]. An electromagnetic (EM) wave would suffer reflection loss after hitting on the wall's surface due to multiple internal reflections. Measurement results have shown that the reflection loss is dependent on the incident angles and polarisation of EM waves, as well as the EM and physical properties of wall materials [19, 20], which is mathematically characterised by the Fresnel equations [16, 21–23].

The authors in [24, 25] utilized frequency-selective surfaces (FSSs) to change the EM properties of the walls in real-time for the purpose of providing good EM isolation between rooms. Nevertheless, FSS attached walls were studied only as active spatial and frequency filters, while the impact of other EM parameters of walls, such as permittivity and conductivity, on indoor wireless capacity was not investigated.

In order to predict the impact of a wall that is closest to the BS on the indoor wireless performance, we proposed wireless friendliness as a new performance metric of a wall in [26], where we also developed an approach to evaluating the wireless friendliness of a wall by adopting the indoor spatially averaged capacity of a multipath channel as a metric, which is a function of and is affected by the BS transmission power. Note that the capacity of the two-ray channel comprising of the line-of-sight (LOS) path and the wall reflection (WR) path [18, 27] and the capacity of a multipath channel that incorporates other multipath components in addition to the LOS path and the WR path have the same monotonicity, which can be proven using the results in [28]. Therefore, in this work, we propose to study a wall's wireless friendliness based on the capacity of the two-ray channel. By exploiting the asymptotic capacity of this two-ray channel, we find that its eigenvalues can be used to separate the BS transmit signal-to-noise ratio (SNR) from the interference between the LOS path and the WR path that determines the wireless friendliness of the wall. As will be shown in Section II, by leveraging the logarithmic sum or logarithmic product of the eigenvalues of the two-ray channel, the influence of the BS transmission power on a wall's wireless friendliness can be removed. Consequently, compared with the metric in [26], the three new metrics proposed herein no longer require the calculation of the following four parameters: the BS transmit SNR, the power ratio of the LOS and WR paths to the other multipath components, and the two eigenvalues of the two-ray channel, which facilitates a faster and simpler approach to evaluating a wall's wireless friendliness.

In this article, we investigate how the transverse dimension (equal to the length or width of a room), longitudinal dimension (thickness), and dielectric properties (relative permittivity and conductivity) of the wall closest to the BS affect the indoor LOS MIMO downlink transmissions in a rectangular room, which may have various room sizes, aspect ratios, and distances between the BS and its closest wall. Given that the wall closest to the BS would exert a much greater impact on the received signal strength than the other walls due to the dominating distance-dependent path loss over the much weaker reflection gain [26], in this article, we focus on the wireless friendliness evaluation of the wall closest to the BS. For brevity, the wall closest to the BS in a room is referred to as the wall hereafter.

The contributions of this work are summarised as follows:

- We adopt a two-ray channel model incorporating both the LOS path and the WR path from the BS's closest wall, and derive the lower-bound capacity per unit bandwidth in the medium and high SNR regimes for an arbitrary user equipment (UE) location in closed-form.
- We show that, while being independent of the BS transmit SNR, the logarithmic eigenvalue sum (LES) and logarithmic eigenvalue product (LEP) in the derived lower-bound capacity per unit bandwidth of a UE location-specific channel can jointly characterise the wireless friendliness of the wall.
- Based on the UE location-specific LES and LEP, we propose the spatially averaged LES, the spatially averaged LEP, and the upper-bound outage probability of the room as new metrics for evaluating the wall's wireless friendliness. Note that the three proposed metrics for fast evaluating the wireless friendliness of a wall as a reflector can be applied to every wall in the considered room when the channel model takes the WRs from that wall into consideration.
- We also show that the upper-bound outage probability of a room can be calculated by the cumulative distribution function (CDF) of the UE location-specific LES and LEP in the medium and high SNR regimes, respectively.
- The effectiveness of the three proposed metrics is numerically evaluated under different room sizes and aspect ratios, wall permittivities and conductivities, wall thicknesses, and BS-wall distances, and is compared with respect to their advantages, limitations, and applicability.

The rest of the article is organized as follows. In Section II, we describe the system model for indoor LOS MIMO downlink transmissions taking the WRs from the BS's closest wall into account. In Section III, we derive the lower-bound channel capacity, LES and LEP for an arbitrary UE location in closed forms, based on which we propose three metrics for fast

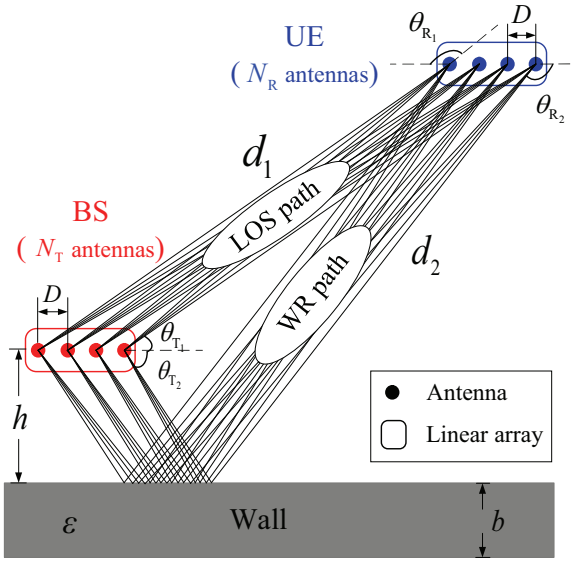

Fig. 1. MIMO channel model with both LOS path and WR path

wireless friendliness evaluation of the wall in Section IV. Numerical results are presented and discussed in Section V. Finally, we conclude this article in Section VI.

2 System Model

As shown in Fig. 1, we consider an indoor LOS MIMO downlink, where the BS is placed with a small distance of h m to its closest wall and one UE is arbitrarily positioned in the room. The BS and UE are each equipped with a uniform linear array (ULA) with the inter-antenna spacing of D m, consisting of N_{T} and N_{R} antennas, respectively. The ULAs at the BS and the UE are both assumed to be parallel to the wall closest to the BS. The received signal $\mathbf{y} \in \mathbb{C}^{N_{\mathrm{R}} \times 1}$ at an arbitrary UE location[1] is given by the transmitted signal $\mathbf{x} \in \mathbb{C}^{N_{\mathrm{T}} \times 1}$, the channel matrix $\mathbf{H} \in \mathbb{C}^{N_{\mathrm{R}} \times N_{\mathrm{T}}}$ and the additive white Gaussian noise $\mathbf{n}$ as

$$\mathbf{y} = \mathbf{H}\mathbf{x} + \mathbf{n}. \tag{1}$$

[1] In Sections II and III, we mainly study the lower-bound capacity of the channel between the BS and an arbitrary UE location. The variables denoting the UE location are dropped for brevity.

The multiple reflections inside the wall as a homogenous dielectric reflector can be modelled by the equivalent reflection coefficient, which is given by [21]

$$\Gamma = \frac{1-\exp(-j2\delta)}{1-\Gamma'^2\exp(-j2\delta)}\Gamma', \tag{2}$$

$$\delta = \frac{2\pi b}{\mu}\sqrt{\varepsilon - \sin^2\alpha}, \tag{3}$$

where α denotes the equivalent incident angle of reflections of all orders under far-field plane wave assumption, μ denotes the wavelength of the EM waves in the air, b denotes the thickness of the wall, ε denotes the relative permittivity of the wall and is given by $\varepsilon = \varepsilon_0 - j17.98\sigma/f$, where $\varepsilon_0 = uf^v$, $\sigma = rf^t$ is the conductivity of the wall material, f denotes the signal's frequency, and u, v, r and t are constant parameters given in [21, Table III], and Γ' denotes the first-order reflection coefficient, which is given by Γ_{TE} for the transverse electric (TE) polarisation or Γ_{TM} for the transverse magnetic (TM) polarisation of the incident electric field, respectively:

$$\Gamma_{\mathrm{TE}} = \frac{\cos\alpha - \sqrt{\varepsilon - \sin^2\alpha}}{\cos\alpha + \sqrt{\varepsilon - \sin^2\alpha}}, \tag{4}$$

$$\Gamma_{\mathrm{TM}} = \frac{\cos\alpha - \sqrt{(\varepsilon - \sin^2\alpha)/\varepsilon^2}}{\cos\alpha + \sqrt{(\varepsilon - \sin^2\alpha)/\varepsilon^2}}. \tag{5}$$

The wall-reflected EM waves propagating along the WR path will arrive at the UE receiver in addition to the EM waves along the LOS path. Based on Friis' formula, the channel matrix $\mathbf{H}$ at a specific UE location can be deterministically modelled as [26]

$$\mathbf{H} = A_1\mathbf{h}_{\beta_1}^{\mathrm{H}}\mathbf{h}_{\alpha_1} + A_2\mathbf{h}_{\beta_2}^{\mathrm{H}}\mathbf{h}_{\alpha_2}, \tag{6}$$

$$\alpha_l = \frac{2\pi}{\mu}D\cos\theta_{\mathrm{T}_l}, \beta_l = \frac{2\pi}{\mu}D\cos\theta_{\mathrm{R}_l},$$

$$A_1 = \frac{\mu}{4\pi d_1}e^{-j2\pi\frac{d_1}{\mu}}, A_2 = \frac{\mu\Gamma}{4\pi d_2}e^{-j2\pi\frac{d_2}{\mu}},$$

$$\mathbf{h}_{\alpha_l} = \left(e^{-j\left(-\frac{N_\mathrm{T}-1}{2}\right)\alpha_l}, e^{-j\left(1-\frac{N_\mathrm{T}-1}{2}\right)\alpha_l}, ..., e^{-j\left(\frac{N_\mathrm{T}-1}{2}\right)\alpha_l} \right),$$
$$\mathbf{h}_{\beta_l} = \left(e^{j\left(-\frac{N_\mathrm{R}-1}{2}\right)\beta_l}, e^{j\left(1-\frac{N_\mathrm{R}-1}{2}\right)\beta_l}, ..., e^{j\left(\frac{N_\mathrm{R}-1}{2}\right)\beta_l} \right),$$

where $l \in \{1,2\}$, $\{\cdot\}^\mathrm{H}$ represents the complex conjugate transpose of a vector or matrix, d_1 and d_2 denote the length of the LOS path and the WR path, respectively, θ_{T_1} and θ_{T_2} denote the equivalent angle of departure (AoD) of the LOS path and the WR path at the BS antenna array, respectively, θ_{R_1} and θ_{R_2} denote the equivalent angle of arrival (AoA) of the LOS path and the WR path at the UE antenna array, respectively, and Γ represents the equivalent reflection coefficient of the WR path given in (2)-(3). Since the rank of $\mathbf{H}$ is 2, matrix $\mathbf{H}\mathbf{H}^\mathrm{H}$ has only two eigenvalues.

3 Lower-bound Capacity

The MIMO channel capacity per unit bandwidth at a specific UE location is given by

$$\begin{aligned} C &= \log_2 \left(\left| I_{N_\mathrm{R}} + \frac{\rho}{N_\mathrm{T}} \mathbf{H}\mathbf{H}^\mathrm{H} \right| \right) \\ &= \log_2 \left(\left(1 + \frac{\rho}{N_\mathrm{T}} \lambda_1 \right) \left(1 + \frac{\rho}{N_\mathrm{T}} \lambda_2 \right) \right) \\ &= \log_2 \left(1 + \frac{\rho}{N_\mathrm{T}} (\lambda_1 + \lambda_2) + \frac{\rho^2}{N_\mathrm{T}^2} \lambda_1 \lambda_2 \right), \end{aligned} \tag{7}$$

where $\rho = \frac{P_\mathrm{T}}{N_0}$ is the BS transmit SNR, P_T and N_0 denote the power of the transmitted signal and noise, respectively, λ_1 and λ_2 denote the two eigenvalues of $\mathbf{H}\mathbf{H}^\mathrm{H}$.

Based on (7), in the medium SNR regime, i.e., $\rho < \frac{\lambda_1+\lambda_2}{\lambda_1\lambda_2} N_\mathrm{T}$, the MIMO channel capacity per unit bandwidth is lower bounded by

$$C_\mathrm{m} = \log_2 \left(\frac{\rho}{N_\mathrm{T}} (\lambda_1 + \lambda_2) \right) = \log_2 \frac{\rho}{N_\mathrm{T}} + \log_2 (\lambda_1 + \lambda_2), \tag{8}$$

where $\log_2 (\lambda_1 + \lambda_2)$ is referred to as LES.

In the high SNR regime, i.e., $\rho \geq \frac{\lambda_1+\lambda_2}{\lambda_1\lambda_2} N_{\mathrm{T}}$, the MIMO channel capacity per unit bandwidth is lower bounded by

$$C_{\mathrm{h}} = \log_2\left(\frac{\rho^2}{N_{\mathrm{T}}^2}\lambda_1\lambda_2\right) = 2\log_2\frac{\rho}{N_{\mathrm{T}}} + \log_2\left(\lambda_1\lambda_2\right), \tag{9}$$

where $\log_2\left(\lambda_1\lambda_2\right)$ is referred to as LEP.

Since $\log_2\frac{\rho}{N_{\mathrm{T}}}$ is a constant independent of the room setting or building materials, the LES and LEP can effectively characterise the wireless friendliness of a wall in the medium and high SNR regimes, respectively. Following [26, Lemma 1], the LES and LEP at a specific UE location are computed, respectively, by

$$\log_2(\lambda_1+\lambda_2) = \log_2\left(\frac{\mu^2 N_{\mathrm{T}} N_{\mathrm{R}}}{16\pi^2 d_1^2} + \frac{\mu^2|\Gamma|^2 N_{\mathrm{T}} N_{\mathrm{R}}}{16\pi^2 d_2^2} + \frac{\mu^2 N_{\mathrm{T}} N_{\mathrm{R}}}{8\pi^2 d_1 d_2}\Delta_\alpha\Delta_\beta\Re\left(\Gamma e^{j2\pi\frac{d_1-d_2}{\mu}}\right)\right) \tag{10}$$

$$\begin{aligned}\log_2(\lambda_1\lambda_2) = &\log_2\left(1+\Delta_\alpha^2 - \frac{2\Delta_\alpha}{N_{\mathrm{T}}}\sum\nolimits_{q=-\frac{N_{\mathrm{T}}-1}{2}}^{\frac{N_{\mathrm{T}}-1}{2}}\cos\left(q(\alpha_1-\alpha_2)\right)\right)\\ &+\log_2\left(1+\Delta_\beta^2 - \frac{2\Delta_\beta}{N_{\mathrm{R}}}\sum\nolimits_{q=-\frac{N_{\mathrm{R}}-1}{2}}^{\frac{N_{\mathrm{R}}-1}{2}}\cos\left(q(\beta_1-\beta_2)\right)\right)\\ &+\log_2\left(\frac{\mu^2|\Gamma|N_{\mathrm{T}}N_{\mathrm{R}}}{16\pi^2 d_1 d_2}\right)^2\end{aligned} \tag{11}$$

where $\Re(\cdot)$ denote the real part of a complex,

$$\Delta_\alpha = \frac{1}{N_{\mathrm{T}}}\sum\nolimits_{q=-\frac{N_{\mathrm{T}}-1}{2}}^{\frac{N_{\mathrm{T}}-1}{2}}\exp\left(jq(\alpha_1-\alpha_2)\right) = \frac{\sin\left(\pi N_{\mathrm{T}} D(\cos\theta_{\mathrm{T}_1}-\cos\theta_{\mathrm{T}_2})/\mu\right)}{N_{\mathrm{T}}\sin\left(\pi D(\cos\theta_{\mathrm{T}_1}-\cos\theta_{\mathrm{T}_2})/\mu\right)}, \tag{12}$$

$$\Delta_\beta = \frac{1}{N_{\mathrm{R}}}\sum\nolimits_{q=-\frac{N_{\mathrm{R}}-1}{2}}^{\frac{N_{\mathrm{R}}-1}{2}}\exp\left(jq(\beta_1-\beta_2)\right) = \frac{\sin\left(\pi N_{\mathrm{R}} D(\cos\theta_{\mathrm{R}_1}-\cos\theta_{\mathrm{R}_2})/\mu\right)}{N_{\mathrm{R}}\sin\left(\pi D(\cos\theta_{\mathrm{R}_1}-\cos\theta_{\mathrm{R}_2})/\mu\right)}. \tag{13}$$

Given that

$$\begin{aligned}\frac{1}{N_{\mathrm{T}}}\sum\nolimits_{q=-\frac{N_{\mathrm{T}}-1}{2}}^{\frac{N_{\mathrm{T}}-1}{2}}\cos\left(q(\alpha_1-\alpha_2)\right) &= \Delta_\alpha,\\ \frac{1}{N_{\mathrm{R}}}\sum\nolimits_{q=-\frac{N_{\mathrm{R}}-1}{2}}^{\frac{N_{\mathrm{R}}-1}{2}}\cos\left(q(\beta_1-\beta_2)\right) &= \Delta_\beta,\end{aligned}$$

we obtain a simple expression of the LEP at a specific UE location as follows

$$\log_2(\lambda_1\lambda_2)=2\log_2\left(\frac{\mu^2|\Gamma|N_{\mathrm{T}}N_{\mathrm{R}}}{16\pi^2 d_1 d_2}\right)+\log_2\left(1-\Delta_\alpha^2\right)\left(1-\Delta_\beta^2\right). \tag{14}$$

We note that the inter-antenna spacing D, the wall thickness b, the LOS path length d_1, and the WR path length d_2 can typically be given as multiples of the signal wavelength μ. Thus, according to (10, 12-14), for given EM parameters of a wall material (i.e., the relative permittivity and conductivity), the UE-specific LES and UE-specific LEP are not affected by the signal frequency.

We also find that the number of antennas, i.e., N_{T} and N_{R}, affects the values of UE-specific LES and UE-specific LEP, indicating that the MIMO configuration should be considered when evaluating a wall's wireless friendliness.

By substituting (10) and (14) into (8) and (9), respectively, the lower-bound MIMO channel capacity per unit bandwidth at a specific UE location in the medium and high SNR regimes are, respectively, given by

$$C_{\mathrm{m}}=\log_2\left(\frac{\mu^2\rho N_{\mathrm{R}}}{8\pi^2}\right)+\log_2\left(\frac{1}{2d_1^2}+\frac{\Re\left(\Gamma e^{j2\pi\frac{d_1-d_2}{\mu}}\right)}{(\Delta_\alpha\Delta_\beta)^{-1}d_1 d_2}+\frac{|\Gamma|^2}{2d_2^2}\right), \tag{15}$$

$$C_{\mathrm{h}}=2\log_2\left(\frac{\mu^2\rho N_{\mathrm{R}}}{16\pi^2}\right)+\log_2\left(\frac{|\Gamma|^2\left(1-\Delta_\alpha^2\right)\left(1-\Delta_\beta^2\right)}{d_1^2 d_2^2}\right). \tag{16}$$

4 Wireless Friendliness Evaluation for Walls as Reflectors

In this section, we design three new metrics: the spatially averaged LES, the spatially averaged LEP, and the upper-bound outage probability, which are all over the room of interest, to enable fast evaluation of the wireless friendliness of the wall closest to the BS.

The wireless friendliness of the wall closest to the BS can be evaluated based on the lower-bound capacity for all possible UE locations in a rectangular room [26]. As revealed in (8) and (9), the impact of the BS transmission power and that of the wall material properties on the lower-bound indoor capacity can be decoupled, which enables fast evaluation of the

wall's wireless friendliness based on the statistics of the LES and LEP at an arbitrary UE position in the room of interest.

We apply a 2D Cartesian coordinate system inside a rectangular room and evenly divide the room area into a $X \times Y$ dense grid. We can calculate the LES and LEP at the centre of each smallest rectangle (x_i, y_j), using (10) and (14), respectively, denoted by $\mathrm{LES}\left(x_i, y_j\right)$ and $\mathrm{LEP}\left(x_i, y_j\right)$, where $i \in \{1, 2, ..., X\}$ and $j \in \{1, 2, ..., Y\}$.

4.1 Spatially averaged LES and spatially averaged LEP of a room

The impact of room settings on the spatially averaged capacity over a room can be studied based on the spatially averaged LES and spatially averaged LEP of that room, which are computed by

$$\mathrm{LES}_{\mathrm{avg}} = \frac{1}{XY} \sum_{i=1}^{X} \sum_{j=1}^{Y} \mathrm{LES}\left(x_i, y_j\right). \tag{17}$$

$$\mathrm{LEP}_{\mathrm{avg}} = \frac{1}{XY} \sum_{i=1}^{X} \sum_{j=1}^{Y} \mathrm{LEP}\left(x_i, y_j\right). \tag{18}$$

However, due to the complicated expressions of the UE location-specific LES and LEP expression in (10) and (14), it is difficult to derive closed-form expressions for the spatially averaged LES and spatially averaged LEP of a room. Hence, the spatially averaged LES and spatially averaged LEP will be obtained numerically in Section V.

4.2 Upper-bound outage probability of a room

To evaluate the percentage of all possible UE locations not meeting the target downlink capacity, the upper-bound outage probability of a room is designed as another evaluation metric of the wireless friendliness of the wall. Under the channel (6) that considers both the LOS path and the WR path, a lower value of the upper-bound outage probability of a room means a better wireless signal coverage inside the room, which indicates that the wall is more wireless-friendly.

An outage occurs when the capacity at UE location $\left(x_i, y_j\right)$ falls below a given downlink capacity threshold T bit/s/Hz. The upper-bound outage probability of a room is defined to

measure the proportion of UE locations whose capacities are not greater than T bit/s/Hz, and is given by

$$\begin{aligned} P(T) &= \Pr\left(C^{'} \leq T\right) \\ &= \begin{cases} \Pr\left(\mathrm{LES}' \leq T - \log_2 \frac{\rho}{N_\mathrm{T}}\right), & \rho < \frac{\lambda_1+\lambda_2}{\lambda_1\lambda_2} N_\mathrm{T}, \\ \Pr\left(\mathrm{LEP}' \leq T - 2\log_2 \frac{\rho}{N_\mathrm{T}}\right), & \rho \geq \frac{\lambda_1+\lambda_2}{\lambda_1\lambda_2} N_\mathrm{T}. \end{cases} \end{aligned} \tag{19}$$

where $C^{'}$, LES$'$, and LEP$'$ are the variables denoting the lower-bound capacity, LES, and LEP at an arbitrary UE position in the room of interest, respectively. Therefore, the upper-bound outage probability of a room can be computed by the CDF of the LES in the medium SNR regime and by the CDF of the LEP in the high SNR regime. We note that the downlink capacity threshold T should be properly selected according to the MIMO configuration.

According to the above three proposed evaluation metrics, the wireless friendliness of the wall will be directly affected by the wall material's thickness and relative permittivity, and BS-wall distance, as they influence the reflection characteristics of the wall as a reflector. Besides, the size and aspect ratio of a rectangular room, which determines the transverse dimension of the wall closest to the BS, will also influence the wireless friendliness of the wall.

5 Numerical Results and Analysis

In this work, the simulation is performed in the 6 GHz band in a rectangular room with the dimension of $W \times L$ m^2. The BS is deployed on the centreline perpendicular to the L side. The incident EM wave is assumed to be TE polarised. The transmit power is assumed to be equally allocated to each BS antenna. The inter-antenna spacing of both the UE and BS antenna array are assumed to be half wavelength. The UE and BS antenna array each employ a 4-antenna ULA. We consider five popular wall materials, whose values of relative permittivity are given in Table. I following [21, Table III].

TABLE I Material EM parameters under 6 GHz [21]

Material class	ε_0	σ
Concrete	5.31	0.1390
Brick	3.75	0.0380
Plasterboard	2.94	0.0412
Wood	1.99	0.0321
Glass	6.27	0.0364

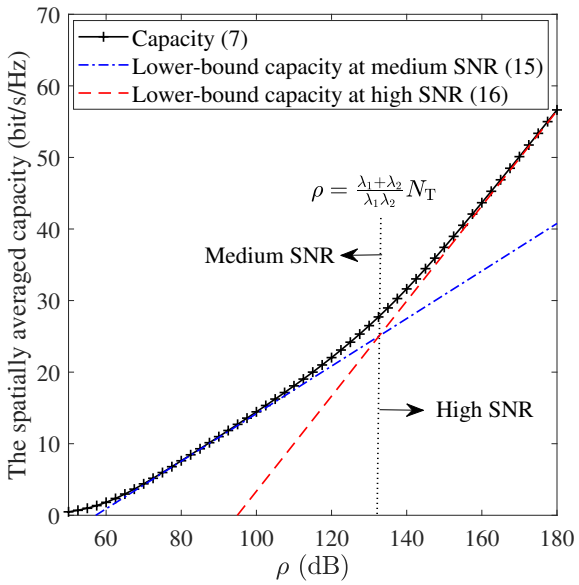

Fig. 2. The spatially averaged capacity of the room versus BS transmit SNR.

5.1 Verification of the analytical derivations

Fig. 2 plots the spatially averaged capacity in the 10×10 m^2 room versus the BS transmit SNR. The values of the spatially averaged capacity are computed by averaging over dense sample points inside the room with concrete walls of thickness 0.2 m and for the BS-wall distance of 0.05 m. We can see that the derived lower-bound capacity C_{m} in (15) and C_{h} in (16) are very close to the capacity C in (7) in the medium and high SNR regimes, respectively.

Fig. 3 plots the upper-bound outage probability versus the downlink capacity threshold T at medium SNR of $\rho = 90$ dB and high SNR of $\rho = 150$ dB inside the 10×10 m^2 room with concrete walls of thickness 0.2 m and the BS-wall distance of 0.05 m. It is observed that the upper-bound outage probability increases with the downlink capacity threshold.

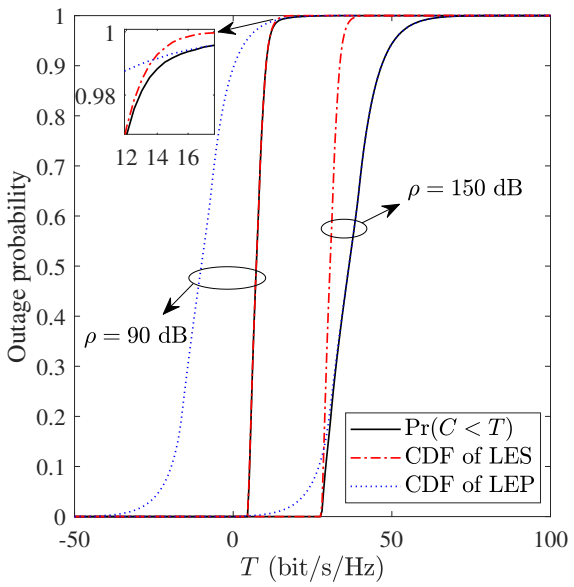

Fig. 3. The upper-bound outage probability of the room versus downlink capacity threshold T at medium SNR of $\rho = 90$ dB and high SNR of $\rho = 150$ dB.

Meanwhile, the CDF of the LES and the CDF of LEP tightly match the actual outage probability $\Pr(C < T)$ in the medium and high SNR regimes, respectively, as given in (19).

5.2 The impact of room settings on the spatially averaged LES and spatially averaged LEP of a room

In Fig. 4 and Fig. 5, we discuss the impact of room settings on the spatially averaged LES and spatially averaged LEP over the room of interest, respectively.

Fig. 4(a) and Fig. 5(a) plot the spatially averaged LES and spatially averaged LEP for different room sizes, respectively. The aspect ratio of a room is defined as $r = L/W$. The wall is assumed to be concrete with the thickness of 0.2 m and the BS-wall distance is 0.05 m. From Fig. 4(a) and Fig. 5(a), given the same aspect ratio of rooms, a larger room size results in a smaller spatially averaged LES and spatially averaged LEP due to the sever path loss caused by the longer LOS path and WR path.

Fig. 4(b) and Fig. 5(b) plot the spatially averaged LES and spatially averaged LEP for different aspect ratios, respectively. It is seen that, for the same room size, with the increase

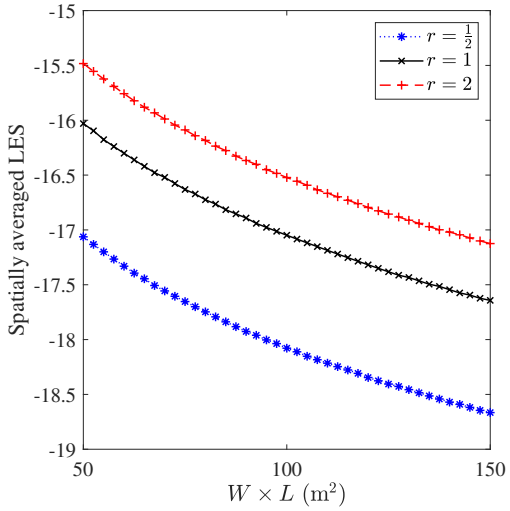

(a) Under various room sizes

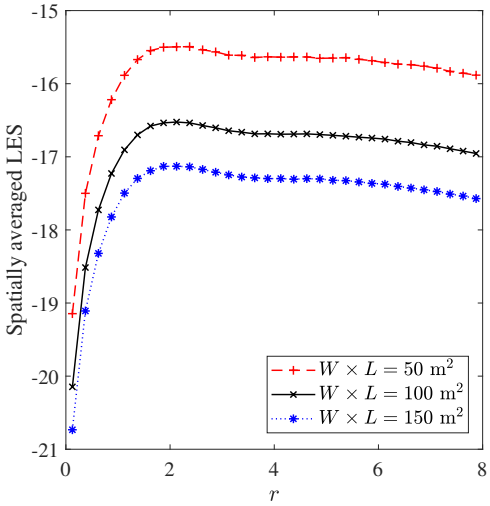

(b) Under various room aspect ratios

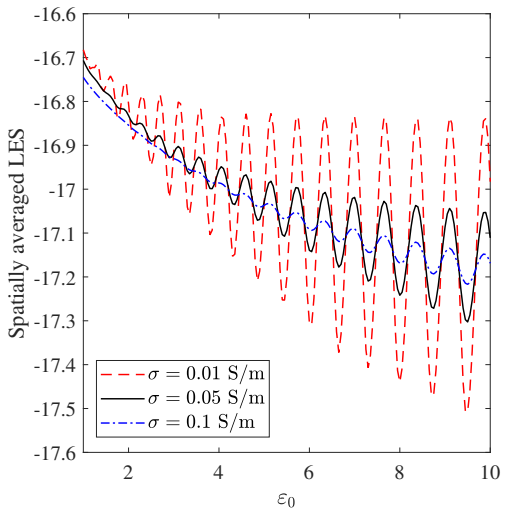

(c) Under various real part of wall relative permittivities

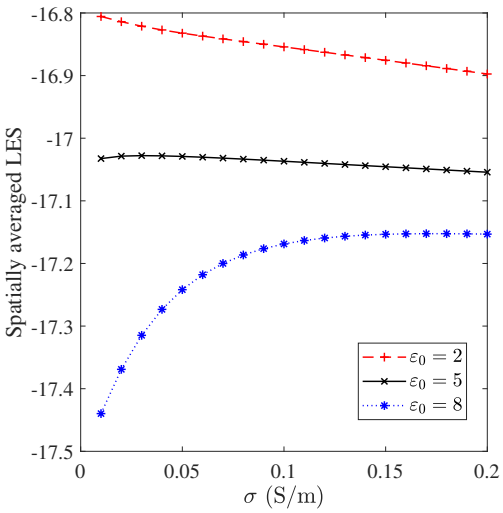

(d) Under various wall conductivities

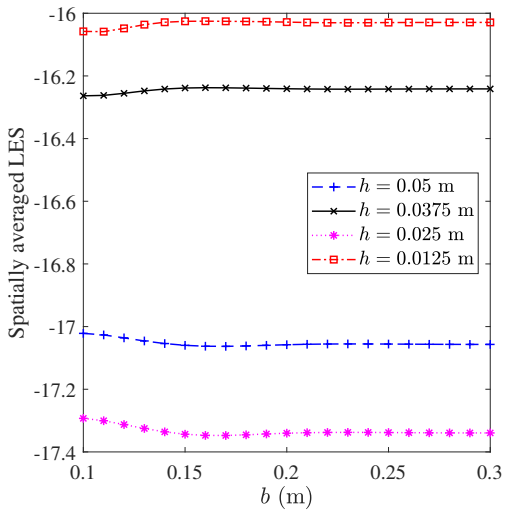

(e) Under various wall thickness

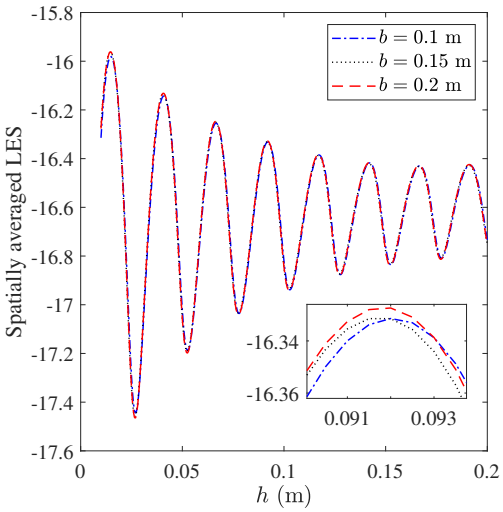

(f) Under various BS-wall distances

Fig. 4. The spatially averaged LES of a room in (10) under different room settings.

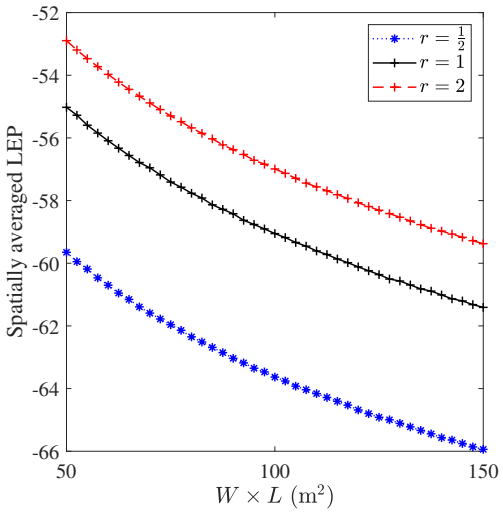

(a) Under various room sizes

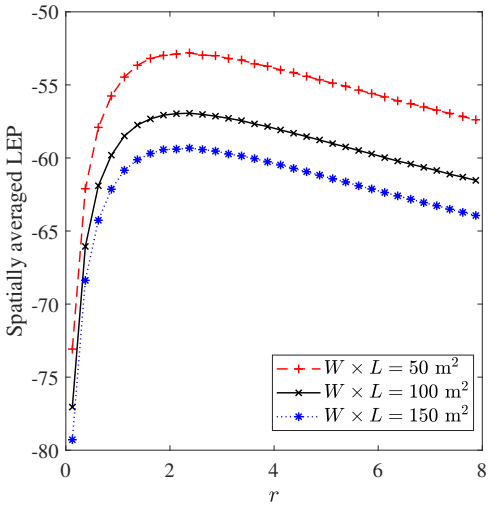

(b) Under various room aspect ratios

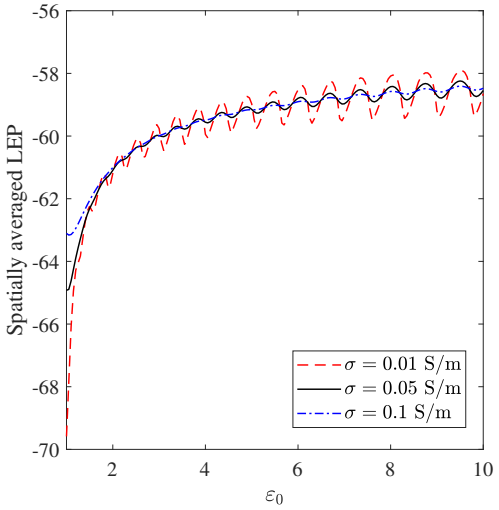

(c) Under various real part of wall relative permittivities

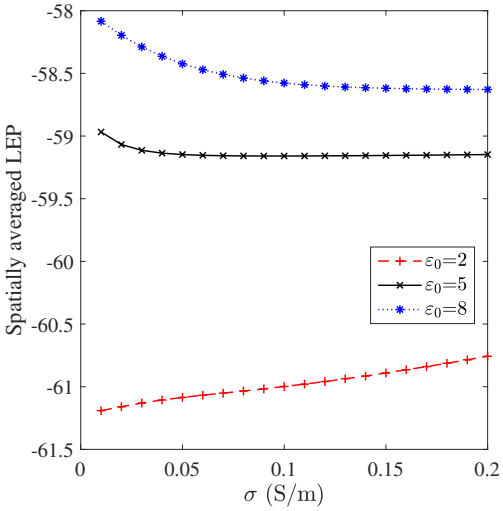

(d) Under various wall conductivities

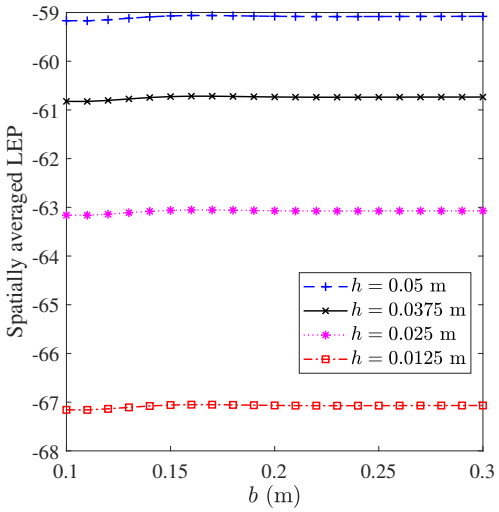

(e) Under various wall thickness

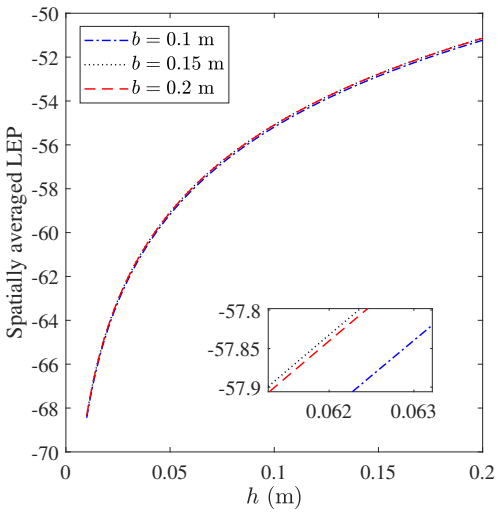

(f) Under various BS-wall distances

Fig. 5. The spatially averaged LEP of a room in (14) under different room settings.

of r from $\frac{1}{8}$ to 8, the spatially averaged LES and spatially averaged LEP first rapidly increase and then slowly decrease. The peak values of the spatially averaged LES and spatially averaged LEP are obtained when r approaches 2. This phenomenon can be explained by the path loss towards the UE location farthest from the BS, where the longest BS-UE distance in the room is approximately given by $d_{1,\max} = W\sqrt{1+\frac{1}{4}r^2} = \sqrt{\frac{S}{r}+\frac{Sr}{4}}$, where S is the give area of the rooms with different r. Obviously, as r is growing above 2, the path loss being approximately proportional to $d_{1,\max}^2$ will increase faster in growth rate since the derivative of $d_{1,\max}^2$ is greater than 0. We arrive at the conclusion that, for the same room size, the long side wall of a room with an aspect ratio close to 2, which is deployed closely behind the BS, would be more friendly to indoor LOS MIMO communications.

The spatially averaged LES and spatially averaged LEP of a room versus the real part of wall relative permittivity are depicted in Fig. 4(c) and Fig. 5(c), respectively, while the spatially averaged LES and spatially averaged LEP of a room versus the wall conductivity are depicted in Fig. 4(d) and Fig. 5(d), respectively, for a 10×10 m^2 room with the BS-wall distance of 0.05 m and the wall thickness of 0.2 m. We can see that the real part of wall relative permittivity determines the upward or downward trend of the spatially averaged LES and spatially averaged LEP, while the conductivity of wall materials affecting the imaginary part of the relative permittivity strongly influences the fluctuation magnitude and envelope. Generally, a severer fluctuation arises out of a smaller conductivity, and the spatially averaged LES is more prone to this fluctuation than the spatially averaged LEP. The above results reveal the significant impact of wall relative permittivity on indoor wireless capacity.

Fig. 4(e) and Fig. 5(e) illustrate the spatially averaged LES and spatially averaged LEP of a room under different wall thicknesses, respectively, for a 10×10 m^2 room with concrete walls and the BS-wall distance ranging from a quarter of wavelength (0.0125 m) to wavelength (0.05 m). We observe that, for a given BS-wall distance, both the spatially averaged LES and spatially averaged LEP change slightly with the wall thickness. This is because the wavelength of 0.05 m is not comparable to the typical wall thickness ranging from 0.1 m to 0.3 m. Meanwhile, the limited variation of δ in (3), caused by the narrow

range of typical wall thickness, hardly affects the equivalent reflection coefficient considering multiple internal reflections in (2).

Fig. 4(f) and Fig. 5(f) show the spatially averaged LES and spatially averaged LEP of a room under different BS-wall distances, respectively, for a 10×10 m^2 room with concrete walls ranging from 0.1 m to 0.2 m in thickness. It is found that the curves of spatially averaged LES fluctuate under a decreasing envelop with the increase of BS-wall distance from 0.01 m to 0.2 m. Nevertheless, the spatially averaged LEP present a monotonic increasing tendency with the rise of BS-wall distance. This is intuitive because, as the BS is moved away from its closest wall, the difference between the LOS path and the WR path becomes more substantial. Consequently, the two paths become more irrelevant, and the two eigenvalues of the channel becomes closer to each other. We can conclude that the BS deployment from its closest wall affects indoor wireless capacity.

5.3 The impact of room settings on the upper-bound outage probability of a room

In Fig. 6 and Fig. 7, we discuss the impact of room settings on the upper-bound outage probability of a room in the medium and high SNR regimes, respectively.

Fig. 6(a) and Fig. 7(a) present the upper-bound outage probability of a room at medium and high SNR, respectively, for different room sizes and aspect ratios with concrete walls of 0.2 m thickness and 0.05 m BS-wall distance. We can see that, for the rooms of same size with an aspect ratio no larger than 2, given a same downlink capacity threshold, the upper-bound outage probability of the room with a bigger aspect ratio would be smaller. The room with the aspect ratio of 4 does not obviously present a lower outage probability than the room of same size with the aspect ratio of 1.5625. Meanwhile, for the rooms with the aspect ratio of 1, given a same downlink capacity threshold, the upper-bound outage probability is smaller for the room of a smaller size than that of a bigger size. Therefore, the room size and aspect ratio will influence the outage performance over a room.

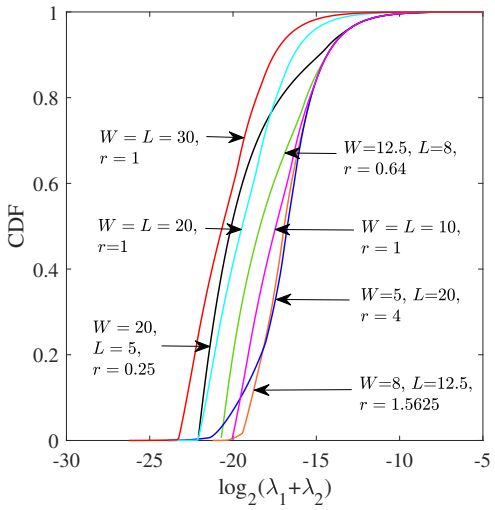

(a) Under various room sizes

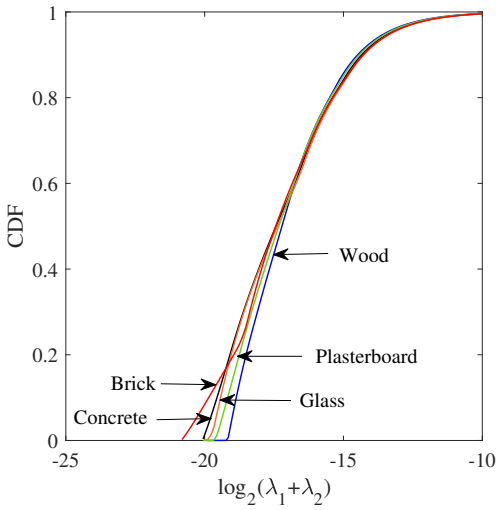

(b) Under various wall permittivities

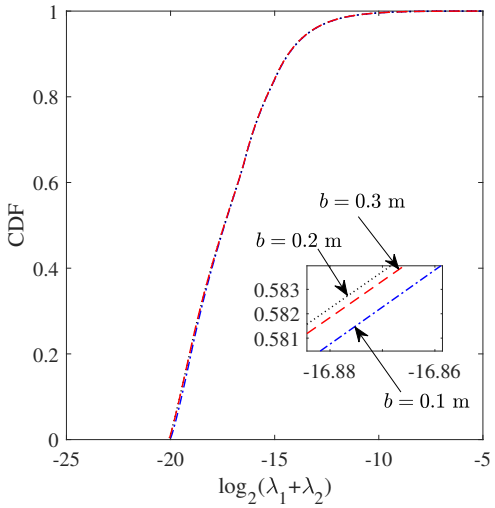

(c) Under various wall thicknesses

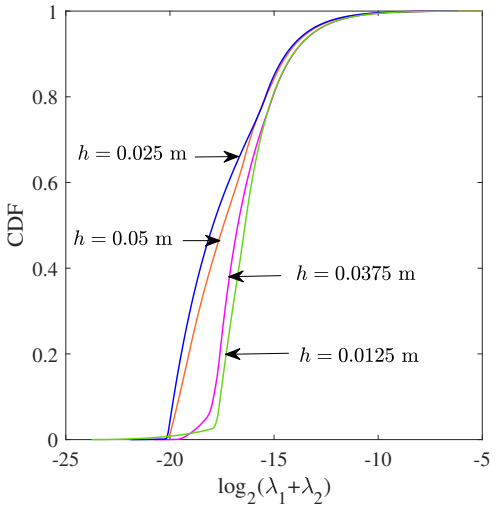

(d) Under various BS-wall distances

Fig. 6. The upper-bound outage probability of a room in (19) in the medium SNR regime under different room settings.

In Fig. 6(b) and Fig. 7(b), the upper-bound outage probability of a room at medium and high SNR are illustrated, respectively, for a 10×10 m^2 room with the BS-wall distance of 0.05 m under different wall materials with the thickness of 0.2 m. It is found that, at a high SNR, for a same downlink capacity threshold, the wall with a larger real part of relative permittivity would result in smaller upper-bound outage probability, which is verified by the curves order from left to right being wood with Re(ε) of 1.99, plasterboard with Re(ε) of 2.94, brick with Re(ε) of 3.75, concrete with Re(ε) of 5.31, and glass with Re(ε) of 6.27. The impact of imaginary part of the relative permittivity affected by the wall material's conductivity on the outage performance is much smaller than that of the real part of relative permittivity. However, the outage probability at medium SNR is irregular with the relative permittivity of these five materials due to the higher sensitivity of LES than LEP. In brief, the EM properties of wall materials need to be well selected in terms of the outage performance over a room.

The upper-bound outage probability of a room at medium and high SNR is shown in Fig. 6(c) and Fig. 7(c), respectively, under different wall thicknesses for a 10×10 m^2 room with concrete walls and the BS-wall distance of 0.05 m. We find that the curves of outage probability under the wall thickness of 0.1, 0.2, and 0.3 m are with very slight difference, indicating that the wall thickness in typical range does not substantially affect the outage performance over a room.

Fig. 6(d) and Fig. 7(d) depict the upper-bound outage probability of a room at medium and high SNR, respectively, under different BS-wall distances for a 10×10 m^2 room with concrete walls of 0.2 m in thickness. It is observed that, for a same downlink capacity threshold, the upper-bound outage probability at high SNR becomes smaller as the BS-wall distance increases from a quarter of wavelength (0.0125 m) to wavelength (0.05 m). Nonetheless, the curves of the upper-bound outage probability at medium SNR swing left and right with the change of every quarter of wavelength in BS-wall distance. This uncertainty of the trend can also be demonstrated by the fluctuations in Fig. 4(f). Hence, the BS-wall distance plays a crucial impact on the outage performance over a room.

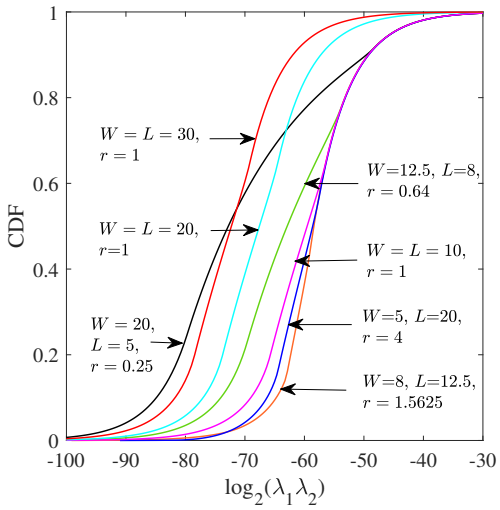

(a) Under various room sizes

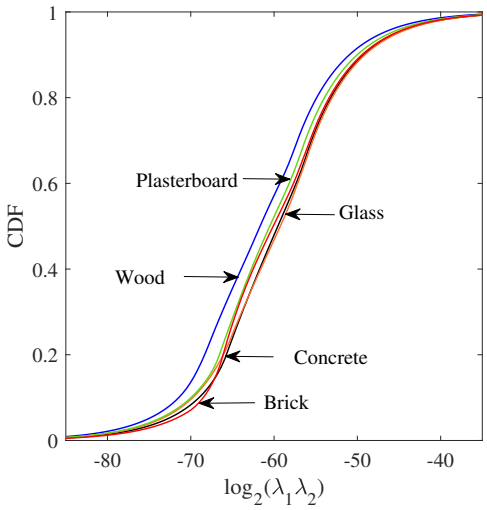

(b) Under various wall permittivities

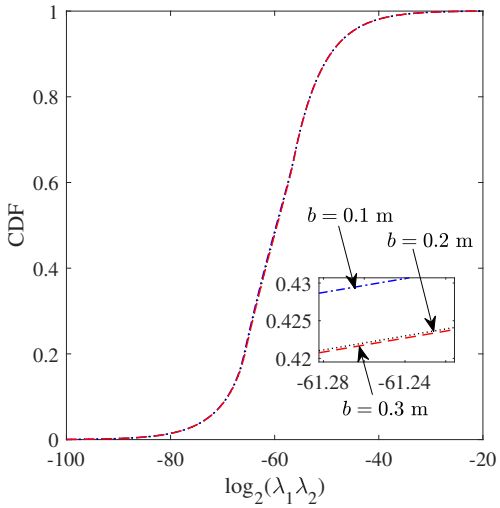

(c) Under various wall thicknesses

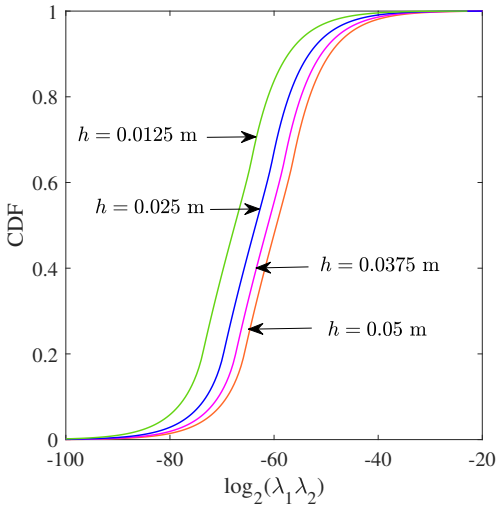

(d) Under various BS-wall distances

Fig. 7. The upper-bound outage probability of a room in (19) in the high SNR regime under different room settings.

5.4 Comparisons of the three proposed metrics

In this subsection, we compare the three proposed metrics for evaluating the wireless friendliness of a wall with respect to their advantages, limitations, and applicability. Note that the room setting factors mentioned below include the room size and aspect ratio, wall relative permittivity and thickness, and the BS-wall distance.

Given the spatially averaged LES and spatially averaged LEP of a room, respectively, the MIMO channel capacity in the medium and high SNR regimes can be easily obtained for a known BS transmit SNR. Meanwhile, according to the trend of the spatially averaged LES or spatially averaged LEP versus a room setting factor, the optimal configuration of this factor under medium and high SNR are thus attained. Moreover, the spatially averaged LES and spatially averaged LEP over the UE location are easy to get, which enables fast evaluation of the wireless friendliness of the wall as a reflector. However, it is analytically intractable to derive the expressions of spatially averaged LES and spatially averaged LEP, and it is uncertain if the obtained range of the room setting factor will meet the practical downlink capacity requirement, e.g., not less than the downlink capacity threshold T bit/s/Hz.

The upper-bound outage probability of a room, whose analytical expression is simple based on the CDF of the LES and LEP in the medium and high SNR regimes, respectively, can be leveraged to quickly evaluate the indoor capacity at any UE position against a given downlink capacity threshold and reveal the percentage of all possible UE locations not achieving the target downlink capacity. Nevertheless, the trends of upper-bound outage probability versus each room setting factor is not intuitive and is affected by the downlink capacity threshold. Besides, the downlink capacity threshold should be properly selected for the MIMO configuration of a given size.

In brief, the three proposed metrics have different applicability to the wireless friendliness evaluation of walls as reflectors. When evaluating the impact of a room setting factor on the indoor wireless capacity and obtaining its optimal configuration, the spatially averaged LES and spatially averaged LES of a room are preferred in the medium and high SNR regimes, respectively. When a room setting factor needs to be properly set to meet the capacity requirement, the upper-bound outage probability of a room should be adopted.

6 Conclusion

In this work, we have proposed three new metrics for fast evaluating the wireless friendliness of a wall that is close to an indoor BS based on how the wall reflections caused by it affect the lower-bound capacity. We have shown that the LES and LEP of the channel model that characterises both the LOS path and the WR path can represent the lower-bound capacity in the medium and high SNR regimes, respectively, and derived the LES, LEP, and the lower-bound capacity for an arbitrary UE location in closed forms. Three new metrics, i.e., the spatially averaged LES, spatially averaged LEP, and upper-bound outage probability of a room, have been proposed and compared with respect to their advantages, limitations, and applicability. Numerical results validate that the three proposed metrics are effective indicators of wireless friendliness of the wall as a reflector under different room sizes and aspect ratios, wall relative permittivities and thicknesses, and BS-wall distances. The measurement campaign will be held in the near future to validate the results herein using the experiment results.

References

[1] Cisco, *Cisco Visual Networking Index: Global Mobile Data Traffic Forecast Update, 2017-2022*, Feb. 2019. [Online]. Available: https://www.cisco.com/c/en/us/solutions/collateral/service-provider/visual-networkingindex-vni/white-paper-c11-738429.pdf

[2] L. Shi, *et al.*, "5G internet of radio light positioning system for indoor broadcasting service," *IEEE Trans. Broadcast.*, vol. 66, no. 2, pp. 534-544, Jun. 2020.

[3] N. Jawad, *et al.*, "Smart television services using NFV/SDN network management," *IEEE Trans. Broadcast.*, vol. 65, no. 2, pp. 404-413, Jun. 2019.

[4] J. Song, *et al.*, "An indoor broadband broadcasting system based on PLC and VLC," *IEEE Trans. Broadcast.*, vol. 61, no. 2, pp. 299-308, Jun. 2015.

[5] Ericsson, *Ericsson mobility report*, Jun. 2019. [Online]. Available: https://www.ericsson.com/en/mobility-report/reports/june-2019

[6] Huawei, *Mobile Video Report: China Trailblazing Mobile Live Video Market*, Feb. 2017. [Online]. Available: https://www-file.huawei.com/-/media/corporate/pdf/white%20paper/mobile-video-report-china-trailblazing-mobile-live-video-market-en-0314.pdf?la=en

[7] S. Yang and L. Hanzo, "Fifty years of MIMO detection: the road to large-scale MIMOs," *IEEE Commun. Surveys Tuts.*, vol. 17, no. 4, pp. 1941–1988, 4th Quart., 2015.

[8] B. Rohani, *et al.*, “Improving channel capacity in indoor 4×4 MIMO base station utilizing small bidirectional antenna," *IEEE Trans. Antennas Propag.*, vol. 66, no. 1, pp. 393-400, Jan. 2018.

[9] G. Li, *et al.*, “AMC-loaded wideband base station antenna for indoor access point in MIMO system," *IEEE Trans. Antennas Propag.*, vol. 63, no. 2, pp. 525-533, Feb. 2015.

[10] K. Haneda, *et al.*, “Indoor 5G 3GPP-like channel models for office and shopping mall environments,” *IEEE International Conference on Communications Workshops (ICC)*, Kuala Lumpur, 2016, pp. 694-699.

[11] S. K. Yoo, *et al.*, “Ceiling- or wall-mounted access points: an experimental evaluation for indoor millimeter wave communications,” *13th European Conference on Antennas and Propagation (EuCAP)*, Krakow, Poland, 2019, pp. 1-5.

[12] J. Zhang, A. A. Glazunov and J. Zhang, “Wireless energy efficiency evaluation for buildings under design based on analysis of interference gain,” *IEEE Trans. Veh. Tech.*, vol. 69, no. 6, pp. 6310–6324, Jun. 2020.

[13] J. Zhang, A. A. Glazunov and J. Zhang, “Wireless performance evaluation of building layouts: closed-form computation of figures of merit,” *IEEE Trans. Commun.*, vol. 69, no. 7, pp. 4890-4906, Jul. 2021.

[14] W. Yang, *et al.*, “Line-of-sight probability for channel modeling in 3-D indoor environments," *IEEE Antennas Wireless Propag. Lett.*, vol. 19, no. 7, pp. 1182-1186, Jul. 2020.

[15] Suherman, Fahmi, *et al.*, “Radio-friendly building for efficient signal distribution,” *IEEE International Conference on Communication, Networks and Satellite (Comnetsat)*, Medan, Indonesia, 2018, pp. 60-63.

[16] G. Narimani, P. A. Martin and D. P. Taylor, “Analysis of ultra wideband pulse distortion due to lossy dielectric walls and indoor channel models,” *IEEE Trans. Antennas Propag.*, vol. 64, no. 10, pp. 4423-4433, Oct. 2016.

[17] Y. Z. Goh, *et al.*, "Effects of complex wall structures on antenna radiation characteristics," *IEEE International Symposium on Antennas and Propagation & USNC/URSI National Radio Science Meeting*, Boston, MA, 2018, pp. 2485-2486.

[18] Y. Zhang, *et al.*, "Effects of wall reflection on the per-antenna power distribution of ZF-precoded ULA for indoor mmWave MU-MIMO transmissions," *IEEE Commun. Lett.*, vol. 25, no. 1, Jan. 2021.

[19] J. Zhang, *et al.*, "Two-ray reflection resolution algorithm for planar material electromagnetic property measurement at the millimeter-wave bands," *Radio Science*, vol. 55, pp. 3, Mar. 2020.

[20] Y. Azar, H. Zhao and M. E. Knox, "Polarization diversity measurements at 5.8 GHz for penetration loss and reflectivity of common building materials in an indoor environment," *Third International Conference on Future Generation Communication Technologies (FGCT)*, Luton, 2014.

[21] ITU-R, "Effects of building materials and structures on radiowave propagation above about 100 MHz P series radiowave propagation," *Recomm. ITU-R P.2040-1*, Jul. 2015.

[22] O. Landron, M. J. Feuerstein, and T. S. Rappaport, "A comparison of theoretical and empirical reflection coefficients for typical exterior wall surfaces in a mobile radio environment," *IEEE Trans. Antennas Propag.*, vol. 44, no. 3, pp. 341-351, Mar. 1996.

[23] N. Yu, P. Genevet, M. A. Kats, F. Aieta, J.-P. Tetienne, F. Capasso, and Z. Gaburro, "Light propagation with phase discontinuities: Generalized laws of reflection and refraction," *Science*, vol. 334, no. 6054, pp. 333-337, Oct. 2011.

[24] L. Subrt, *et al.*, "Advanced modelling of intelligent walls for indoor smart environments," *The 8th European Conference on Antennas and Propagation (EuCAP 2014)*, The Hague, 2014, pp. 620-622.

[25] L. Subrt and P. Pechac, "Controlling propagation environments using intelligent walls," *6th European Conference on Antennas and Propagation (EUCAP)*, Prague, 2012, pp. 1-5.

[26] Y. Zhang, *et al.*, "How friendly are building materials as reflectors to indoor LOS MIMO communications?," *IEEE Internet Things J.*, vol. 7, no. 9, pp. 9116-9127, Sept. 2020.

[27] A. Goldsmith, *Wireless Communications*. Cambridge, U.K.: Cambridge Univ. Press, 2005.

[28] D. Hoesli, Y. Kim and A. Lapidoth, "Monotonicity results for coherent MIMO Rician channels," *IEEE Trans. Inf. Theory*, vol. 51, no. 12, pp. 4334-4339, Dec. 2005.

Paper III

Effects of Wall Reflection on the Per-Antenna Power Distribution of ZF-Precoded ULA

Yixin Zhang, Jiliang Zhang, Xiaoli Chu, and Jie Zhang.

Published in *IEEE Communications Letters, Volume: 25, Issue: 1, Pages: 13-17, Jan. 2021.* Date of Publication: 09 Sep. 2020.

Effects of Wall Reflection on the Per-Antenna Power Distribution of ZF-Precoded ULA

Yixin Zhang[1], Jiliang Zhang[1], Xiaoli Chu[1], Jie Zhang[1,2]

[1] Department of Electronic and Electrical Engineering, the University of Sheffield, Sheffield, S10 2TN, UK

[2] Research and Development Department, Ranplan Wireless Network Design Ltd., Cambridge, CB23 3UY, UK

Abstract

Indoor access points (APs) with large-scale antenna arrays would commonly be deployed in the vicinity of a wall, where wall reflection (WR) affects the indoor electromagnetic (EM) wave propagation. In this paper, we investigate the effects of WR on the per-antenna power distribution of a transmit uniform linear array (ULA) adopting a zero-forcing (ZF) precoder. A new channel model is constructed to characterise the impact of both the line-of-sight (LOS) path and the WR path on indoor millimetre wave (mmWave) multi-user (MU) multiple-input multiple-output (MIMO) downlink transmissions. Specifically for the dual user equipment (UE) scenario, the ZF precoding matrix is analytically obtained and verified through simulations. The effects of WR on the per-antenna power distribution of the ZF-precoded ULA, in terms of the normalized power distribution and maximum power ratio (MPR), are evaluated through the comparisons between our proposed channel model and the pure LOS channel model. Our analytical and numerical results reveal the impact of AP configurations (the number of antennas and the AP-wall distance), multi-user spatial distribution (the angle of departure (AoD) and length of the LOS path for each user), and wall parameters (permittivity and thickness) on the power distribution across the ZF-precoded ULA. It is found that the effects of WR will exacerbate the uneven power distribution across the ZF-precoded ULA.

1 Introduction

The combination of multiple-input multiple-output (MIMO) and millimetre wave (mmWave) technologies facilitates massive indoor high-rate wireless applications for future wireless networks by exploiting spatial multiplexing gains even in limited scattering environment [1–5]. While the deployment of indoor access point(s) (AP) would typically be optimised to maximise the throughput and/or coverage [6], customers may prefer to deploy the APs in positions that will not lead to inconveniencing usages of a room. A popular solution is to integrate the AP with an interior wall of the building [7]. In this sense, the interactions between the indoor electromagnetic wave (EM) propagation and the interior wall should not be neglected in the deployment of indoor APs [8, 9].

The EM wave bounced off an interior wall would have experienced multiple internal reflections, whose amplitudes and phases are totally changed [10]. The wall reflection (WR) is characterised by the reflection coefficient, which depends on the EM wave's polarisation, incidence angle, and the wall material's relative permittivity and thickness [11]. Measurement campaigns in the 28 GHz band show that typical indoor building materials such as clear glass and dry wall usually have strong reflectivity and low penetration [12]. Hence, it is necessary to consider the effects of WR when evaluating indoor wireless performance.

In downlink multi-user (MU) MIMO scenarios, zero-forcing (ZF) precoding has been widely used to suppress inter-user interference. However, the power distribution across a ZF-precoded transmit antenna array has not been sufficiently studied. The power assigned to each transmit antenna affects the efficiency of its corresponding RF power amplifier, and thus influences the power consumption of the RF chains of the AP[13]. It has been shown that the uniform power excitation over all transmit antennas would allow the RF power amplifiers to work with maximum efficiency [14, 15], while significant power variations across different antennas would reduce this efficiency and cause a huge waste of energy. That is why per-antenna power constraints, instead of sum power constraints, need to be well considered for practical precoder design [16].

In this paper, we study the impact of WR on the per-antenna power distribution across the precoded antenna array for indoor mmWave MU-MIMO downlink transmissions. The

transmitter is assumed to be equipped with a ZF-precoded uniform linear array (ULA) for analytical tractability. The contribution of this paper is summarised as follows:

- To capture the effects of WR on the power distribution across the precoded ULA, a new channel model characterising both the line-of-sight (LOS) path and the WR path is proposed for indoor MU-MIMO downlink scenarios.
- We evaluate the effects of WR on the power distribution across the ZF-precoded ULA that serves multiple user equipment (UE) simultaneously through the comparisons between our proposed channel model and the pure LOS channel model in [15]. The unevenness in the power distribution across the ZF-precoded ULA becomes more significant under the effects of WR.
- We analytically derive the entries of the ZF precoding matrix for a dual-UE case, the accuracy of which is verified by simulation results.
- Our numerical results give insights into how the configuration of transmit antenna array, the spatial distribution of multiple users, the EM and physical properties of the wall, and the mutual coupling influence the power distribution across the ZF-precoded ULA.

2 System Model

In this work, we consider an indoor MU-MIMO downlink narrowband system in a LOS environment, as shown in Fig. 1(a). The AP, outfitted with a ULA of M directional antennas, is deployed in parallel with a wall with a distance of D_1 m from the wall. The impact of the directional radiation pattern of an AP antenna on the LOS path and the WR path is illustrated in Fig. 1(b). All the K single-antenna UEs locate in the far-field of the AP's ULA. Due to the dynamic attitude of UEs, the UE antenna is assumed as an omnidirectional antenna for analytical tractability. The transmit ULA is assumed to be transparent, i.e., it will not block the WRs to the UEs.

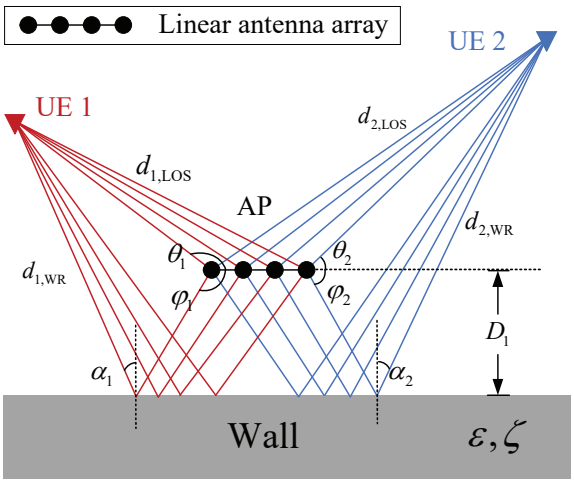

(a) The LOS path and the WR path between indoor BS and UE

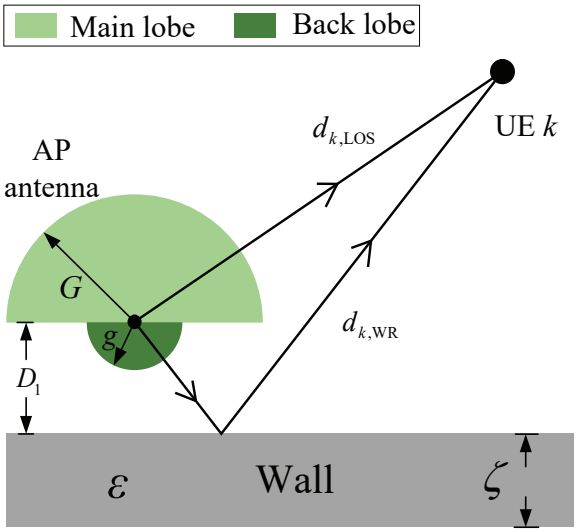

(b) The directional radiation pattern of an AP antennas

Fig. 1. Indoor MU-MIMO system model for a LOS environment.

In order to study the effects of WR on the per-antenna power distribution across the ULA, we incorporate the WR path to characterise the EM wave propagation inside a wall. The signal along the WR path experiences multiple reflections inside the wall closest to the AP, named as the considered wall hereafter. Using Friis' formula, the wireless link between the mth antenna and the kth UE is deterministically modelled as

$$\begin{aligned} h_{k,m} \propto\ & G d_{k,\mathrm{LOS}}^{-1} \exp\left(-j\beta\left(d_{k,\mathrm{LOS}} + (m - \frac{M+1}{2}) D \cos\theta_k\right)\right) \\ & + g\Gamma_k d_{k,\mathrm{WR}}^{-1} \exp\left(-j\beta\left(d_{k,\mathrm{WR}} + (m - \frac{M+1}{2}) D \cos\varphi_k\right)\right), \end{aligned} \tag{1}$$

where $\propto$ denotes being proportional to, $m \in \{1,2,...,M\}$, $k \in \{1,2,...,K\}$, G and g denote the main-lobe gain and side-lobe gain of each antenna, respectively, subject to $G^2 + g^2 = 2$ according to energy conservation law, $d_{k,\mathrm{LOS}}$ and $d_{k,\mathrm{WR}}$ denote the length of the LOS path and the WR path of the kth UE, respectively, θ_k and φ_k denote the angle of departure (AOD) of the LOS path and the WR path of the kth UE, respectively, $\beta = \frac{2\pi}{\lambda}$ denotes the wave number with λ being the wavelength, D denotes the inter-antenna spacing, and Γ_k denotes the kth UE's equivalent reflection coefficient of multiple internal reflections along the WR path and is defined in the following.

Supposing that the considered wall is a homogenous dielectric reflector, the multiple internal reflections inside it are strongly affected by the first-order reflection. In this letter, we mainly focus on the transverse electric (TE) polarisation of the incident EM waves. The proposed approach can be directly applied for the transverse magnetic (TM) polarisation. The first-order reflection coefficient for UE k is given by [11]

$$\bar{\Gamma}_k = \frac{\cos\alpha_k - \sqrt{\varepsilon - \sin^2\alpha_k}}{\cos\alpha_k + \sqrt{\varepsilon - \sin^2\alpha_k}} \tag{2}$$

with $\alpha_k = (\frac{\pi}{2} - \varphi_k)$ denoting the equivalent incident angle under plane wave assumption and ε denoting the relative permittivity of the considered wall. Given the thickness of the considered wall as ζ, the equivalent coefficient of multiple internal reflections for UE k is given by

$$\Gamma_k = \frac{1 - \exp(-j2\tau_k)}{1 - \bar{\Gamma}_k^2 \exp(-j2\tau_k)} \bar{\Gamma}_k, \tag{3}$$

where $\tau_k = \frac{2\pi\zeta}{\lambda}\sqrt{\varepsilon - \sin^2\alpha_k}$.

After precoding at the ULA and propagating through a complex flat-fading channel, the received signals at the UE sides are given by

$$\mathbf{y} = \mathbf{HCWs} + \mathbf{n}, \tag{4}$$

where $\mathbf{y}, \mathbf{s}, \mathbf{n} \in \mathbb{C}^{K\times 1}$ denote the received signal vector, data symbol vector and additive white Gaussian noise vector, respectively, $\mathbf{H} \in \mathbb{C}^{K\times M}$ denotes the channel matrix whose

elements are given in (1), $\mathbf{W} \in \mathbb{C}^{M\times K}$ denotes the precoding matrix, and $\mathbf{C} \in \mathbb{C}^{M\times M}$ denotes the mutual coupling matrix whose elements reveal how the radiated power of an antenna is affected by its neighbouring antennas [17].

In this letter, we employ the following empirical model of mutual coupling [18]

$$C_{p,q} = \exp\left(-\frac{2d_{p,q}}{\lambda}(\gamma + j\pi)\right), p \neq q \in \{1,2,...,M\}, \tag{5}$$

$$C_{p,p} = 1 - \frac{1}{M}\sum_{p=1}^{M}\sum_{q=1,q\neq p}^{M} C_{p,q},$$

where $C_{p,q}$ and $d_{p,q}$, respectively, denote the mutual coupling coefficient and distance between the pth antenna and qth antenna, and γ is a positive parameter controlling the mutual coupling level.

3 Effects of Wall Reflection on the Power Distribution of ZF-Precoded ULA

In this section, we investigate how the power is distributed among the M antennas of a ZF-precoded ULA serving K UEs simultaneously. We first apply two metrics to evaluate the power distribution across the transmit precoded ULA for an arbitrary K and then derive the analytical expression of the ZF precoding matrix for a dual-UE case, i.e. $K = 2$.

3.1 Metrics for quantifying power variation

Considering uncorrelated and unit variance data symbol sequences $\mathbf{x} = \sum_{k=1}^{K} \mathbf{w}_k s_k$, the transmitted power of the AP's ULA is given by $\mathrm{E}(|\mathbf{x}|^2) = \sum_{k=1}^{K} \|\mathbf{w}_k\|^2$, where $\mathbf{w}_k$ and s_k are the M-by-1 precoding vector and the intended symbol for the kth UE, respectively, $\mathrm{E}(\cdot)$ denotes the expectation, and $\|\cdot\|^2$ denotes the F-norm. Since the transmitted power is the summation of the F-norm of each UE's precoding vector, the power distribution across the AP's ULA can be evaluated based on each UE's precoding vector. Following [15], we apply the two metrics below to evaluate the power imbalance among the transmit antennas.

The normalized power allocated to the mth antenna to serve the kth UE is defined as

$$P_{k,m}^{\text{norm}} = \frac{\left|w_{k,m}\right|^2}{\left\|\mathbf{w}_k\right\|^2} = \frac{\left|w_{k,m}\right|^2}{\sum_{m=1}^{M}\left|w_{k,m}\right|^2}, \tag{6}$$

where $w_{k,m}$ is the mth element of $\mathbf{w}_k$.

Maximum power ratio (MPR) describing the power variation across the M antennas of a transmit ULA is defined as

$$P_k \triangleq \frac{\max\left(\mathbf{P}_k^{\text{norm}}\right)}{\min\left(\mathbf{P}_k^{\text{norm}}\right)}, \tag{7}$$

where $\mathbf{P}_k^{\text{norm}} = (P_{k,1}^{\text{norm}}, ..., P_{k,M}^{\text{norm}})$ gives the normalized power levels allocated to the M antennas for serving UE k.

3.2 Analytical ZF precoding matrix for a dual-UE case

The array factors (AFs) of the ULA are introduced as

$$\text{AF}_{ll} = \frac{\sin\left(M\beta D\delta_{ll}/2\right)}{\sin\left(\beta D\delta_{ll}/2\right)}, \tag{8}$$

$$\text{AF}_{lk,n} = \frac{\sin\left(M\beta D\delta_{lk,n}/2\right)}{\sin\left(\beta D\delta_{lk,n}/2\right)}, \tag{9}$$

where $k \neq l \in \{1,2\}$ denotes the UE index, $\delta_{ll} = \cos\theta_l - \cos\varphi_l$, $n \in \{3,4,5,6\}$, $\delta_{lk,3} = \cos\theta_k - \cos\theta_l$, $\delta_{lk,4} = \cos\varphi_k - \cos\theta_l$, $\delta_{lk,5} = \cos\theta_k - \cos\varphi_l$, and $\delta_{lk,6} = \cos\varphi_k - \cos\varphi_l$. Note that $\text{AF}_{lk,n} = \text{AF}_{kl,n}^*$, in which $\{\cdot\}^*$ denotes the complex conjugate.

Given (4), the effective downlink channel model is given by $\bar{\mathbf{H}} = \mathbf{HC}$. Even though $\mathbf{C}$ in (5) is a Toeplitz symmetrical matrix, the closed-form expression of $\mathbf{W}$ is still intractable. Fortunately, as stated in [19], the mutual coupling is non-negligible only when D is below 0.2λ. In this letter, D is assumed to be half wavelength to guarantee a low spatial correlation [20]. As such, both $\mathbf{C} \approx \mathbf{I}$ and $\bar{\mathbf{H}} \approx \mathbf{H}$ are satisfied, especially when $\gamma \geq 4$.

When $\gamma \geq 4$, the ZF precoding matrix is derived as [21]

$$\mathbf{W}=\mathbf{H}^{\mathrm{H}}\left(\mathbf{H}\mathbf{H}^{\mathrm{H}}\right)^{-1}\propto\mathbf{H}^{\mathrm{H}}\begin{bmatrix}\left(\mathbf{H}\mathbf{H}^{\mathrm{H}}\right)_{22} & -\left(\mathbf{H}\mathbf{H}^{\mathrm{H}}\right)_{12}\\ -\left(\mathbf{H}\mathbf{H}^{\mathrm{H}}\right)_{21} & \left(\mathbf{H}\mathbf{H}^{\mathrm{H}}\right)_{11}\end{bmatrix}, \tag{10}$$

where $\{\cdot\}^{\mathrm{H}}$ represents the complex conjugate transpose of a matrix. The four elements of matrix $\mathbf{H}\mathbf{H}^{\mathrm{H}}$ are given by

$$\left[\mathbf{H}\mathbf{H}^{\mathrm{H}}\right]_{11}=M(G^2d_{1,\mathrm{LOS}}^{-2}+g^2d_{1,\mathrm{WR}}^{-2}|\Gamma_1|^2)+2Ggd_{1,\mathrm{WR}}^{-1}d_{1,\mathrm{LOS}}^{-1}\mathrm{Re}\left(\Gamma_1F_1\right), \tag{11}$$

$$\left[\mathbf{H}\mathbf{H}^{\mathrm{H}}\right]_{22}=M(G^2d_{2,\mathrm{LOS}}^{-2}+g^2d_{2,\mathrm{WR}}^{-2}|\Gamma_2|^2)+2Ggd_{2,\mathrm{WR}}^{-1}d_{2,\mathrm{LOS}}^{-1}\mathrm{Re}\left(\Gamma_2F_2\right), \tag{12}$$

$$\begin{aligned}\left[\mathbf{H}\mathbf{H}^{\mathrm{H}}\right]_{12}&=G^2d_{2,\mathrm{LOS}}^{-1}d_{1,\mathrm{LOS}}^{-1}F_{12,3}+Ggd_{2,\mathrm{LOS}}^{-1}d_{1,\mathrm{WR}}^{-1}\Gamma_1F_{12,4}\\&\quad+Ggd_{1,\mathrm{LOS}}^{-1}d_{2,\mathrm{WR}}^{-1}\Gamma_2^*F_{12,5}+g^2d_{1,\mathrm{WR}}^{-1}d_{2,\mathrm{WR}}^{-1}\Gamma_1\Gamma_2^*F_{12,6},\end{aligned} \tag{13}$$

$$\begin{aligned}\left[\mathbf{H}\mathbf{H}^{\mathrm{H}}\right]_{21}&=G^2d_{2,\mathrm{LOS}}^{-1}d_{1,\mathrm{LOS}}^{-1}F_{21,3}+Ggd_{2,\mathrm{LOS}}^{-1}d_{1,\mathrm{WR}}^{-1}\Gamma_1^*F_{21,4}\\&\quad+Ggd_{1,\mathrm{LOS}}^{-1}d_{2,\mathrm{WR}}^{-1}\Gamma_2F_{21,5}+g^2d_{1,\mathrm{WR}}^{-1}d_{2,\mathrm{WR}}^{-1}\Gamma_1^*\Gamma_2F_{21,6},\end{aligned} \tag{14}$$

where

$$\begin{aligned}F_l&=\exp\left(j\beta\left(d_{l,\mathrm{LOS}}-d_{l,\mathrm{WR}}\right)\right)\mathrm{AF}_{ll},l\in\{1,2\},\\F_{21,3}&=\exp\left(j\beta\left(d_{1,\mathrm{LOS}}-d_{2,\mathrm{LOS}}\right)\right)\mathrm{AF}_{21,3},\\F_{21,4}&=\exp\left(j\beta\left(d_{1,\mathrm{WR}}-d_{2,\mathrm{LOS}}\right)\right)\mathrm{AF}_{21,4},\\F_{21,5}&=\exp\left(j\beta\left(d_{1,\mathrm{LOS}}-d_{2,\mathrm{WR}}\right)\right)\mathrm{AF}_{21,5},\\F_{21,6}&=\exp\left(j\beta\left(d_{1,\mathrm{WR}}-d_{2,\mathrm{WR}}\right)\right)\mathrm{AF}_{21,6}.\end{aligned}$$

Note that $F_{lk,n}=F_{kl,n}^*$ for $n\in\{3,4,5,6\}$ and $k\neq l\in\{1,2\}$.

By substituting (11)-(14) into (10), the precoding coefficient for the mth antenna to serve the kth UE is derived as

$$w_{k,m}\propto h_{k,m}^*\left(\mathbf{H}\mathbf{H}^{\mathrm{H}}\right)_{ll}-h_{l,m}^*\left(\mathbf{H}\mathbf{H}^{\mathrm{H}}\right)_{lk},k\neq l\in\{1,2\}. \tag{15}$$

When $\gamma<4$, since the analytical expression of $\mathbf{W}$ is not tractable, we analyse the proposed metrics using simulations.

4 Numerical Results

In order to study how WR affects the power distribution across the ZF-precoded ULA in the case of the AP being deployed close to the considered wall, we compare our proposed channel model in (1)-(3) with the LOS channel model in [15], which is given as

$$h'_{k,m} \propto d_{k,\mathrm{LOS}}^{-1} \exp\left(-j\beta\left(d_{k,\mathrm{LOS}} + (m - \tfrac{M+1}{2})D\cos\theta_k\right)\right)$$

for $m \in \{1,2,...,M\}$ and $k \in \{1,2,...,K\}$. As the channel model in [15] considers only the LOS path without the WR path, it is referred to as the pure LOS case. The normalized power $P_{k,m}^{\mathrm{norm}}$ and MPR P_k, given in (6) and (7) respectively, are taken as metrics for the comparison.

The simulation is carried out at 28 GHz. The inter-antenna spacing of the ULA is half wavelength. The main-lobe gain and side-lobe gain of the radiation pattern is assumed as $G = \sqrt{5/3}$ and $g = \sqrt{1/3}$, respectively. The incident EM wave impinging on the wall surface is assumed to be TE polarised. All the antennas of the AP and UEs are assumed to be vertically polarised (that is, there is no polarisation mismatch). The location of UE k is specified with the length and the AOD of its LOS path from the AP, i.e. $d_{k,\mathrm{LOS}}$ and θ_k. Note that the relative permittivity of a wall material is a complex value, whose real part and imaginary part are functions of the carrier frequency, respectively [11]. The following simulation results can verify the analytical derivations in Section III-B.

Fig. 2(a) plots the normalized power distribution across the ZF-precoded ULA with or without considering WR for the dual-UE case, for the number of antennas being 8, 16, or 32. We can see that the normalized power distribution presents a periodic behaviour across the antennas when considering only the LOS path. However, the vibration in power distribution caused by the WR breaks this periodicity.

Fig. 2(b) plots the normalized power distribution across the ZF-precoded ULA with or without considering WR for the four-UE case for the number of antennas being 32. Comparing the results obtained using the two channel models, we observe that the effects of WR exacerbates the power variation up to 6 dB across the ZF-precoded ULA, revealing that some antennas are allocated much more power than the others.

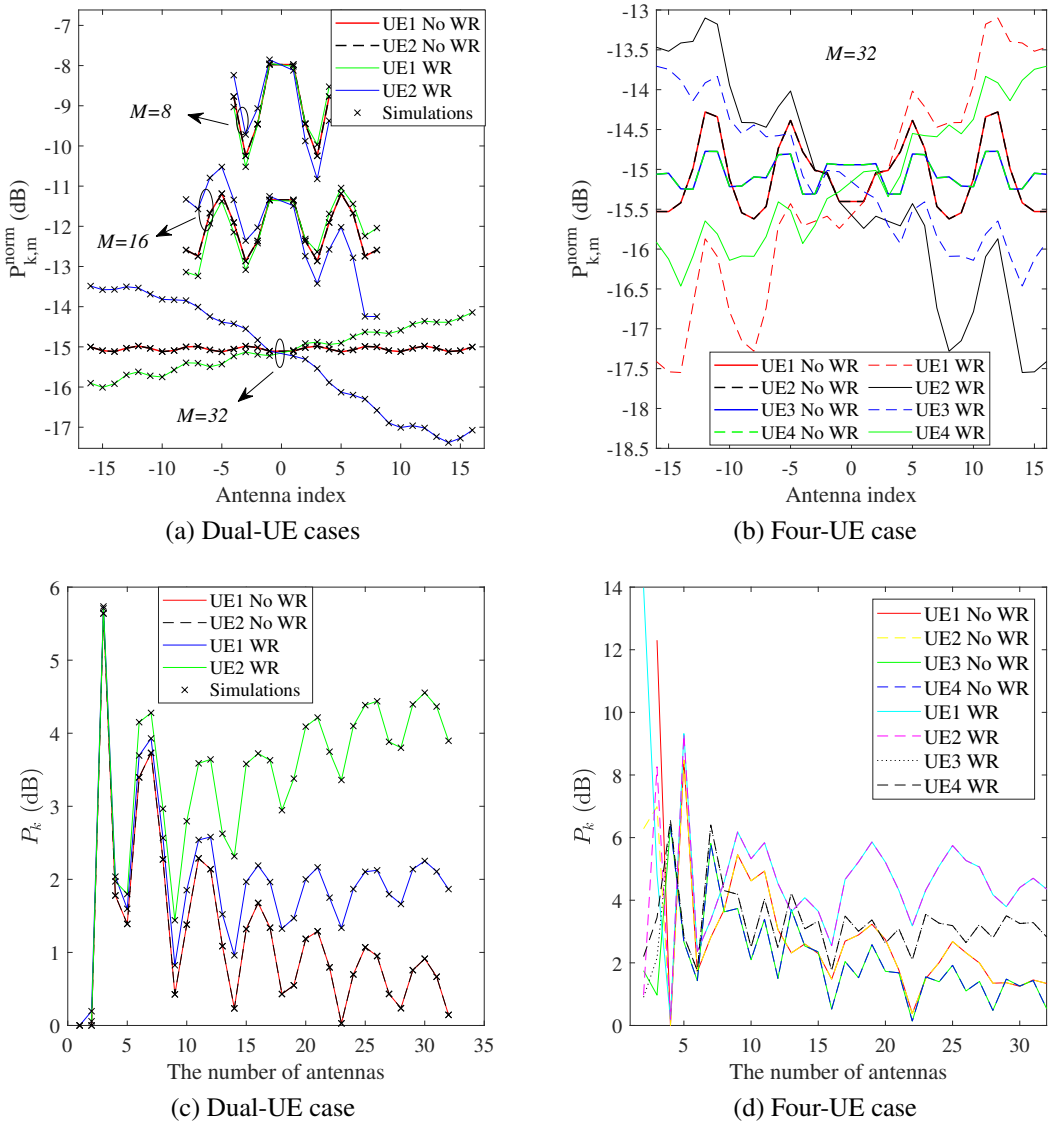

(a) Dual-UE cases (b) Four-UE case

(c) Dual-UE case (d) Four-UE case

Fig. 2. The normalized power distribution and the MPR across the ZF-precoded ULA, where $D_1 = 0.05$ m, $\zeta = 0.15$ m, $\gamma = 5$, and $\varepsilon = 5.31 - j0.3107$ for concrete [11]. Lines represent analytical results while markers represent simulation results. (Dual-UE case: $d_{1,\mathrm{LOS}} = 6$ m, $\theta_1 = \frac{5\pi}{6}$, $d_{2,\mathrm{LOS}} = \sqrt{2}$ m, $\theta_2 = \frac{\pi}{4}$. Four-UE case: $d_{i,\mathrm{LOS}} = 2$ m for $i \in \{1,2,3,4\}$, $\theta_1 = \frac{5\pi}{6}$, $\theta_2 = \frac{\pi}{6}$, $\theta_3 = \frac{2\pi}{3}$, $\theta_2 = \frac{\pi}{3}$.)

Fig. 2(c) and Fig. 2(d) show the impact of the number of antennas on the MPR across the ZF-precoded ULA with or without considering WR for the dual-UE case and the four-UE case, respectively. We can see that the MPRs obtained by our proposed channel model are larger than that obtained by the pure LOS channel model, indicating that the effects of WR exacerbates the uneven power distribution across the ZF-precoded ULA. For the dual-UE case under the pure LOS channel, MPR becomes smaller gradually when the number of antennas increases. However, under our proposed channel, increasing the number of antennas would exacerbate the non-uniform power distribution over the ULA.

Fig. 3(a) illustrates the normalized power distribution of the ZF-precoded ULA for UE 2 under different AP-wall distances for a dual-UE case, where the positions of UE 1 and UE 2 are assumed to be symmetric with respect to the midpoint of the ULA for simplicity. The result of UE 1 is symmetrical to that of UE 2 with respect to the midpoint of ULA. As shown in Fig. 3(a), the variation in the power distribution across the ULA changes greatly with the AP-wall distance, which reveals that the AP-wall distance has to be taken into account carefully.

Fig. 3(b) and Fig. 3(c) present the normalized power distribution of the ZF-precoded ULA for different values of the length (from 1 to 9 m) and the AoD (from 0 to π) of the LOS path of one user in the dual-UE case, respectively. Fig. 3(b) shows that, as the length of the LOS path increases, the normalized power for serving the UE varies slower within a smaller dynamic range, which is also observed in Fig. 2(a). In Fig. 3(c), a significant variation appears in the power distribution across the ZF-precoded ULA when θ_2 approaches $\pi/4$. This is ascribed to the location of UE 2 being very close to UE 1 with $\theta_1 = \pi/4$. In this case, the ZF precoder needs to allocate highly different power levels across the ULA to distinguish the two UEs.

From Fig. 3(b)-(c) and Fig. 2(a)-(d), we can see that the power distribution is not sensitive to the length (UE-AP distance) or the AoD of the LOS path under the pure LOS channel model, while under our proposed channel model, different multi-user spatial distributions result in different dynamic ranges of the power distribution over the ULA, which is more evident when the UE is closer to the wall.

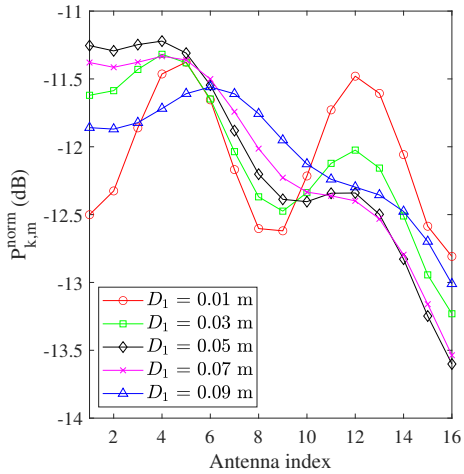

(a) The normalized power distribution for different AP-wall distances where $d_{1,\mathrm{LOS}} = d_{2,\mathrm{LOS}} = 2$ m, $\theta_1 = \frac{\pi}{6}$, $\theta_2 = \frac{5\pi}{6}$.

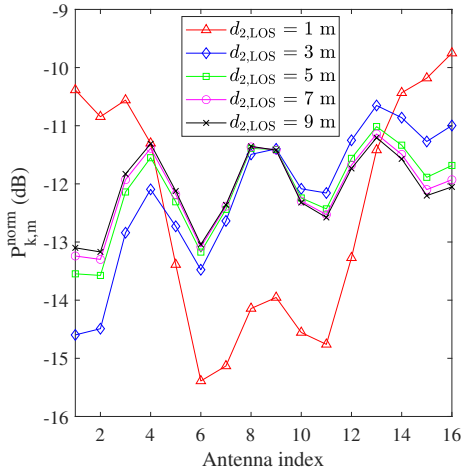

(b) The normalized power distribution for different values of $d_{2,\mathrm{LOS}}$ where $d_{1,\mathrm{LOS}} = \sqrt{2}$ m, $\theta_1 = \frac{\pi}{4}$, $\theta_2 = \frac{5\pi}{6}$, $D_1 = 0.05$ m.

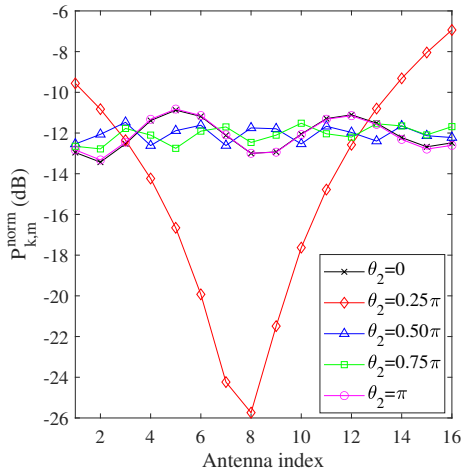

(c) The normalized power distribution for different values of θ_2 where $d_{2,\mathrm{LOS}} = 6$ m, $d_{1,\mathrm{LOS}} = \sqrt{2}$ m, $\theta_1 = \frac{\pi}{4}$, $D_1 = 0.05$ m.

Fig. 3. The normalized power distribution across the ZF-precoded ULA under different AP-wall distances and user spatial distributions, where $M = 16$, $\zeta = 0.15$ m, $\gamma = 5$, and $\varepsilon = 5.31 - j0.3107$ for concrete.

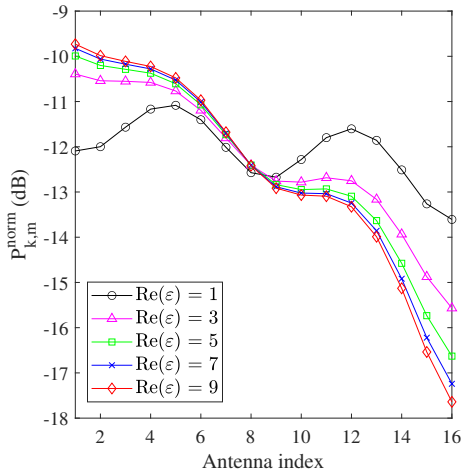

(a) The normalized power distribution under different wall permittivities where $\gamma = 5$, $\zeta = 0.15$ m.

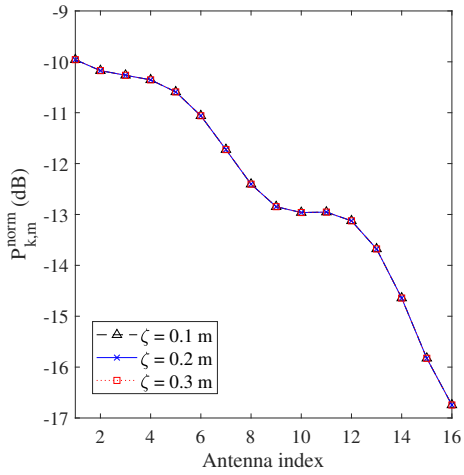

(b) The normalized power distribution for different values of wall thickness where $\gamma = 5$, and $\varepsilon = 5.31 - j0.3107$ for concrete.

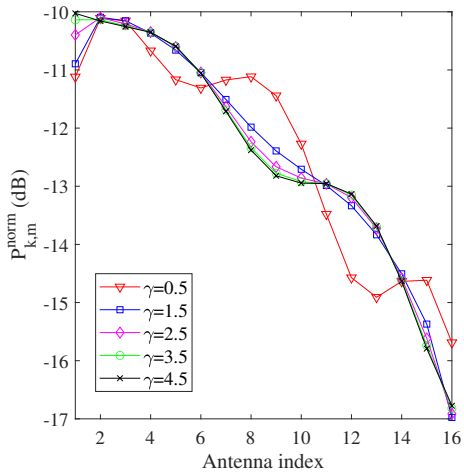

(c) The normalized power distribution for different values of γ where $\zeta = 0.15$ m, and $\varepsilon = 5.31 - j0.3107$ for concrete.

Fig. 4. The impact of wall permittivity, thickness, and mutual coupling on the normalized power distribution across the ZF-precoded ULA, where $d_{1,\mathrm{LOS}} = d_{2,\mathrm{LOS}} = 2$ m, $\theta_1 = \frac{\pi}{6}$, $\theta_2 = \frac{5\pi}{6}$, $M = 16$, $D_1 = 0.05$ m.

In Fig. 4(a)-(c), the two UEs are assumed to be symmetrically located with respect to the midpoint of the ULA for simplicity and only the result of UE 2 is plotted. The result of UE 1 is symmetrical to that of UE 2 with respect to the midpoint of ULA.

Fig. 4(a) and Fig. 4(b) present the normalized power distribution across the ZF-precoded ULA for different values of the real part of wall permittivity (from 1 to 9) and wall thickness (from 0.1 to 0.3 m) for the dual-UE case, respectively. We can see from Fig. 4(a) that the non-uniform power distribution across the ZF-precoded ULA will be exaggerated with the increase of the real part of wall permittivity. Differences as large as 8 dB are observed between the ends of the ULA. In Fig. 4(b), the power distribution does not change with the wall thickness. This is because the wavelength at 28 GHz, i.e. 1 cm, is not comparable to the typical wall thickness.

Fig. 4(c) plots the normalized power distribution across the ZF-precoded ULA for different values of γ. We can see that the power distribution across the ZF-precoded ULA changes slightly with γ ranging from 1.5 to 4.5, corresponding to the mutual coupling level between two adjacent antennas from -13.03 dB to -39.09 dB [18]. However, for a very small value of γ, e.g., $\gamma = 0.5$ corresponding to the mutual coupling level between two adjacent antennas of -4.34 dB, the mutual coupling has to be considered while analysing the power distribution over the AP's ULA.

5 Conclusion and Future works

In this paper, we build an indoor MU-MIMO downlink channel model that involves both the LOS path and the WR path. The expression of the ZF precoding matrix for the dual-UE case is analytically derived. For the scenario where the AP is deployed close to a wall, we compare the power distribution across the ULA under our channel model and that under the pure LOS channel model, in terms of the normalized power distribution and MPR. Numerical results show that the power distribution becomes more uneven across the ZF-precoded ULA under the effects of WR. Even though the proposed numerical approach has shed light on how

WR impacts the per-antenna power distribution, a comprehensive measurement campaign is still required to verify the results of this work.

The following research will be considered in future works: 1) Experimental validation of the proposed approach; 2) Consideration of actual antenna patterns; 3) The impact of an arbitrary arrangement of the AP; 4) The effects of WR on the power distribution across an MMSE/MRT-precoded massive MIMO antenna array; 5) Indoor rich scattering environment; 6) MmWave wideband wireless system.

References

[1] J. Kibiłda, *et al.*, "Indoor millimeter-wave systems: design and performance evaluation," *Proceedings of the IEEE*, Apr. 2020.

[2] V. Raghavan, *et al.*, "Millimeter-wave MIMO prototype: measurements and experimental results," *IEEE Commun. Mag.*, vol. 56, no. 1, pp. 202-209, Jan. 2018.

[3] E. Torkildson, *et al.*, "Indoor millimeter wave MIMO: feasibility and performance," *IEEE Trans. Wireless Commun.*, vol. 10, no. 12, pp. 4150-4160, Dec 2011.

[4] E. Torkildson,*et al.*, "Channel modeling for millimeter wave MIMO," *Information Theory and Applications Workshop (ITA)*, 2010, pp. 1-8.

[5] E. Torkildson, *et al.*, "Millimeter-wave spatial multiplexing in an indoor environment," *IEEE Globecom Workshops*, 2009, pp. 1-6.

[6] J. Zhang and G. De La Roche, "Femtocells: technologies and deployment," *Wiley*, 2010.

[7] S. K. Yoo, *et al.*, "Ceiling- or wall-mounted access points: an experimental evaluation for indoor millimeter wave communications," *Proc. IEEE 13th Eur. Conf. Antennas Propag. (EUCAP)*, 2019, pp. 1-5.

[8] Y. Zhang, *et al.*, "How friendly are building materials as reflectors to indoor LOS MIMO communications?," *IEEE Internet Things J.*, early access, 2020.

[9] J. Zhang, *et al.*, "Wireless energy efficiency evaluation for buildings under design based on analysis of interference gain," *IEEE Trans. Veh. Tech.*, vol. 69, no. 6, pp. 6310–6324, Jun. 2020.

[10] J. Zhang, *et al.*, "Two-ray reflection resolution algorithm for planar material electromagnetic property measurement at the millimeter-wave bands," *Radio Sci.*, , vol. 55, no. 3, Mar. 2020.

[11] "Effects of building materials and structures on radiowave propagation above about 100 MHz P series radiowave propagation," IETF, ITU-Recommendation P.2040-1, Jul. 2015.

[12] H. Zhao, *et al.*, "28 GHz millimeter wave cellular communication measurements for reflection and penetration loss in and around buildings in New York city", *Proc. IEEE Int. Conf. Commun. (ICC)*, 2013, pp. 5163-5167.

[13] P. Skrimponis, *et al.*, "Power consumption analysis for mobile mmWave and sub-THz receivers," *2020 2nd 6G Wireless Summit (6G SUMMIT)*, Levi, Finland, 2020, pp. 1-5.

[14] P. Angeletti and G. Toso, "Array antennas with jointly optimized elements positions and dimensions Part I: linear arrays," *IEEE Trans. Antennas Propag.*, vol. 62, no. 4, pp. 1619-1626, Apr. 2014.

[15] N. Amani, *et al.*, "Per-antenna power distribution of a zero-forcing beamformed ULA in pure LOS MU-MIMO," *IEEE Commun. Lett.*, vol. 22, no. 12, pp. 2515–2518, Dec. 2018.

[16] T. M. Pham, *et al.*, "Efficient zero-forcing precoder design for weighted sum-rate maximization with per-antenna power constraint," *IEEE Trans. Veh. Technol.*, vol. 67, no. 4, pp. 3640–3645, Apr. 2018.

[17] M. Gustafsson, *et al.*, "Impact of mutual coupling on capacity in large MIMO antenna arrays," *Proc. IEEE 13th Eur. Conf. Antennas Propag. (EUCAP)*, 2014, pp. 2723-2727.

[18] L. Savy and M. Lesturgie, "Coupling effects in MIMO phased array," *IEEE Radar Conference (RadarConf)*, Philadelphia, PA, 2016, pp. 1-6

[19] X. Gao, *et al.*, "Massive MIMO performance evaluation based on measured propagation data," *IEEE Trans. Wirel. Commun.*, vol. 14, no. 7, pp. 3899–3911, Jul. 2015.

[20] D. S. Shiu, et al., "Fading correlation and its effect on the capacity of multielement antenna systems," *IEEE Trans. Commun.*, vol. 48, no. 3, pp. 502-513, Mar. 2000.

[21] A. Wiesel, Y. C. Eldar and S. Shamai, "Zero-forcing precoding and generalized inverses," *IEEE Trans. Signal Processing*, vol. 56, no. 9, pp. 4409-4418, Sep. 2008.